Failure of Asperities by Hydraulically Induced Fatigue:

A Model for the Generation of Intraplate Seismicity

by

Daniel L. Needham

Thesis submitted to the Faculty of the

Virginia Polytechnic Institute and State University

in partial fulfillment of the requirements for the degree of

Master of Science

in

Geophysics

APPROVED:

J. K. Costain, Chairman

G. A. Bollinger

J. A. Snoke

August 18, 1987

Blacksburg, Virginia

Failure of Asperities by Hydraulically Induced Fatigue:

A Model for the Generation of Intraplate Seismicity

by

Daniel L. Needham

J. K. Costain, Chairman

Geophysics

(ABSTRACT)

A model is proposed in which intraplate earthquakes are triggered by the tensile failure of asperities by subcritical crack growth. The principle subcritical crack growth mechanism is fatigue driven by cyclic tensile stresses within an asperity. Cyclic stresses result from cyclic pore pressure variations which propagate from the Earth's surface because of annual variations in the height of the water table. Asperities are postulated to be porous and permeable masses of saturated host rock hydrologically connected to fluids within an open fracture. Porosity and permeability within asperities are assumed to be due to microcracks within the rock matrix. Tensile stresses within an asperity are due partly to mechanical loads, but pore pressure is the primary mechanism by which tension is developed and fatigue operates primarily in tension. Fatigue crack growth is enhanced by chemical subcritical crack growth mechanisms such as stress corrosion and these mechanisms are proposed to act in unison. Faulting may be initiated when a population of asperities is either driven to failure by these mechanisms alone or when it is weakened to the point at which it is vulnerable to small applied stresses. Numerical modeling of the interaction of pore pressures and stresses within asperities indicates that a small transient increase of pore pressure on the order of a fraction of a megapascal will increase the tensile stresses within an asperity by a fraction of a megapascal. Consequently, it may be possible for a small increase in pore pressure, due to elevated water table levels, to trigger asperity failure and result in seismicity.

Acknowledgements

Many people assisted me in my tenure here at Virginia Tech. First, I would like to thank all the professors that I had as an undergraduate here at Virginia Tech for providing me with the educational foundation and technical wherewithal which allowed me to pursue postgraduate studies. I would sincerely like to thank my major advisor, Dr. Costain for his patience and guidance throughout the course of my graduate research. Furthermore, I would like to thank Dr. Snoke and Dr. Bollinger for their valuable suggestions about the research and comments on the manuscript. Also, I would like to thank Dr. Coruh and Dr. Robinson, who were not directly involved in my research, but nonetheless provided their time and advice willingly when asked. Mildred Memitt and Bob Montgomery were extremely helpful and made it possible for me to learn the use of the VAX facilities and digitizing equipment. I am grateful to Matt Sibol for providing assistance with the Seismological Observatory data base and computer facilities. My fellow graduate students helped to make my tenure as a graduate student an enjoyable one and also provided the comraderie and competition that pushed me to do my best in research, teaching and academics. I would also like to thank the department for providing me with the financial support which made my studies possible. Last, but certainly not least, I would like to thank my wife, Barbara for supporting me, emotionally and otherwise, in my pursuit of higher education. Barbara has been a constant source of inspiration to me and it is to her that I dedicate this thesis.

Table of Contents

List of Illustrations

List of Tables

Introduction

In the southeastern United States there are four active areas of intraplate seismicity: the South Carolina-Georgia Seismic Zone, the Eastern Tennessee Seismic Zone, the Giles County, Virginia Seismic Zone and the Central Virginia Seismic Zone. In general, there is no obvious active tectonism responsible for the seismicity in any of these regions. Costain and others (1987) put forth the hypothesis (termed Hydroseismicity) that natural transient increases in fluid pressure in the surface recharge areas of groundwater basins can be transmitted to hypocentral depths (10-20 km) and trigger earthquakes. Inherent in this hypothesis is the fact that the seismogenic volume is a saturated, fractured and permeable region with connections to the Earth's surface. Seismicity, which occurs along pre-existing fractures, may be triggered by small pore pressure increases at hypocentral depths and hydrolytic weakening to the point of failure. Moreover, it is assumed in the Hydroseismicity hypothesis that the failure of a population of asperities triggers seismicity. The purpose of this research is to investigate material fatigue within asperities resulting from cyclic pore pressure variations as a possible trigger mechanism for Hydroseismicity and to determine to what extent a small pore pressure change affects the stresses within a single asperity.

Fracture surfaces consist of asperities which bear the entire load across the fracture. The resistance to sliding along a fracture is determined by the strength of the asperities (Byerlee, 1967).

Costain and others (1987) proposed that fluid interaction with asperities reduces their shear strength and thereby leads to asperity failure. On a laboratory specimen scale the size of asperities is on the order of a grain size, whereas on a field scale asperities are surface roughness patches composed of a mass of the host rock. Asperities herein will be defined as any point or collection of relatively small areas of contact across a fracture. **The idea is put forth that asperities are composed of a porous and permeable solid matrix which is saturated and hydrologically connected to the fluids within the open fracture.** Accordingly, fluid pressure changes as transmitted along fractures from the Earth's surface to hypocentral depths encounter asperities and induce pore pressure changes within the asperities. Moreover, an increase in pore pressure within an asperity is accompanied by a change in the stresses within the solid matrix as governed by the theory of Biot (1941). Furthermore, an increase in stress leads to deformation which can be accommodated by the growth of microcracks within the solid matrix. While overall deformation along a fracture is due to shear stresses, it is possible that on the asperity scale tensile stresses exist (Byerlee, 1967). In other words, the shear stress that causes motion along a fracture applied as a loading condition on an asperity may cause local tension to develop within the asperity. Consequently, the Griffith theory of brittle failure (1921), based on the growth of microcracks in tension, is the mechanism by which the asperities fail and asperity failure controls faulting. Therefore, it is proposed that asperities will be weakened by hydraulically induced tensile crack growth and that this reduction of asperity strength reduces the coefficient of friction across a fault. Accordingly, failure should occur when the slope of the Mohr failure envelope decreases to the point where it touches the Mohr circle.

According to Griffith (1921), rapid unstable crack growth that results in failure occurs when the stresses at the tips of microcracks meet or exceed some critical value characteristic of the material; however, it is possible for microcrack growth to occur at stresses below the critical stress value. Crack growth that occurs in this fashion is characterized by slow, stable growth and is termed subcritical crack growth (Ewalds and Wanhill, 1984). Failure will result when several microcracks coalesce to form a larger single crack or when a single crack grows to a length which is not capable of sustaining the applied load. Fatigue is a subcritical crack growth mechanism which is driven by

cyclic stresses with maximum amplitudes not in excess of the critical stress of the material. The cyclic stresses are proposed to be the result of cyclic pore pressure variations which propagate from the Earth's surface through permeable crystalline rocks to hypocentral depths. Pore pressure cyclicity is caused by the annual cyclic variation in the elevation of the water table. Therefore, it is proposed that small cyclic fluid pressure changes within asperities reduce the strength of asperities by the process of fatigue. Furthermore, the overall resistance of a fracture to sliding decreases as asperities are weakened. Accordingly, the slope of the failure envelope gradually decreases until it intersects the Mohr circle at which point a population of asperities fails and an earthquake results. Active seismic volumes are assumed to contain numerous fractures and permeability is primarily due to these fractures. This is consistent with Brace (1984) who suggested that for crystalline rocks that extend to the Earth's surface permeability is on the order of a few tenths to a few tens of millidarcys and is primarily due to fractures.

A two-dimensional finite element code which utilizes Biot's (1941) coupled equations of elastic deformation and pore fluid flow is used to investigate the interaction of pore pressures and stresses within rectangular shaped asperities. Various asperity sizes and loading conditions are modeled in an attempt to provide some insight into the magnitudes and distributions of stresses within an asperity. An important reason for the numerical modeling is to establish the presence and extent of the region of tension produced by the addition of fluid to the asperity. Once the stresses within an asperity have been established, the likelihood of fatigue crack growth is discussed. Finally, results are discussed with applications to reservoir induced seismicity and to intraplate seismicity within the Central Virginia Seismic Zone. The Central Virginia Seismic Zone was chosen because of the four seismic zones in the southeastern United States it exhibits the shallowest seismicity and, consequently, the Hydroseismicity hypothesis has a greater likelihood of being applicable to this region.

Literature Review

Correlations Between Fluid Pressure Transients and Seismicity

Reservoir Induced Seismicity: Since the first recognized case of reservoir induced seismicity (RIS) associated with the impoundment of Lake Mead behind the Hoover Dam in the mid-1930's (Carder, 1945), seismicity attributed to the impoundment of large reservoirs has been well documented (Simpson, 1976 and references therein). In general, RIS is characterized by shallow to intermediate (1-20 km) focal depths in areas of high to moderate strain accumulation. Also, when compared with the orientation of mapped surface faults, fault plane solutions from reservoir induced earthquakes suggest that RIS occurs along pre-existing fractures with the potential for RIS being greatest in regions of strike-slip and normal faulting. Furthermore, major bursts of earthquake activity usually begin some three to six years after the initial reservoir impoundment (Gupta, 1985). Exceptions to this are the August, 1976 Lake Oroville, California earthquake, 8 years after initial impoundment and the November, 1981 Aswan High Dam earthquake, 16 years after impoundment (Rajendran and Gupta, 1986).

The principal driving force behind RIS is generally attributed to the diffusion of fluid pressure from the surface pressure source, the reservoir, to hypocentral depths. On the basis of the obser-

vation of linear growth of the epicentral area associated with RIS, Talwani and Acree (1985) calculated a "seismic" hydraulic diffusivity, α_s. Their results indicate that the seismic hydraulic diffusivity is in the range of 10^3 to 10^5 cm²/sec , which is equivalent to within an order of magnitude to the material hydraulic diffusivity, $\alpha = \frac{k}{\mu\varphi\beta}$ where k is the intrinsic permeability, μ is fluid viscosity, φ is porosity and β is fluid compressibility. The major controlling factor for pore pressure diffusion is permeability. Accordingly, assuming $10^3 \leq \alpha \leq 10^5$ cm²/sec, Talwani and Acree (1985) calculated a range of permeability on the order of $0.1 \leq k \leq 10$ mdarcy which is in agreement with the range of permeabilities of crustal rocks at hypocentral depths given by Brace (1984). The time it takes for a pore pressure change to diffuse to hypocentral depth has been hypothesized (Bell and Nur, 1978; Talwani and Acree, 1985) to account for the time lag between impoundment and the onset of seismicity. Moreover, in some cases seismicity has been correlated to pore pressure changes induced by fluctuations in reservoir levels (Rajendran and Gupta, 1986), but as yet no theory has been put forth to adequately explain this apparent phenomenon. However, a fatigue failure model will be put forth in a later section which may explain this phenomenon.

Once a change in pore pressure diffuses to hypocentral depths, it can affect the crustal rocks in two ways: (1) reduce the effective normal stress across the fault and (2) reduce the shear strength of the rock material. Talwani and Acree (1985) suggest that the spatial and temporal RIS patterns are controlled by the mechanical effects of pore pressure, but the actual onset of seismic activity is due to the chemical effect of water reducing the coefficient of friction in clays that line the fractures. Zoback and Hickman (1982) state that for the Monticello Reservoir, South Carolina, a pore pressure increase of 10 bars will not move the Mohr circle to the failure envelope for a coefficient of friction of $0.6 \leq \mu \leq 0.85$ and further suggest that RIS in the vicinity of the Monticello Reservoir should only extend to 500 m depth; however, seismicity extends to 2 km and Talwani and Acree (1985) explain this discrepancy in the following manner. The pre-existing fractures are lined with clays with a clay-rock coefficient of friction on the order of $\mu \leq 0.4$. Fluid interaction with the clays can reduce this coefficient of friction to $0.1 \leq \mu \leq 0.2$ and, coupled with a pore pressure increase, this should be sufficient to initiate seismicity. In general, the presence or absence of

seismicity will depend on the complex interaction of the pore pressure changes resulting from reservoir level fluctuations and tectonic, geologic and hydrologic factors.

Certain aspects of RIS have important implications for the Hydroseismicity hypothesis. If seismicity can be triggered by pore pressure changes in the crust resulting from reservoir level changes at the Earth's surface as shown, for example, by Bell and Nur (1978), then the seismogenic zones must be saturated with some connection to the surface. Furthermore, reservoir induced earthquakes extend to depths of 5 to 20 km which suggests that it may be possible for natural increases in pore pressure to trigger seismicity, especially in shallow intraplate seismic zones such as the Central Virginia Seismic Zone.

Injection Induced Seismicity: In March 1962 the U. S. Army Corps of Engineers began the deep injection of contaminated wastewater at the Rocky Mountain Arsenal northeast of Denver, Colorado. The well bottomed in crystalline Precambrian bedrock at a depth of approximately 3.6 km and over a four year period from 1962 to 1966 roughly 625 million liters of fluid was disposed of in the well (Hsieh and Bredehoeft, 1981). Between the period April 1962 and August 1967 over 1500 small earthquakes were detected, some exceeding Richter magnitudes of 3 and 4 (Hsieh and Bredehoeft, 1981). Evans (1966) was the first to suggest a relationship between the earthquakes and the fluid injection at the Rocky Mountain Arsenal. His hypothesis was based on an apparent correlation between the frequency of the earthquakes and the volume of fluid injected, as well as the spatial proximity of the earthquake hypocenters to the injection well.

In a follow up study, Hsieh and Bredehoeft (1981) describe the seismogenic volume with which the "Denver Earthquakes" are associated as a fractured Precambrian crystalline reservoir within which seismicity takes place along pre-existing fractures. After constructing a reasonable model of this reservoir based on hydrologic and geologic data, Hsieh and Bredehoeft computed the pressure buildup due to the pressure injection of wastewater. Their overall conclusion was that the spatial

and temporal distribution of earthquake hypocenters was governed by a "critical pressure". That is, earthquakes were mostly confined to regions of the reservoir where the pressure buildup was greater than a critical pressure of 32 bars (in excess of hydrostatic). Furthermore, the work done by these injection related pressures alone could not account for the total energy released by the earthquakes. Accordingly, strain energy, due to natural tectonic stresses present in the Precambrian rocks, must have been released by a pore pressure triggering mechanism (Hsieh and Bredehoeft, 1981). Many triggering mechanisms have been proposed. For example, chemical reactions between the wastewater and the rock could have reduced the shear strength of the rock, thereby allowing slippage (Hsieh and Bredehoeft, 1981). On the other hand, the existence of a critical pressure suggests that the Hubbert-Rubey Mechanism (Hubbert and Rubey, 1959) was the predominant mechanism by which these earthquakes were initiated. Moreover, such a small value (32 bars) for the critical pressure suggests that the rocks were already stressed close to failure prior to fluid injection and that seismicity occurred along pre-existing fractures (Hsieh and Bredehoeft, 1981). Additionally, several earthquakes occurred after the fluid injection had ceased. To explain this phenomenon Healy and others (1968) noted that while cessation of fluid injection at the well decreases the pressure at the well, the pressure front at large distances away from the well continues to advance. In other words, pore pressure diffusion was the principal driving force generating seismicity.

In another study, the U. S. Geological Survey conducted an experiment at Rangely, Colorado to determine to what extent pore pressure controls the occurrence of earthquakes. The experiment was conducted in an oil field in which Chevron Oil Company began injecting fluids, in 1958, into reservoir rock (Weber Sandstone) at a depth of 1.8 km to facilitate enhanced oil recovery. Fluid pressures in the periphery of the reservoir rose from 170 bars, hydrostatic for 1.8 km, to 240 - 275 bars (Raleigh and others, 1972). From 1969, when the U. S. Geological Survey began detailed monitoring of seismic activity in the area, to 1971 over 1000 small earthquakes were recorded (Raleigh and others, 1972). Results from this study indicate that earthquakes occurred along a single pre-existing fault in areas where the total pore pressure exceeded 255 bars (85 bars above

hydrostatic). As a result, the critical pressure for the Rangely earthquakes was 85 bars, significantly greater than that for the Denver earthquakes. Bottom hole pressures in the injection wells at Rangely were known to be approximately 275 bars. Also, when pressure injection was decreased by 35 bars seismicity ceased (Raleigh and others,1972). This is in contrast to the Denver earthquakes which did not cease immediately after pressure injection was stopped (Hsieh and Bredehoeft, 1981).

These two cases of injection induced seismicity established beyond a doubt that pore pressure can play a role in the generation of some seismic activity. Several conclusions, with implications towards Hydroseismicity, can be drawn from the results obtained from studies related to injection induced seismicity. First, the spatial and temporal correlation between earthquake locations and zones of pressure in excess of some critical value suggests that seismicity may be triggered by an increase in pore pressure. Furthermore, the mechanism by which the pressure front advances through the reservoir may be attributed to pore pressure diffusion. Also, the difference in the values of critical pressure for the two cases discussed above (32 bars--Denver, 85 bars--Rangely) suggest that the critical pressure is a variable possibly dependent upon hydrologic, geologic and tectonic factors. For example, in Denver the earthquakes occurred along multiple fractures, whereas at Rangely the earthquakes apparently occurred along a single fault. This suggests that a more highly fractured seismogenic zone with a correspondingly higher permeability may require a lower critical pressure in order to initiate earthquake activity. On the other hand, the earthquakes occurred in different rock materials with different fracture strengths. Or, perhaps the tectonic stresses in the Rangely area were not so large that the host rocks were stressed as close to failure as they were in the Denver area. This is probably an indication that these two regions are markedly different in their respective hydrologic, geologic and tectonic environments and that the interplay of these factors determines the nature and extent of induced seismicity in ways that remain unexplained.

Seismicity Induced from Natural Pore Pressure Increases: While pore pressures resulting from artificially induced seismicity, as in the case of reservoirs and fluid injection, are much higher than pore pressures that occur naturally, there have been several studies which suggest a correlation between natural pore pressure variations, resulting from rainfall and river level fluctuations, and seismicity. For instance, Taber (1914) reports that for the two years prior to the 1886 Charleston, South Carolina earthquake rainfall was well above normal ($\cong$65 in/yr). Conversely, the five year period following the 1886 earthquake was marked by comparatively lower rainfall ($\cong$45 in/yr) and a lower frequency of earthquakes. This two year time span between increased rainfall and seismicity is reasonable for a time delay associated with a pore pressure diffusion driving mechanism. Furthermore, 1891-1897 was a period of high seismicity and the average annual rainfall was 52 inches. Whereas, average annual rainfall from 1898-1914 was 39 inches and the period was marked by a low earthquake frequency. Consequently, Taber (1914) postulated a gross correlation between average annual rainfall and earthquake frequency for the local Charleston area. Of course, rainfall does not directly correspond to a pore pressure change at depth in the Earth's crust. Rainfall does, however, affect the water table elevation and river stage levels and therefore, a direct correlation between a particular rainfall event and seismicity is not to be expected. Consequently, a correlation between seismicity and river stages or water table elevations where there is a time lag between a high river stage and seismicity is more likely to exist.

In the New Madrid Seismic Zone, Nava (1983) showed that there is a correlation between the Mississippi River stage and New Madrid seismicity. Using statistical methods, Nava showed that six to nine months after a maximum stage (roughly 0.9 bars of fluid pressure) earthquake frequency increased. Also, when the river level increase is small (0.3 bars) and of short duration there is an almost instantaneous ($<$ 1 month) increase in earthquake frequency. Thus, there is an apparent correlation between the rate of change of Mississippi River levels and the time delay to the initiation of the New Madrid seismicity. A sudden decrease in river stage results in a closely following decrease in seismic activity and similarly, a sudden increase in river stage results in a near instantaneous increase in earthquake activity (Nava, 1983). In another study, a relationship between water

table levels and earthquake frequency in the Coyote Lake region southeast of Berkeley, California was postulated. A period of drought and low earthquake frequency in the late 1970's was followed by a wet, rainy period and an increase in seismicity. In August 1979 an $M_L = 5.9$ earthquake occurred followed by an aftershock sequence of 31 events over a ten day period with $2.4 \leq M_L \leq 4.4$ (Uhrhammer, 1980). For the ten days following the main event aftershocks migrated progressively further (up to 20 km) from the main event in a southeasterly direction (Uhrhammer, 1980). This temporal and spatial migration of the seismic activity was determined to be consistent with a pore pressure diffusion mechanism driven by a water table elevation increase (Pradeep Talwani, personal communication, 1987).

Hydroseismicity: A new hypothesis termed Hydroseismicity has been put forth to explain the role of water in the generation of intraplate seismicity (Costain and others, 1987). This hypothesis has hydrologic elements, i.e., diffusion of pore pressure transients from surface recharge areas of groundwater basins, geologic elements, i.e., fractured crust and chemical elements, i.e., solubility of minerals. It is based on a spatial correlation between crustal volumes of high seismicity, large gravity-driven river basins and a fractured permeable crust that is tectonically stressed close to failure. Seismicity may be triggered by transient increases in fluid pressure transmitted from recharge areas of groundwater basins to depths of 10-20 km. Implicit in this model is the existence of open fractures at hypocentral depths. Fractures are kept open even under ambient tectonic stresses by fracture surface irregularities, i.e., asperities. In the context of this paper asperities are defined as patches of surface roughness on the fracture surface which act, in combination with fluid pressures between fracture surfaces, to keep the fracture open. Assuming that asperities will have the same overall rhealogical properties as the host material, they will be composed of saturated porous and permeable material. The porous and permeable nature of the asperity rock matrix is assumed to be primarily due to microcracks. According to Simmons and Richter (1976) microcracks are very common in all rocks and especially extensive in regions where there is some source of "shock" such as in active seismic areas. The presence of many multigrain "shock" crack subsets has been noted

in petrographic descriptions of crystalline rocks and will contribute to the porosity and permeability of the rock matrix (Simmons and Richter, 1976). Costain and others (1987) proposed that subcritical crack growth by mechanisms of stress corrosion and hydrolytic weakening gradually decrease the strength of asperities. Earthquake activity may be initiated when a population of asperities is weakened to the point at which it is vulnerable to small applied stresses which result from small transient increases of fluid pressure.

Byerlee (1967) was the first to suggest that brittle fracture of surface asperities may be the mechanism controlling frictional sliding of brittle materials such as granite and, thus, structural weakening of asperities should ultimately be responsible for the initiation of earthquake activity. During frictional sliding the resistance to sliding is governed by the strength of asperities (Byerlee, 1967). Accordingly, as asperities are continually weakened by the process of subcritical crack growth the frictional resistance to sliding across the fault is reduced. Consequently, a point will be reached where either the ambient tectonic stresses are enough to cause slippage, from the failure of a population of asperities and a subsequent earthquake or the asperities will be weakened to the point at which they are vulnerable to a small applied load. Even though the fracture surfaces are subject to shear stresses it is possible that on the asperity level local tensile stresses exist (Byerlee, 1967). If tensile stresses do exist within asperities then it is more likely that subcritical crack growth can occur within asperities. As a result, the failure of asperities under tension could play a major role in the generation of earthquakes.

Linear Elastic Fracture Mechanics Applied to Failure in Rocks

Theory of Crack Propagation: The study of crack growth by the principles of linear elastic fracture mechanics is well documented, e.g., in engineering materials, Parker (1981), Broek (1982) and Ewalds and Wanhill (1984) and in geologic materials, Jaeger and Cook (1976). All materials contain microcracks which may be present without causing failure under a given load. Based on

the hypothesis as first put forth by Griffith (1921), crack propagation is caused by stress-concentrations at the tips of microcracks and failure occurs when the maximum stress near the tip of a favorably oriented crack reaches a critical value characteristic of the material. According to Griffith, crack propagation will occur if the energy released by crack growth provides all the energy necessary for crack growth. If this is not the case then the stress must be raised in order to propagate a crack. Therefore, if a crack extension of length da is to occur the following must be true:

$$\frac{dU}{da} = \frac{dW}{da} \qquad [1]$$

where U is the elastic energy, dU/da is the elastic strain energy release rate per crack tip or crack driving force, W is the energy required for crack growth and dW/da is the energy consumed during crack extension or crack resistance force. Both dU/da and dW/da have the dimensions of force per unit crack extension. Accordingly, for crack extension to occur two conditions must be met: (1) the stresses ahead of the crack must be above some critical value (material dependent), and (2) the total energy of the system must be reduced by an incremental extension of the crack. Consequently, crack growth generally occurs if high stresses are present in the material.

The material responds to energy input by crack extension which releases energy. The strain energy release rate per crack tip, G is (plane strain),

$$G = \sigma^2 \pi a \frac{(1 - \nu^2)}{E} \qquad [2]$$

where, σ is the remote applied stress in the material, a is 1/2 of the crack length, E is Young's modulus and ν is Poisson's ratio. A threshold condition for crack growth is that the energy absorbed during crack growth (a constant) is about equal to the energy release rate, G. Therefore, there is a value G_c , a material property which depends on the energy required to break atomic bonds within the material, at which crack propagation will occur, e.g., for plane strain,

$$G_c = \sigma_c^2 \pi a \frac{(1 - \nu^2)}{E} \qquad [3]$$

where, σ_c is the critical stress and is given by,

$$\sigma_c = \left[\frac{2\gamma E}{\pi a}\right]^{\frac{1}{2}} \quad [4]$$

and 2γ is the surface energy required to form a new free surface. This is the original Griffith criterion for failure.

In general, the stresses near a crack tip are proportional to the stress intensity factor, K_L where the subscript L (L = I, II or III) denotes the crack tip deformation mode, opening mode--Mode I, shear mode (in-plane shear)--Mode II or tearing mode (out of plane shear)--Mode III. For any mode,

$$K_L = Y\sigma(\pi a)^{\frac{1}{2}} \quad [5]$$

where Y is a numerical modification factor which accounts for crack geometry, loading conditions and edge effects. For instance, for Mode I (plane strain),

$$K_I = Y\left[\frac{GE}{1-\nu^2}\right]^{\frac{1}{2}} \quad [6]$$

Consequently, K_L is a function of the energy release rate, G. The stresses in the vicinity of the crack tip are proportional to the stress intensity factor and are given by (for Mode I, plane strain),

$$\sigma_x = \frac{K_I}{\sqrt{2\pi r}}\cos\frac{\theta}{2}\left[1 - \sin\frac{\theta}{2}\sin\frac{3\theta}{2}\right] \quad [7]$$

$$\sigma_y = \frac{K_I}{\sqrt{2\pi r}}\cos\frac{\theta}{2}\left[1 + \sin\frac{\theta}{2}\sin\frac{3\theta}{2}\right] \quad [8]$$

$$\tau_{xy} = \frac{K_I}{\sqrt{2\pi r}}\cos\frac{\theta}{2}\sin\frac{\theta}{2}\cos\frac{3\theta}{2} \quad [9]$$

$$\sigma_z = \mu(\sigma_x + \sigma_y) \quad [10]$$

where r and θ are polar coordinates with the origin at the crack tip. From the above equations it is clear that when r = 0, e.g., at the crack tip, the stress is equal to infinity. In reality, however, this cannot occur and plastic deformation which develops in the immediate vicinity of the crack tip keeps the stresses finite (Ewalds and Wanhill, 1984). Even though there is a small zone of plastic deformation in the vicinity of the crack tip, linear elastic fracture mechanics is still a valid means by which to approach the problem of crack growth. In other words, the stress intensity factor is a sufficient measure for all stresses in the vicinity of a crack (Broek, 1982).

It is clear from the previous discussion that there must be a value of K for which unstable crack growth can occur. This value is called the critical stress intensity factor, K_c and it is dependent upon the amount of crack tip constraint which is a function of specimen thickness and geometry. In general, the values of K_c are determined experimentally. For mode I crack tip deformation the critical stress intensity factor is given by,

$$K_{Ic} = Y\sigma_c\sqrt{\pi a} \qquad [11]$$

It is important to note that in the case of Mode I crack growth a thin plate with an internal crack and a uniaxial remote applied tensile stress, T, is the equivalent loading situation to a thin plate with an internal crack loaded with fluid pressure, P, of the same magnitude as the tensile stress (T = P).

Fatigue Crack Growth: In the previous discussion it was shown that cracks within a material can produce failure when the applied load causes the stresses at the crack tip to reach a critical value; however, it is possible for crack growth and failure to occur when the applied load is not sufficient to cause the crack tip stresses to reach a critical value. Crack growth that occurs at stress values below the critical stress is termed subcritical crack growth. In general, subcritical crack growth occurs in a slow, stable fashion. Failure occurs when the crack has reached a critical length, a_c , at which the stress intensity factor becomes equivalent to the critical stress intensity factor or when a

set of microcracks coalesce to form a larger crack of length, a_c. In this manner failure can occur even when the remote applied stresses are not equal to or in excess of the critical stress. It is believed that subcritical crack growth is the predominant mechanism of crack growth in geologic materials (Atkinson, 1984; Swanson,1984). The most predominant mechanism of subcritical crack growth in engineering materials is fatigue, which results from cyclic loading with maximum and minimum load levels below the fracture strength of the material. Until this time fatigue has not been considered as a primary driving force for subcritical crack growth in geologic materials because natural cyclic stresses were not hypothesized to exist in the Earth's upper crust. In the following discussion a description of the fatigue phenomenon based on a fracture mechanics approach is presented (after Broek, 1982).

In general, fatigue crack growth is characterized by the rate of crack propagation per cycle, da/dN, which is a function of the stress intensity factor range, ΔK, where,

$$\frac{da}{dN} = f(\Delta K) = f\left[(S_{max} - S_{min})\sqrt{\pi a}\right] = f(2S_a\sqrt{\pi a}) \qquad [12]$$

where S_{max} and S_{min} are the maximum and minimum stresses, which may be either tension, compression or both, in a cycle, respectively, S_a is the stress amplitude and N is the number of cycles. (The symbol S is used to denote cyclic stress.) This relationship takes the form of a simple power function equation,

$$\frac{da}{dN} = C \cdot (\Delta K)^n \qquad [13]$$

where C and n are experimentally determined material constants and $\Delta K = K_{max} - K_{min}$. Equation [13] is the Paris Equation (Ewalds and Wanhill, 1984) and it is an empirically derived formula. This equation is limited to the range of experimental data where there is a linear relationship between da/dN and ΔK. A more general equation is the Forman Equation which is valid over all ranges of da/dN vs. ΔK (Ewalds and Wanhill, 1984). This equation is

$$\frac{da}{dN} = \frac{C(\Delta K)^n}{(1 - R)K_c - \Delta K} \qquad [14]$$

where $R = \frac{S_{min}}{S_{max}}$. Because the stress intensity factor is dependent upon the crack length, a crack extension will cause the stress intensity factor to increase. Consequently, the further along in the crack growth cycle the material is the closer to failure it becomes. Failure occurs during the cycle in which the stress intensity factor reaches the value K_c, the critical stress intensity factor; however, crack length is not the critical parameter governing crack growth rate. No matter what the size of the cracks, if their ΔK is the same they will exhibit the same rate of fatigue crack growth (Broek, 1982). It is obvious from the above discussion that detailed experimental fatigue testing of the material in question is necessary in order to determine the parameters which characterize fatigue crack growth. To date, these data are not available for geologic materials. Moreover, experimental determination of fatigue crack growth parameters for every type of loading condition, crack size, shape and orientation is not possible (Ewalds and Wanhill, 1984).

On the other hand, it is possible to make qualitative assessments of the various factors that affect the rate of crack propagation. For instance, it has been shown (Bradshaw and Wheeler, 1969) that fatigue crack propagation in normal wet air can be an order of magnitude higher than in a vacuum. Also, fatigue crack growth in a liquid environment that causes stress corrosion enhances crack growth rates (Ewalds and Wanhill, 1984). This suggests that the presence of fluids within a crack may act to accelerate crack growth. In addition, an increase in temperature decreases the number of cycles necessary for a crack extension of some length, da (Broek, 1982). In other words, high temperatures accelerate fatigue crack growth. Moreover, low-frequency fatigue cycles and elevated temperatures enhance chemical effects such as stress corrosion and result in a more rapid crack propagation rate (Ewalds and Wanhill, 1984). These effects are important because at depths in the Earth's crust fluid-filled cracks and elevated temperatures are expected to exist.

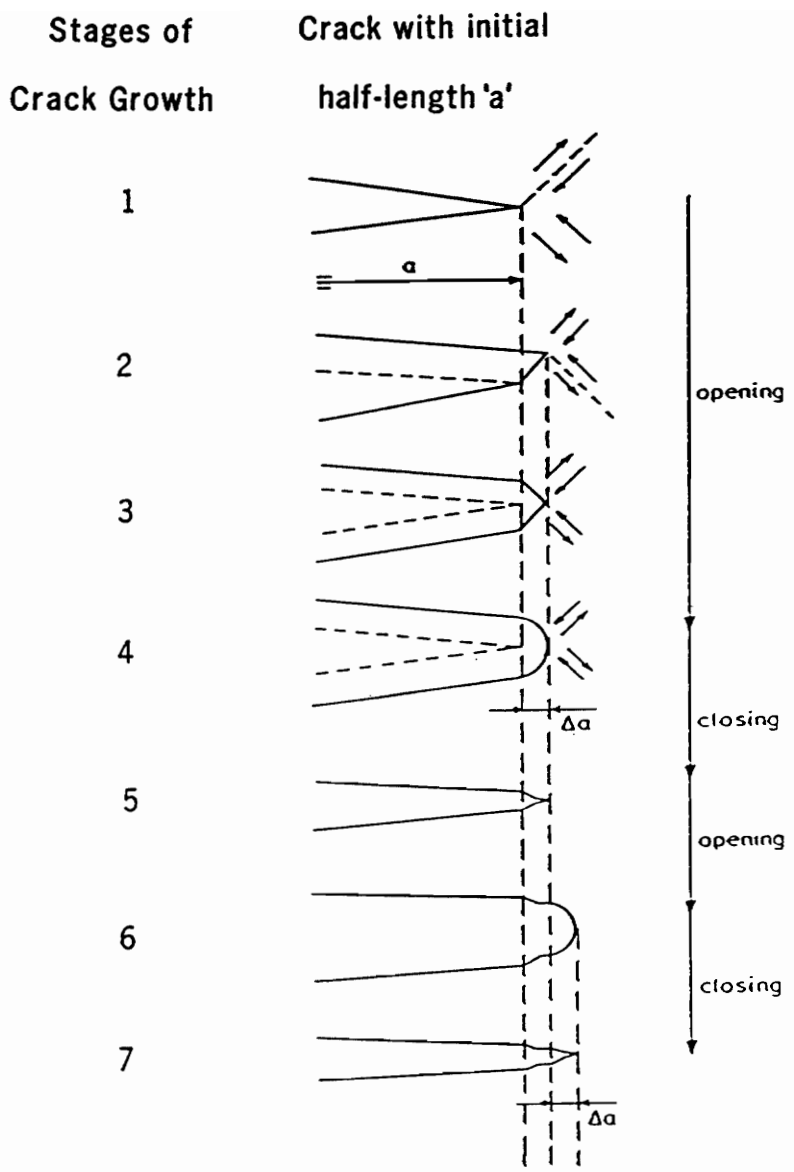

Figure 1. Fatigue Crack Growth Model: Various stages in the growth of a crack due to a fatigue mechanism (from Broek, 1982). $\Delta a \cong da$ in equation number [12]. Stages 1 - 4 correspond to the rising part of the load cycle. In these stages failure occurs along favorable planes in the direction of maximum shear stress. This causes a blunt crack tip to form. In stage 5, during the falling part of the load cycle, elastic material exerts compressive stresses on the near tip zone of plastic deformation which closes and resharpens the crack tip. In stages 6 and 7 the process repeats.

Fatigue Crack Growth Model: The mechanism by which fatigue crack growth occurs is generally attributed to cyclic plastic deformation. The following fatigue crack growth model has for its basis the model put forth by Broek (1982). There are several stages of fatigue crack growth (see Figure 1). A sharp crack under a tensile load has large stress concentrations associated with its tip where slip can easily occur. In stages 1 and 2, the material above the crack slips along a favorable plane in the direction of maximum shear stress. This slippage causes the crack to open and extend and slip can now occur on another plane, stage 3. In stage 4, increasing stress activates other parallel slip planes which leads to a blunt crack tip. At this point the crack has extended by an amount Δa. Stage 5 corresponds to the falling part of the load cycle. During this stage the elastic material, which surrounds the near tip zone of plastic deformation, will exert compressive stresses on the plastic zone. These compressive stresses are above yield, at least at the crack tip. Consequently, reversed plastic deformation occurs which will close and resharpen the crack tip. In stages 6 and 7 the process reoccurs. This cyclic opening and closing of the crack develops a rippled pattern with each cycle adding a new ripple. These effects have been observed on fracture surfaces under the electron microscope and are called fatigue striations. In addition, a cleavage mechanism may accelerate fatigue crack propagation. Typical fatigue crack propagation rates (da/dN) for an Al-Cu-Mg alloy range from 10^{-2} to 10^{1} μm per cycle (Broek, 1982).

Mechanism of Fracture in Rocks: The following discussion is based on a study on crack propagation in materials that cleave (Gandhi and Ashby, 1979) and a study on subcritical crack propagation in rocks (Atkinson, 1982). At this point it is appropriate to define a microcrack as it relates to geologic materials. A microcrack is "... an opening that occurs in rocks and has one or two dimensions much smaller than the third. For flat microcracks, one dimension is much less than the other two and the width to length ratio, termed crack aspect ratio, must be less than 10^{-2} and is typically 10^{-3} to 10^{-5}. The length may be as great as meters, but typically is of the order of 100 μm or less... large scale openings, such as vugs, joints etc., are excluded..." (Simmons and Richter, 1976). The most important fracture mechanism in the upper 20 km of the Earth's crust is fracture

which is controlled by pre-existing cracks (Atkinson, 1982). It is not necessary for stresses to be as high as those required for slip or twinning on a crystallographic system for cracks to propagate; propagation of a crack or a flaw can occur at lower stresses. The critical stress necessary for crack growth on pre-existing cracks is given by (Atkinson, 1982),

$$\sigma_c = \left[\frac{EG_c}{\pi a}\right]^{\frac{1}{2}} \qquad [15]$$

where all terms are defined as in previous sections. On the other hand, if pre-existing cracks are small or nonexistent then crack nucleation can occur when slip or twinning dislocations pile up at grain boundaries. For this case, the critical stress is given as (Atkinson, 1982),

$$\sigma_c = \left[\frac{EG_c}{\pi d}\right]^{\frac{1}{2}} \qquad [16]$$

where the crack half-length is proportional to the grain size, d. The critical stress for the second case is higher than that for the first case, this is because the crack half-length, a is greater than the crack half-length, d. Another type of fracture is that which is controlled by sliding along grain boundaries. In general, these types of cracks propagate in a stable manner until a critical length is reached at which unstable growth occurs as a cleavage crack.

In general, crack growth in geologic materials is dominated by slow, stable subcritical crack growth (Atkinson, 1982). The most predominant and well studied mechanism of subcritical crack growth in geologic materials is stress corrosion. Stress corrosion tensile crack growth of quartz can occur at values of 0.2 times the critical stress intensity factor (Atkinson, 1984). Typical crack growth rates or crack velocities for stress corrosion cracking of granitic rocks are on the order of 0.01 to 100 μm/s (Atkinson, 1982). Fundamental to stress corrosion cracking of geologic materials is the fact that all or at least a portion of the rock material is in tension (Atkinson, 1982 and 1984; Segall, 1984; Swanson, 1984).

Mechanism of Fatigue in Rocks: In a study of deformation and failure of rock in cyclic tension, Kim (1976) concluded that rock is a fatigue prone material. On the basis of acoustic emission characteristics of rock during cyclic tensile loading Kim suggested that fatigue of rock is not due to cyclic plastic deformation, but is due to the accumulation of microcracking. Furthermore, fatigue in tension can be divided into three main phases:

1. The first cycle is characterized by grain boundary loosening and the opening of pre-existing cracks with little crack nucleation. In the next few cycles, crack activity takes place at a decreasing rate. However, if the stress amplitude, S_a is sufficiently high failure will occur during the first few cycles due to the nucleation of a major crack.

2. Subsequent cycles are characterized by stable crack growth throughout the specimen.

3. During the last cycles before failure, microcracks nucleate into a major crack which propagates in an unstable manner resulting in failure.

Results from Kim's study indicate that cyclic tensile loading can significantly reduce the tensile strength of rock. For instance, the fatigue strength was 90 % of the dynamic tensile strength of Westerly granite under cyclic tension-tension limited to tens of cycles and 80 % of the dynamic tensile strength limited to hundreds of cycles (see Figure 2). Moreover, Kim studied the fatigue characteristics of rock under cyclic tension-compression. Failure was defined as the point at which the test specimen was visibly cracked and results indicated that failure always occurred under the tension part of the cycle by mechanisms similar to failure under cyclic tension-tension. Furthermore, test results indicate a significant reduction in the number of cycles required to bring about failure in cyclic tension-compression as compared to failure in cyclic tension-tension. For example, the fatigue strength was 85 % and 70 % of the dynamic tensile strength of Westerly granite under cyclic tension-compression limited to tens and to hundreds of cycles, respectively (see Figure 3).

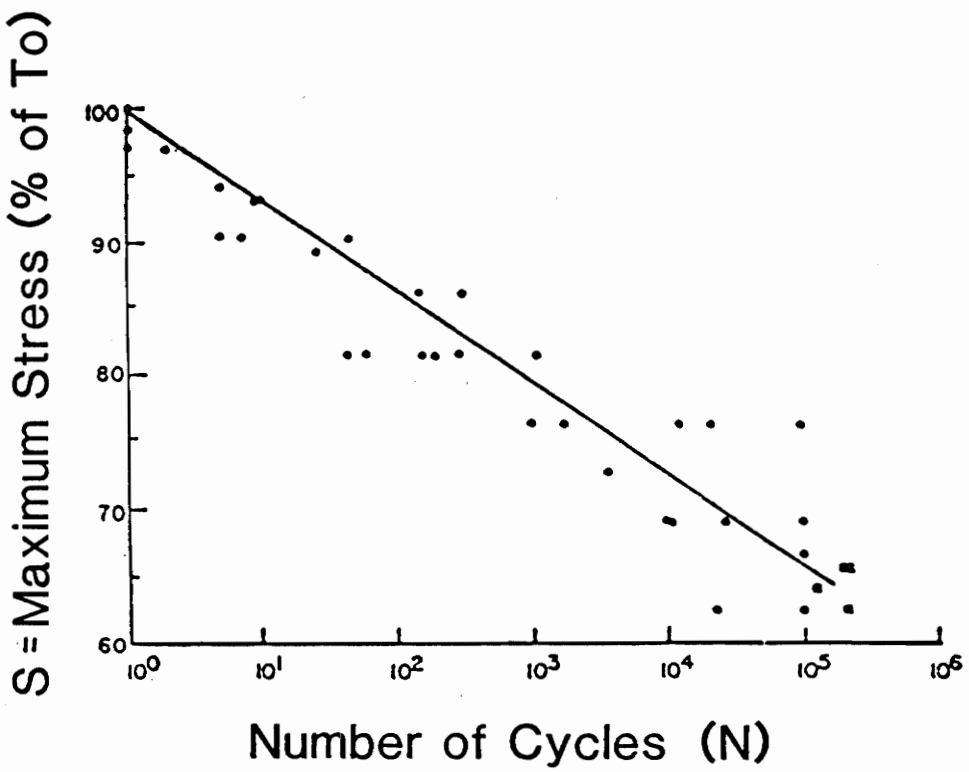

Figure 2. **Fatigue Failure of Granite in Cyclic Tension-Tension:** S-N characteristic curve of Westerly granite in uniaxial tension. S is the maximum stress in a cycle (fatigue strength) expressed as a percentage of the tensile strength, T_o and N is the number of cycles necessary to produce failure. Stress range = 2 MPa (from Kim, 1976).

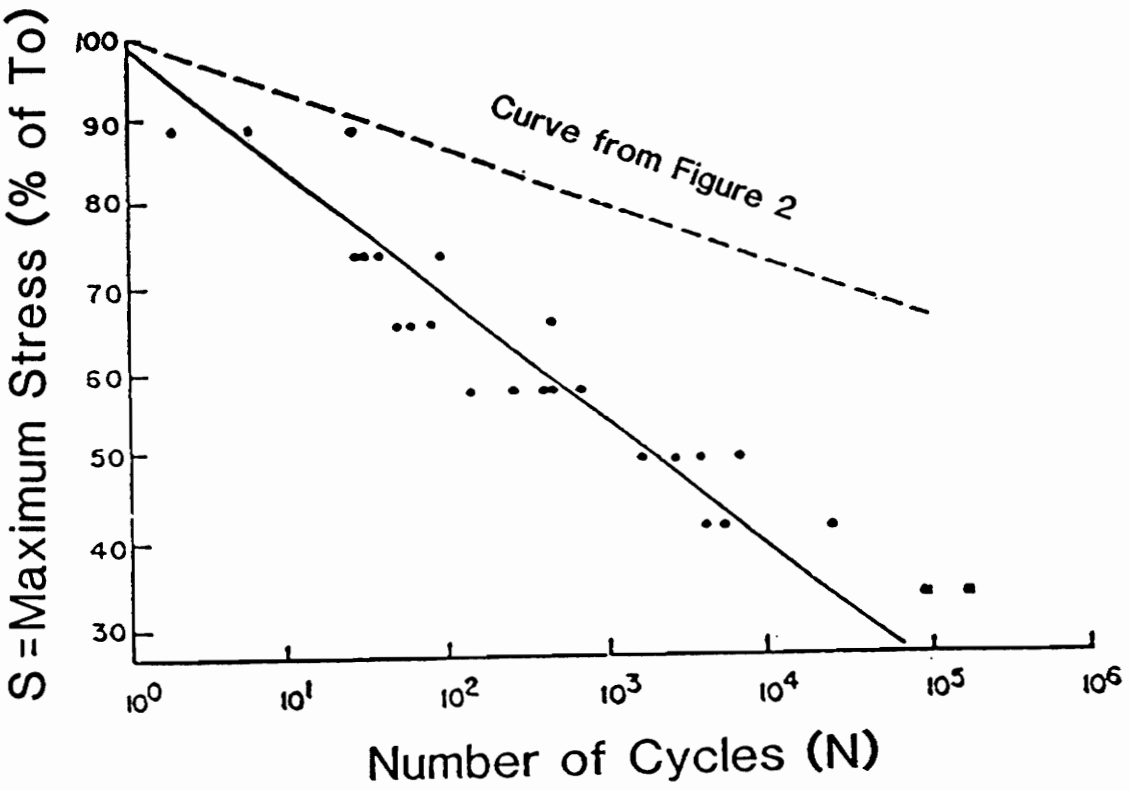

Figure 3. **Fatigue Failure of Granite in Cyclic Tension-Compression:** S-N characteristic curve of Westerly granite in cyclic tension-compression. S is the maximum stress in a cycle (fatigue strength) expressed as a percentage of the tensile strength, T_0 and N is the number of cycles necessary to produce failure. Stress range = 69 MPa. Note that the fatigue strength of granite in cyclic tension-compression is less than that in cyclic tension-tension (Compare to Figure 2) From Kim, 1976.

The Central Virginia Seismic Zone

The Central Virginia Seismic Zone (CVSZ), located in the fractured crystalline rocks of the Piedmont region of Virginia, is a spatially isolated zone of persistent low-level seismicity for which there is no obvious tectonic cause. In plan view the pattern of seismicity is roughly circular extending from Lynchburg, Va. in the west 150 km to Richmond, Va. in the east and approximately 120 km along a North-South axis (see Figure 4). The eastern boundary of the CVSZ ends rather abruptly at the fall line between the Piedmont and Coastal Plain provinces. The earliest reported seismicity in the historical record dates back to 1774 with the largest event a MMI VII, m_b = 5.0 which occurred on December 23, 1875 along the James River southeast of Scottsville, Va. Interpretations of a combined set of 130 hypocenters obtained by the Virginia Tech Regional Seismic Network (34 network determined hypocenters, 1978-1982, M $\leq$ 4.0 and 96 pre-network, pre-1978 earthquakes) suggest that the hypocenters exhibit a diffuse spatial distribution which is not due to errors or data set incompleteness (Bollinger and others, 1985). Consequently, this pattern suggests that multiple rather than singular seismogenic structures are present in the CVSZ. Furthermore, 75% of the focal depths are in the upper 10-15 km of the crust with the mean depth being 8 km. When coupled with seismic-reflection studies these multiple shallow sources suggest that the earthquakes occur above, in a series of associated listric ramp faults, and along a master detachment fault (Coruh and others, 1987, in review; Bollinger and others, 1983; Glover and others, 1979).

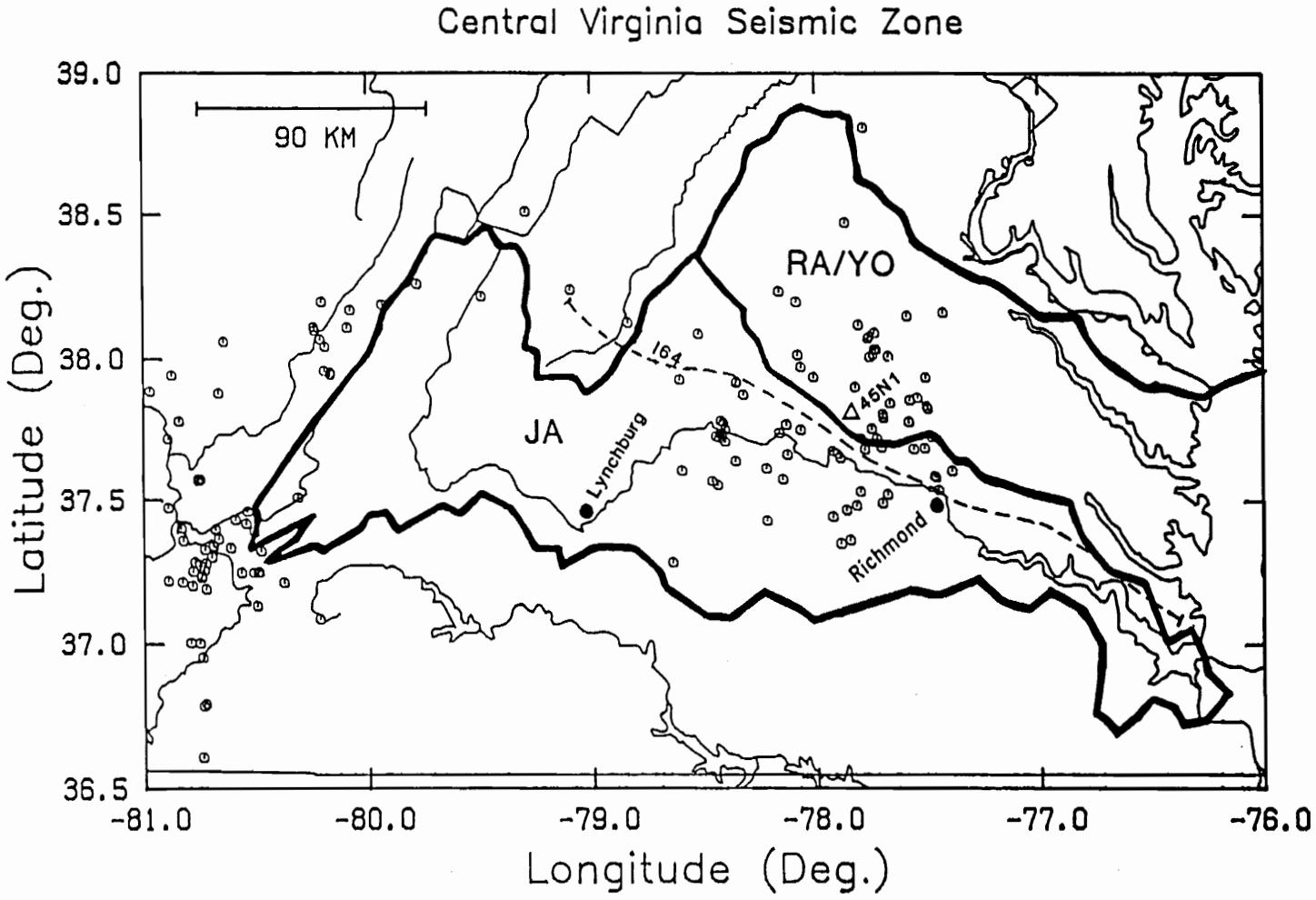

Figure 4. The Central Virginia Seismic Zone: Earthquake epicenter locations in central Va. from 1978-1985. Note that the CVSZ is totally enclosed by the James River drainage basin (JA) to the south and the Rappahannock/York River drainage basin (RA/YO) to the North. Dashed line indicates the location of the 164 seismic line shown in Figure 5. Data from the groundwater well 45N1 located in Louisa Co. is shown in Figure 6.

Moreover, the seismic-reflection data indicates that these faults have dips of 45° or less while focal mechanism solutions (Munsey and Bollinger, 1985) have nodal plane dips of more than 45°.

Results from focal mechanism studies also show scatter in both mechanism type and nodal plane orientation for the earthquakes in the CVSZ. For example, for shallow events ($\leq$ 8 km) the P-axes generally trend northeast, whereas for deeper events the P-axes generally trend northwest. Focal mechanisms are a mixture of strike-slip and dip-slip faulting on steeply dipping planes, 62° $\pm$ 16° (Munsey and Bollinger, 1985). The shallow events are mostly reverse faulting and the deeper events are mainly strike-slip faulting, a result consistent with the reorientation of the principal axes of stress with depth. Moreover, variability of the focal mechanisms suggest that small stress inhomogeneities are present in the CVSZ. The largest principal horizontal stress in the CVSZ is generally attributed to a ridge push force from the Mid-Atlantic Ridge. In-situ stress measurements from hydraulic fracturing tests indicate that the largest tectonic stresses are on the order of a few tens of megapascals oriented roughly west of northwest (Rundle and others, 1987).

Because the nodal plane dips as determined from focal mechanism studies differ from those interpreted from seismic-reflection profiles, Munsey and Bollinger (1985) suggested that the reflection profile is not imaging all of the seismogenic features. They further suggested that the steeper focal planes may be associated with near vertical dikes which are present in the CVSZ. This hypothesis is consistent with the reprocessed and subsequently reinterpreted I64 reflection-seismic line (see Figure 5) which suggests a correlation between earthquake hypocenters and a narrow relatively reflection free zone $\cong$ 12 km across and 6 km deep at the top extending to 30 km depth at the MOHO (Coruh and others, 1987, in review). This zone has been interpreted by Coruh and others to be a zone of near vertical dikes. Hypocenters which project onto this section of the seismic reflection profile exhibit near vertical distributions, thus corroborating the hypothesis of Munsey and Bollinger (1985). Coruh and others (1987, in review) further go on to suggest that earthquakes in the western portion of the CVSZ are related to a major antiformal structure as interpreted on the

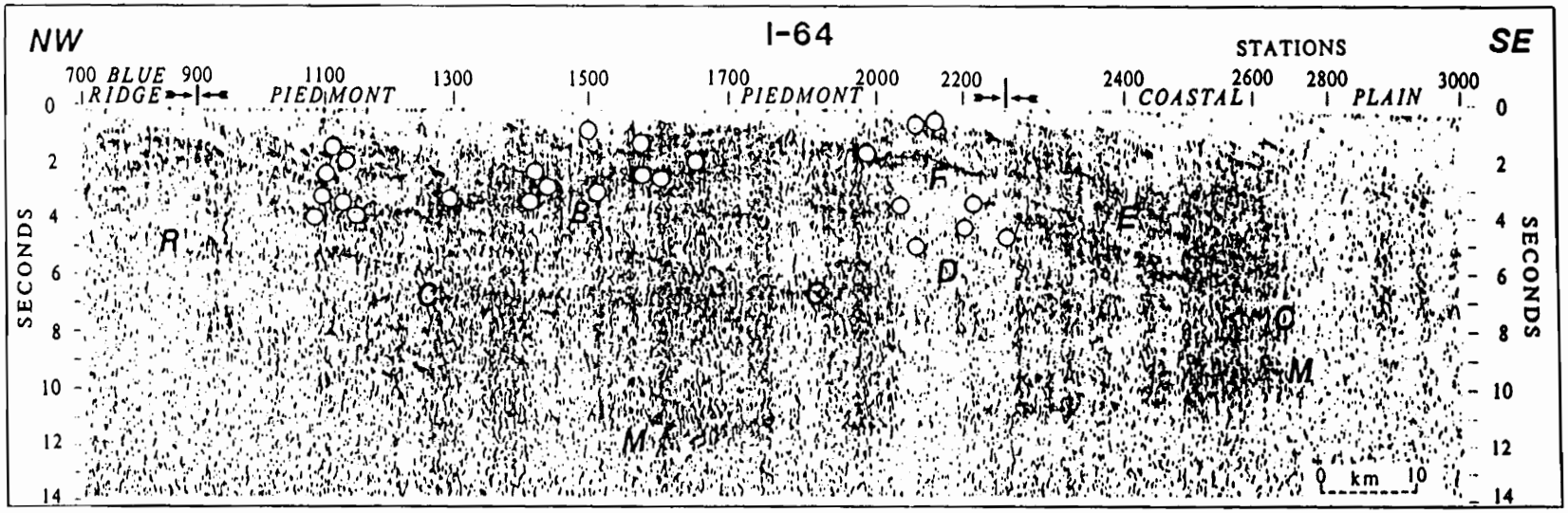

Figure 5. Subsurface Structure-CVSZ: Interstate 64 seismic line from Coruh and others (1987). Earthquake hypocenters are shown as white circles. Only those events with ERZ and ERH less than 5 km were projected on to the line. The line runs NW to SE through the CVSZ (see Figure 4)

I64 line. On the other hand, those earthquakes on the eastern side of the CVSZ are related to the dike swarm previously mentioned.

An interesting characteristic of the seismicity in the CVSZ is the fact that a tendency towards earthquake sequences and temporal periodicity has been observed. Of particular interest is the recent sequence of earthquakes that occurred in Richmond, Va. between December, 1986 and January, 1987. During this period there were eleven felt events, six of which were instrumentally recorded and four of these were instrumentally located. The four located events (duration magnitudes from 1.5 to 2.2) clustered within a five block area in downtown Richmond with focal depths $\leq$ 2.5 km. There were some associated foreshocks and aftershocks to these events. Focal mechanism results indicate reverse faulting on a N-NW trending plane dipping approximately 45° to either the northeast or southwest a result consistent with the aforementioned studies (Davison and Bode, 1987, in press). This sequence is interesting because it is unprecedented in the historical record for Richmond, Va. and because it occurred thirteen months after the flood of November, 1985 when the James River crested at 26 to 32 feet ($\cong$ 20 ft. above flood stage) in the area in which the earthquakes occurred. These river levels are the highest since the seismic recording network in central Virginia has been in place. This suggests a possible correlation between the river stage and this sequence of earthquakes.

Observational Data

The Central Virginia Seismic Zone is totally encompassed by the James River drainage basin (10,000 square miles) to the south and the Rappahannock/York river drainage basin (5,500 square miles) to the north. Together these drainage basins comprise 40 % of the total surface drainage area and 30 % of the total average daily flow in the Commonwealth of Virginia. Figure 4 shows the spatial relationship between these drainage systems and the CVSZ. A typical example of groundwater well records from a water table aquifer in central Virginia is given in Figure 6. If the

hypothesis that earthquakes in the CVSZ result from subcritical crack growth is correct then one would not expect to see a correlation between the occurrence of each earthquake and a high or low river stage level. Although each river stage maximum or minimum is responsible for the weakening of asperities, no single river stage can be expected to fracture a population of asperities. The weakening process is a continual one with each river level fluctuation contributing to this process. However, there may be a "cascading" effect that occurs. In other words, the weakest asperity among a population of asperities on a given fracture surface would fail and thereby redistribute the stress on the remainder of asperities. This sudden stress change may cause the remaining asperities to also fail in a catastrophic manner. Therefore, it is of interest to note the temporal relationship between the occurrence of seismicity and river stage. See Figure 7 for a plot of seismicity and river stage at the Richmond gaging station along the James River. On the other hand, a first pass at correlating total annual flow and seismicity in the CVSZ does indicate that years in which the total annual flow is comparatively high are followed by periods of increased seismicity (J. K. Costain, personal communication, 1987).

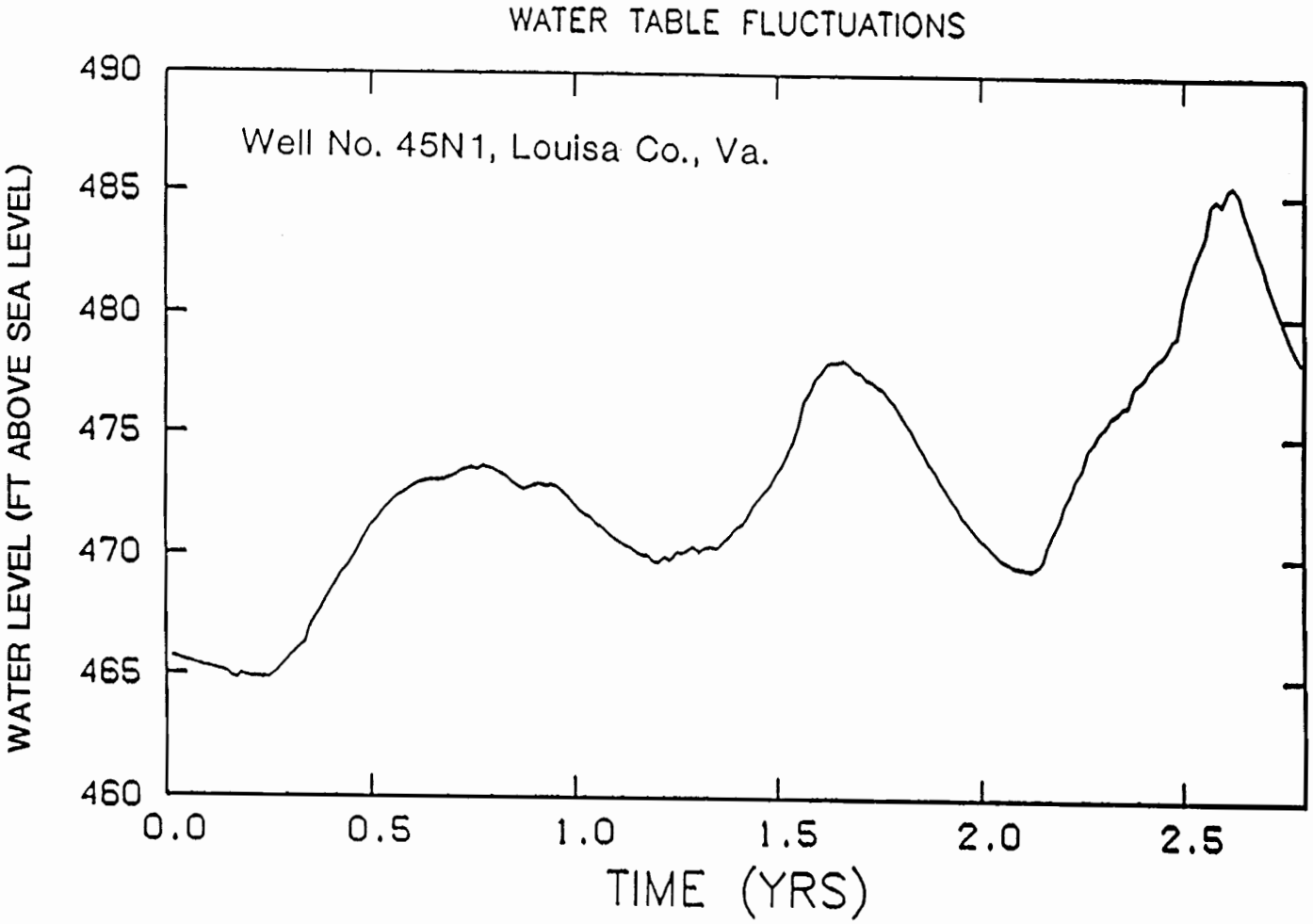

Figure 6. Typical Groundwater Well Record: Water levels from well no. 45N1 located in Louisa Co., Virginia along the surface drainage divide between the James and Rappahannock/York river drainage basins (see Figure 4). This well penetrates a water table aquifer within late Precambrian granitic rock. Note the annual periodicity.

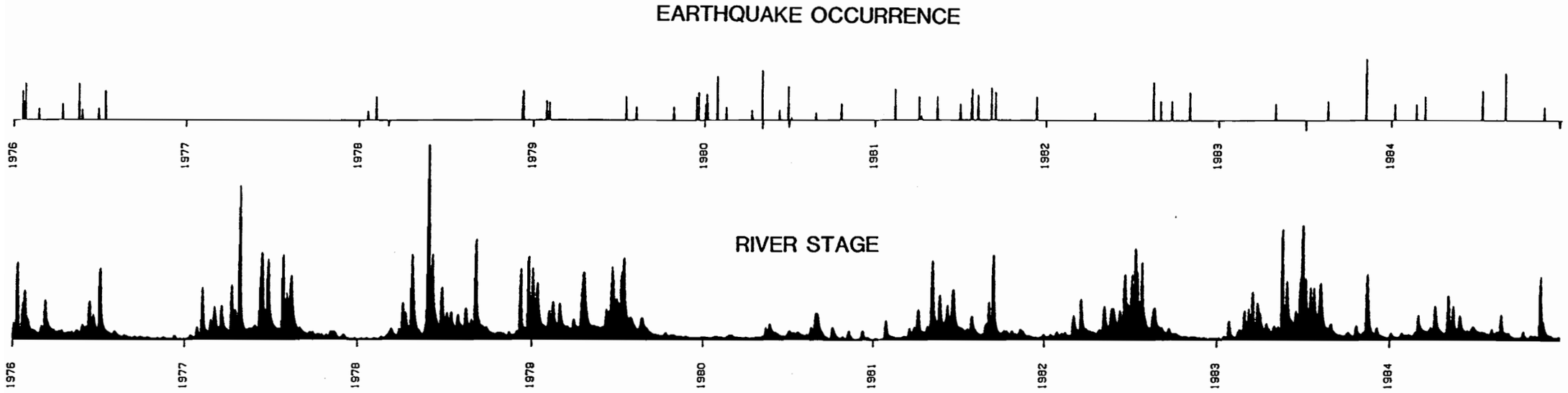

Figure 7. **Seismicity and River Stage:** The lower plot shows river stage level at the Richmond, Va. gaging station along the James river. The height of the line is proportional to specific discharge. Maximum stage roughly corresponds to a fluid pressure of 0.7 bars. Earthquake occurrence in the CVSZ is shown at the top and the height of the line is proportional to the magnitude of the event. Maximum magnitude event corresponds to $m_b = 4.0$. Note the annual streamflow periodicity.

Pore Pressure Transients

Permeability: As previously mentioned in the discussion on reservoir induced seismicity, Talwani and Acree (1985) calculated a narrow range of permeabilities associated with RIS on the order of millidarcys. These values are in agreement with those inferred on a crustal scale by Brace (1984) who states that in-situ measurements of permeability in crystalline rocks in the upper 2-3 km range from 10^{-5} to 10^{-1} darcys. These values are some 4 to 6 orders of magnitude higher than those inferred from laboratory measurements. Brace concludes that this discrepancy is due to the fact that on a field scale permeabilities are justifiably higher because of the contribution of fracture permeability which is too large to be sampled on a laboratory scale. In the Central Virginia Seismic Zone, which is a zone of highly fractured crystalline rocks, it is reasonable to expect the range of permeabilities to be at least as high as those given by Brace (1984) and Talwani and Acree (1985).

Pore Pressures: Biot (1941) developed the general theory governing the transient distribution of stress, water pressure and consolidation (settlement of a porous matrix under load) as a function of time. The following assumptions are inherent in Biot's theory: (1) material isotropy, (2) reversibility of the stress-strain relations under final equilibrium conditions, (3) linear stress-strain relations, (4) small strains, (5) the water is incompressible and (6) the flow of water is governed by

Darcy's Law. If we consider the one-dimensional case of a semi-infinite half space with no lateral expansion, an impermeable base and a free surface at the top then the fluid pressure must satisfy the diffusion equation (Biot, 1941),

$$\frac{\partial^2 P}{\partial z^2} = \frac{1}{C}\frac{\partial P}{\partial t} \qquad [17]$$

where

$$C = \frac{k\rho g}{\mu S_s} \qquad [18]$$

and P is pore pressure, z is distance below ground surface or along a flowline, t is time, S_s is the specific storage of the porous medium, μ is the dynamic viscosity of water, k is intrinsic permeability, ρ is the density of water and g is gravitational acceleration. Howells (1974), in an attempt to assess the order of magnitude of the time involved for a change in pore pressure at the Earth's surface to propagate to depths in the crust, used the above equation and assumed that a pressure P(0,t) is imposed at $z = 0$ and maintained for $t > 0$. The solution to this problem is given by

$$\frac{P(z,t)}{P(0,t)} = 1 - \mathrm{erf}\left[\frac{z}{2\sqrt{Ct}}\right] \qquad [19]$$

In this analysis Howells (1974) assumed that pore pressure was transmitted through any continuously linked channel regardless of its physical properties, origin or scale. The results from Howells' work are shown in Figure 8. The values represented by these curves are values of excess pore pressure, ie., those values in excess of hydrostatic as expressed as a percentage of the magnitude of the surface pressure source.

In Howells' work he assumed that the properties of water (viscosity and density) were constant with depth in the Earth's crust. However, the viscosity and density of water are functions of temperature and pressure and as such this functional dependence must be taken into consideration.

Assuming a geothermal gradient of 15°C/km, which is appropriate for the Piedmont region in central Virginia (Costain and others, 1986) the viscosity and density of water were calculated using the equations of Haar and others (1984). For a detailed discussion of this procedure refer to Appendix A. Using the appropriate values of ρ and μ the curves of Howells (1974) were recalculated (See Figure 8). One can see that the transient time necessary to propagate a pressure change from the surface to a particular depth is greatly reduced when the temperature and pressure dependence of ρ and μ are taken into account.

To assess the order of magnitude of the time involved in the propagation of a pore pressure pulse in the Central Virginia Seismic Zone, Howells' curves were reproduced using the end member permeabilities as given by Brace (1984) see Figure 9. Furthermore, as shown previously, the water table elevation exhibits a cyclic pattern with an annual periodicity (roughly 180 days on, 180 days off). One can consider the surface pressure source function to be a cyclic function and model the resulting pore pressures at depth. In Figure 10 and one can see that the cyclic nature of the surface pressure source function is transmitted to the pore pressure at depth.

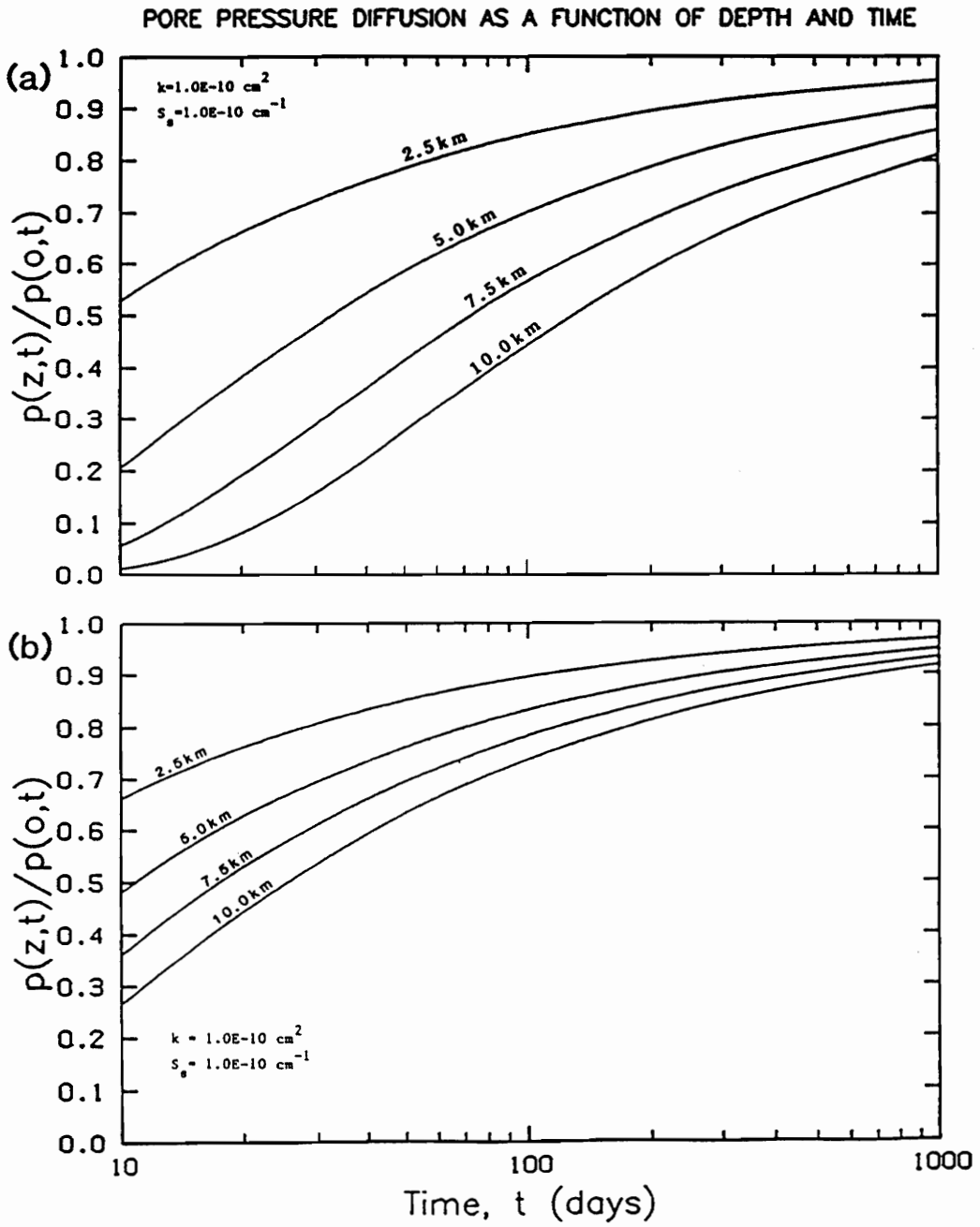

Figure 8. **Pore Pressure Diffusion:** Curves of excess pore pressure normalized to the surface pressure magnitude as a function of depth and time. In (a) fluid properties are constant, whereas in (b) fluid density and dynamic viscosity are functions of temperature and pressure. The geothermal gradient was taken as 15° C/km. Note the more rapid rise in pore pressure in (b). After Howells, 1974.

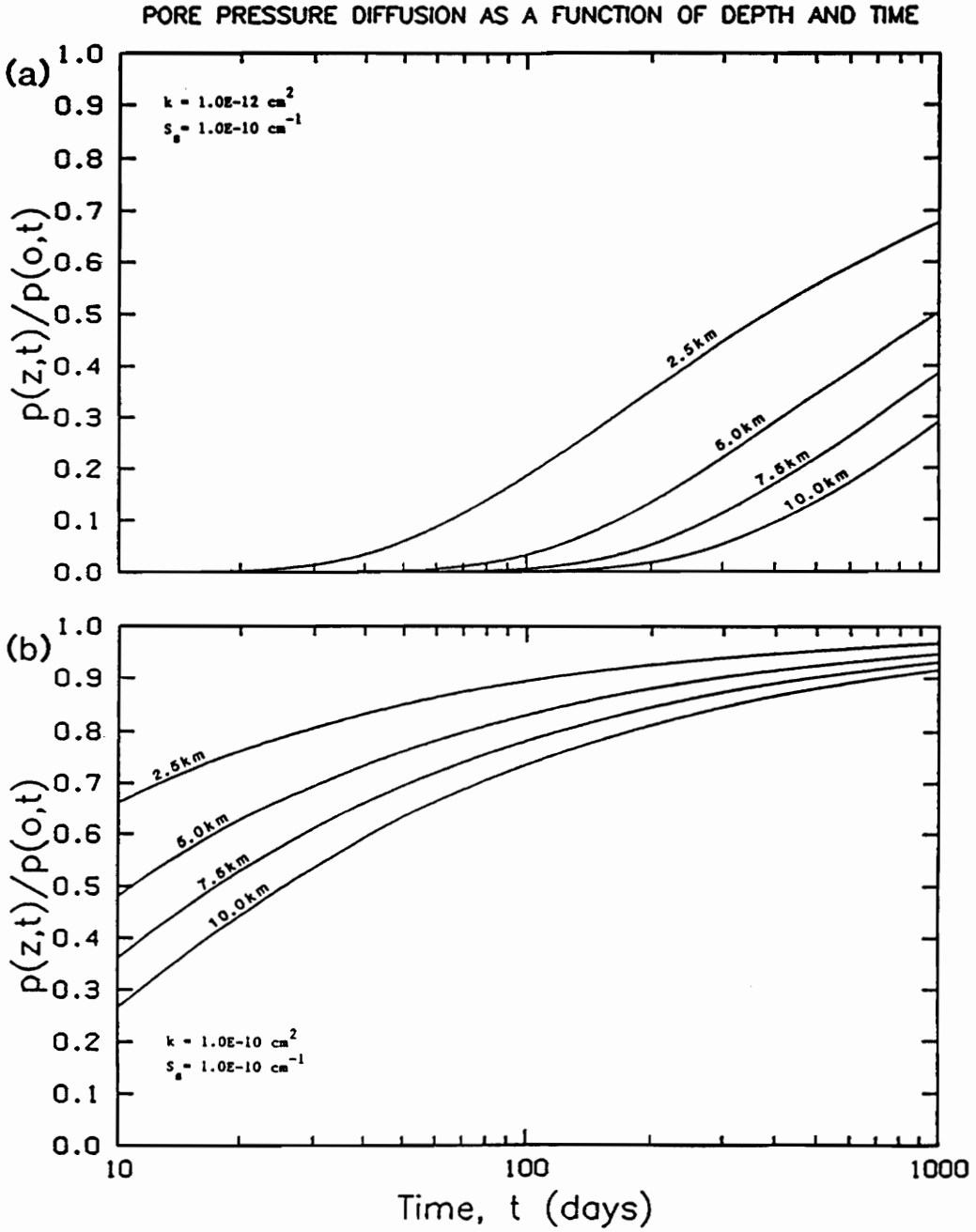

Figure 9. Pore Pressure Diffusion (End Member Permeabilities): Curves of excess pore pressure as a function of depth and time. Both density and viscosity are functions of temperature and pressure. These curves represent pore pressure diffusion using the end member permeabilities as given by Brace (1984). In (a) the permeability is 0.1 mdarcy and in (b) 10 mdarcy.

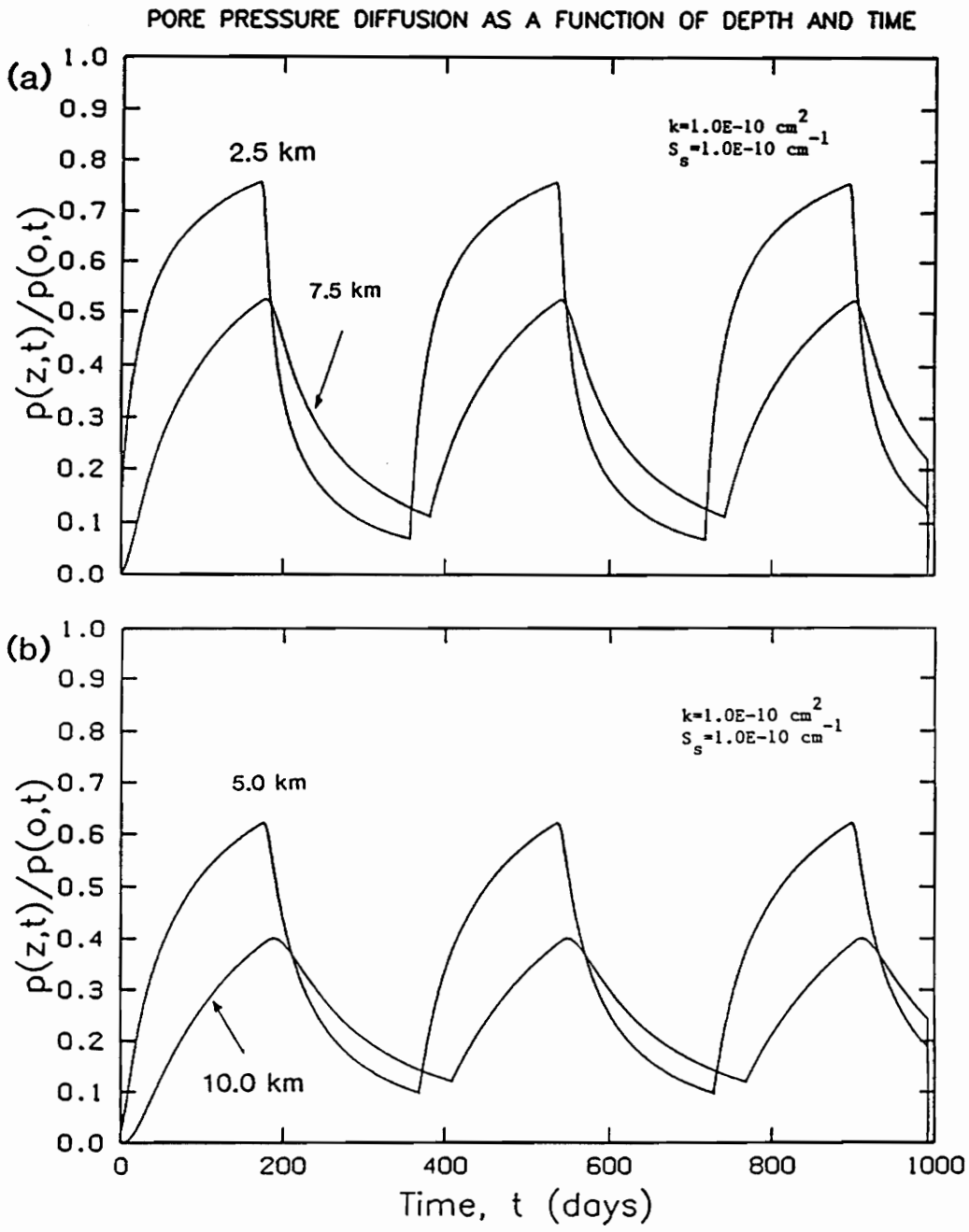

Figure 10. **Pore Pressure Diffusion (Cyclic Source Function):** Surface pressure source function modeled as constant for 180 days on and 180 days off through three cycles. (a) represents excess pore pressure at z = 2.5 and 7.5 km and (b) represents excess pore pressure at z = 5.0 and 10.0 km. Note the cyclic nature of the pore pressure at depth.

Stresses Within Asperities

For the purpose of this investigation asperities are modeled within vertical fractures and are assumed to have a rectangular cross section. The dimension perpendicular to the cross section is assumed to be much greater than either of the dimensions in the plane of the cross section. Moreover, the stresses which act in a direction perpendicular to the cross section are assumed to be negligible compared to those stresses acting within the plane of the cross section. Therefore, the asperity is assumed to be oriented such that the two largest principle stresses are in the plane of the cross section. Consequently, a plane strain analysis is used to model stresses within an asperity. The asperity is assumed to be composed of the same material as the rock composing at least one of the fracture walls. Consequently, one can expect the asperity to have the same general physical properties as the host rock. See Figure 11 for the asperity model used for the analyses. Porosity and permeability within the asperity is assumed to be primarily due to microcracks which are also present within the solid continuum (Simmons and Richter, 1976). In subsequent sections the stress magnitudes and distributions within an asperity will be investigated. As pressure transients diffuse from the Earth's surface along an open fracture network to depths in the crust it will encounter asperities and impart small pressure changes to and within the asperities. This is the source of the fatigue imposed on the asperity. Accordingly, the magnitude and extent to which a fluid pressure change affects the stresses within an asperity will also be examined.

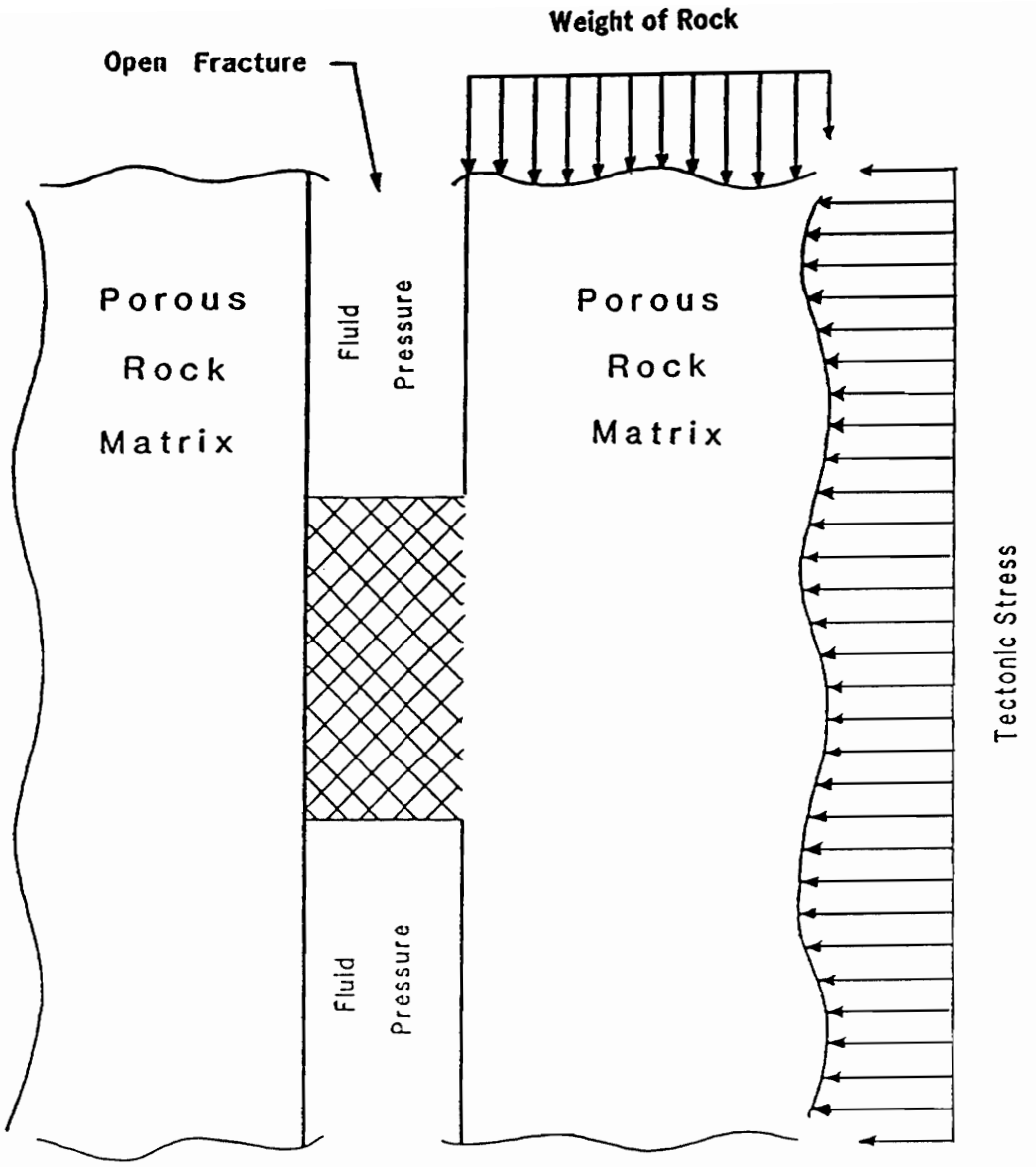

Figure 11. Schematic Model of Asperity and Loading Conditions: Cross section of a rectangular shaped asperity contained within a vertical fracture. Hachured area indicates asperity. The asperity has dimensions h by l which are much smaller than the dimension perpendicular to the paper.

Numerical Simulation Procedure: Numerical modeling of the interaction of fluid pressures and stresses was performed by the two dimensional finite element computer code STAFAN (Huyakorn and Lester, 1983). In STAFAN the governing equations of Biot (1941) are used. These equations can be written in the following form

$$G\frac{\partial^2 u_i}{\partial x_j \partial x_j} + (\lambda + G)\frac{\partial^2 u_j}{\partial x_i \partial x_j} - \frac{\partial p}{\partial x_i} = -F_i - \frac{\partial \sigma_{ij}^{o}}{\partial x_j} \qquad [20]$$

$$\frac{\partial}{\partial x_i}\left(\frac{k_{ij}}{\mu}\frac{\partial p}{\partial x_j}\right) = \varphi\beta\frac{\partial p}{\partial t} + \frac{\partial}{\partial t}\left(\frac{\partial u_i}{\partial x_i}\right) \qquad [21]$$

where u_i is solid displacement, p is fluid pressure, λ and G are Lame's constants, F_i is the body force, σ_{ij}^{o} is the initial effective stress, k_{ij} is the intrinsic permeability of the porous matrix, μ is the dynamic viscosity of water, φ is the effective porosity, β is the compressibility of water, x_i is the cartesian coordinate and t is time. For a complete derivation of the above equations the reader is referred to Appendix B. The constants λ and G can be written in terms of the more familiar elastic moduli, Young's modulus, E and Poisson's Ratio, ν as,

$$\lambda = \frac{E\nu}{(1 + \nu)(1 - 2\nu)} \qquad [22]$$

$$G = \frac{E}{2(1 + \nu)} \qquad [23]$$

STAFAN assumes the following,

1. Fluid flow is two dimensional, completely saturated Darcy flow where the fluid is slightly compressible (see Appendix B for further discussion).

2. Deformation in the rock matrix is linear and elastic with the deformation mode being plane strain.

3. Elastic material properties are isotropic.

4. The compressibility of the solid grains is negligible in comparison to the fluid compressibility (see Appendix B for further discussion).

5. The coupling coefficient $\alpha = 1$ (see Appendix B) meaning complete saturation; in other words, all void spaces are completely filled with fluid.

The above assumptions are commonly adopted to reduce the complexity of the physical problem; they are reasonable for use in predicting the interaction of fluid pressure and deformation (Huyakorn and Pinder, 1983).

The numerical technique employed by STAFAN to solve the governing equations of fluid flow and solid displacement is the Galerkin finite element technique. The solution procedure and numerical approximation technique consists of the following steps:

1. Discretization of the domain into a finite element mesh (as chosen by the user). A standard isoparametric quadrilateral element is employed with a maximum of three degrees of freedom per node (displacement in the x and y direction, u and v, respectively, and fluid pressure, p).

2. Formulation of the governing equations into a system of algebraic equations which describe element behavior.

3. Assembly of element equations into a system of global algebraic equations and imposition of boundary conditions.

4. Solution of the resulting set of algebraic equations for the primary unknowns (u, v and p).

5. Postprocessing: evaluation of secondary unknowns, ie., stresses.

The last four steps are performed for every time step and initial conditions are incorporated during the first time step. A finite difference time stepping scheme that will provide stable solutions with

second order accuracy in time (Huyakorn and Lester, 1983) is utilized to perform the transient analysis.

The stresses calculated by STAFAN are the effective stresses (Huyakorn and Lester, 1983). The effective stress can be written as $\sigma = \sigma_T - p$ where, σ is the effective stress, σ_T is the total stress and p is the fluid pressure. Accordingly, those stresses modeled by STAFAN are the stresses between the grains of the solid skeleton only. A change in pore pressure does affect the magnitude of the effective stresses within the solid matrix. For instance, if the total stress remains constant then an increase in pore pressure will result in a decrease in the effective compressive stress (or increase in the effective tensile stress) because of the relation $dp = -d\sigma$. As stated previously, in terms of crack growth a crack with internal fluid pressure, P is the equivalent of a crack with remote applied uniaxial tension, $T = P$; however, in the case of complex loading conditions such as our model asperity, it is necessary to examine the stresses in the solid matrix due to both the fluid pressure and the load stresses. Consequently, it is necessary to model the effective stresses.

For the asperity model it was assumed that the asperity was contained within a vertical fracture. The asperity and loading conditions are shown in Figure 11. The corresponding boundary conditions are shown in Figure 12. Also, the finite element mesh consisting of 240 nodes (15 columns by 16 rows) and 210 elements (14 columns by 15 rows) is shown in Figure 13. The stresses are calculated at the midpoints of the elements. In general, the finite element solution is an approximation to the exact solution to a physical problem. For the case of rectangular asperities the geometry of the problem is exactly represented and consequently the values of the primary unknowns calculated at the nodal points correspond to the exact solution at these points. Moreover, because the stress in each element is calculated using the primary unknowns they also correspond to the exact solution at the element midpoint. On the other hand, interpolation of the results between nodal points or element midpoints is an approximation. In STAFAN the interpolation between nodes is approximated by an interpolation function which is bilinear in x and y. Therefore, one must keep in mind that the accuracy of the solution between nodes (or element midpoints) is lim-

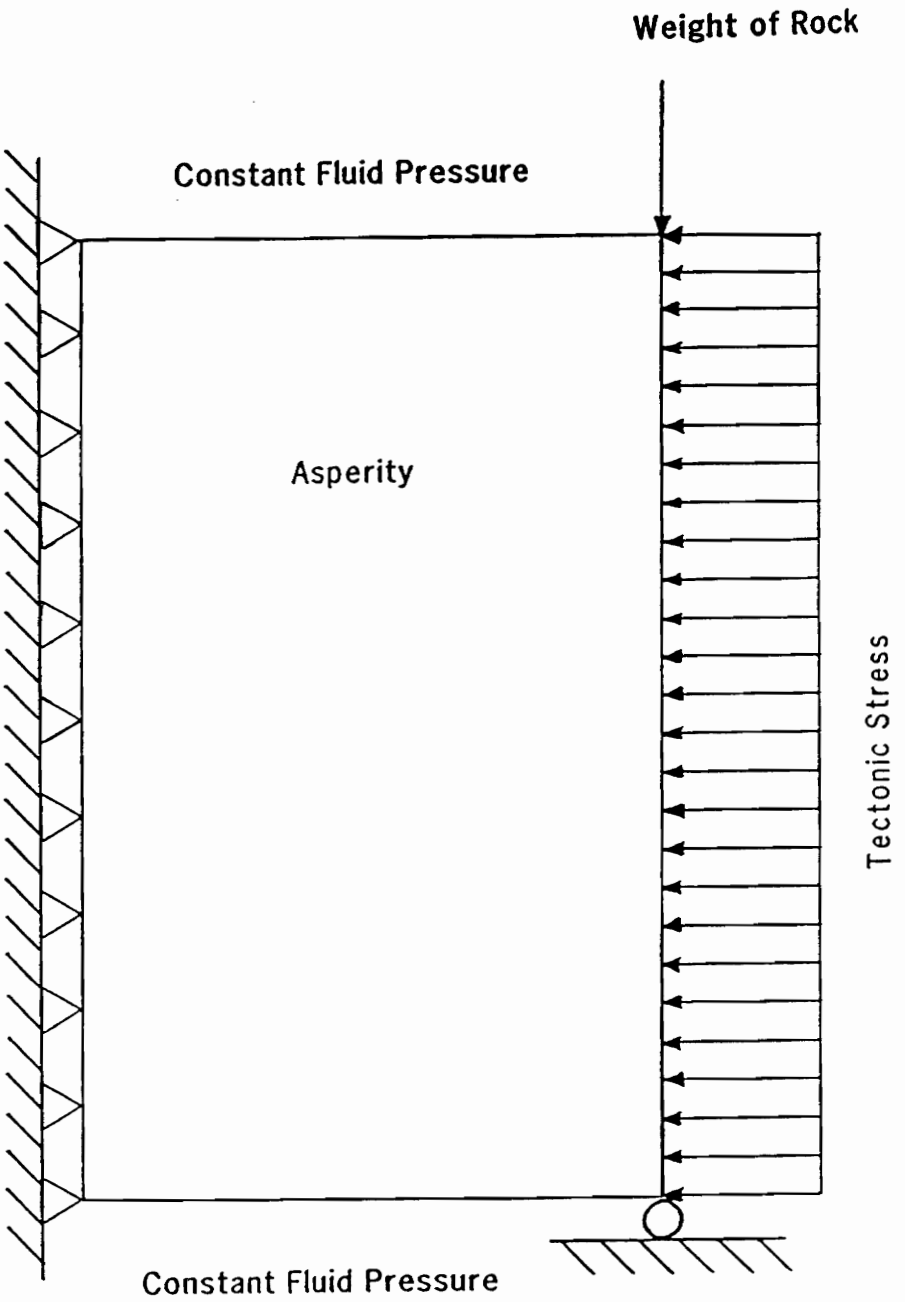

Figure 12. Asperity Boundary Conditions: Cross section of a single asperity on a vertical fracture showing boundary conditions used for modeling the interaction of solid deformation and fluid flow.

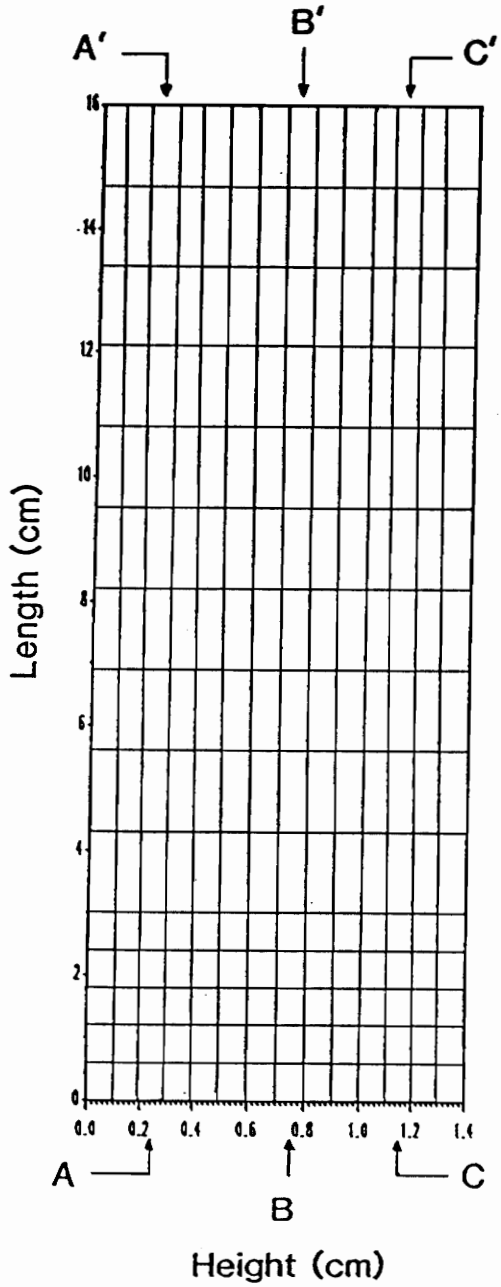

Figure 13. Finite Element Mesh for Asperity: Finite element mesh consisting of 240 nodes and 210 isoparametric quadrilateral elements used for the numerical analysis of the interaction of pore pressures and stresses within an asperity.

ited by a linear approximation. Consequently, any small scale anomalies or errant values in the graphical output presented in the analyses may be artifacts of the approximation procedure and not a real physical phenomenon. Accordingly, the results should be interpreted more in a regional overall sense rather than a small scale local sense. In addition, the number of elements and the size of each element can affect the accuracy of the solution. As the size of each element is decreased and the number of elements is increased the finite element solution will converge to the exact solution for the physical problem at hand. The finite element mesh used to model the asperities is the end product of several stages of refinement. Successive mesh refinement did not alter the numerical results and therefore the mesh shown in Figure 13 was deemed to be a satisfactory representation of the modeled domain.

We do not know the exact geometry of fractures and asperities at depth. Consequently, the following investigation and discussion is aimed at providing some insight into a model of stresses within asperities and how various factors can affect these stresses. An attempt is also made to assess how the following factors affect the final equilibrium state of effective stress within an asperity. We consider the following aspects of these problems:

1. What is the difference in the stress distributions and magnitudes between a dry rock asperity and a saturated asperity?

2. How do the stresses change with depth?

3. How are the stresses changed by an increase in pore pressure?

4. If the physical properties of the asperity are varied does this affect the stresses?

5. How does the height and length of a rectangular asperity alter the stresses within it?

6. How are the stresses affected by a change in the horizontal (tectonic) applied stress?

Results from (1) through (3) above are presented and discussed in the main body of the text. Results from (4) through (6) are presented in Appendix C.

The parameters used in the asperity modeling are given and discussed in Appendix D. Unless otherwise noted the horizontal applied stresses are taken to be 30 MPa which is consistent with the order of magnitude of the highest overall compressive horizontal stresses in the Southeastern U. S. (Haimson, 1978; Zoback and Zoback, 1985; Rundle and others, 1987). The size of the asperities modeled herein is on the order of tens to hundreds of cm^2. It was assumed that asperity size is probably on the order of the size of a given fracture aperture which is most likely a few cm at the largest. This is not to suggest that failure of a single asperity of this size will result in an earthquake; however, failure of a population of asperities (which may make up a larger asperity) could result in an earthquake. Because of the small asperity size, cgs units were used in the numerical modeling. Each of the numerical simulation procedures was performed using a transient analysis. The time discretization was performed using the following algorithm: $\Delta t_k = 1.414\,\Delta t_{k-1}$ where Δt_k is the k^{th} time step and $\Delta t_o = 60$ seconds. Initial conditions were zero displacement and fluid pressure everywhere in the medium. The boundary conditions were applied and in all cases equilibrium conditions were reached after no more than three time steps. For the case of an additional increase in fluid pressure, the initial conditions were the final equilibrium displacements and pressures from an appropriate model. Then, the additional pressure was added and the system allowed to go to equilibrium once again. The sign convention is negative for tensile stress and positive for compressive stress.

Results of Numerical Modeling

Results from this analysis are primarily in the form of graphical output. The stress distributions are given as contour plots. Stress magnitudes are shown along three vertical profiles through the asperity (see Figure 13). Because the stresses are calculated at the midpoints of the elements the

dimensions of the contour plots will not coincide exactly with the exterior dimensions of the asperity.

The stress distribution for a dry rock asperity is shown in Figure 14. This asperity was modeled as a 1.4 cm by 16 cm rectangle at a depth of 2.5 km. Note that there is a small zone of tension in the upper left hand corner of the asperity. This tension is due to extensional deformation in that region. Because the left side is rigidly attached, translation (rigid body motion) of this region is not possible and consequently the material expands to accommodate the vertical load applied in the upper right hand corner of the asperity. A saturated asperity with the same loading conditions and dimensions with the addition of fluid pressure equivalent to hydrostatic for 2.5 km is shown in Figure 15. The addition of fluid pressure within the asperity greatly increases the area of the asperity that is in tension (compare Figure 14 and Figure 15). Moreover, the magnitude of the compressive stresses are less in the saturated asperity than they are in the dry rock asperity. Also, some regions changed from compression in the dry rock asperity to tension in the saturated asperity (see Figure 16). Consequently, one can see that the assumption that the asperity is fluid filled is a critical assumption. **Pore pressure is the primary mechanism by which tension is developed within the asperity and, as previously mentioned, subcritical crack growth mechanisms operate primarily in tension.**

Two loading conditions change as the depth at which the asperities are modeled increases. The vertical load due to the weight of the rock increases and the hydrostatic fluid pressure increases. A common asperity size, 1.4 cm by 16 cm was used for the modeling. Stress distribution contour plots for $z = 2.5$ km, $z = 5.0$ km and $z = 10.0$ km are given in Figure 15, Figure 17 and Figure 18, respectively. Except for the upper and lower right hand corners, almost the entire asperity is in tension at $z = 10.0$ km. This is also true for the asperity at $z = 5.0$ km, however the zone of tension appears to be smaller than that at $z = 10.0$ km. Also, the percentage of the asperity area in tension for the asperity at $z = 2.5$ km is less than that for the other two. Stress magnitude plots are given in Figure 19. In general, the deeper asperities are associated with higher tensile stresses; however,

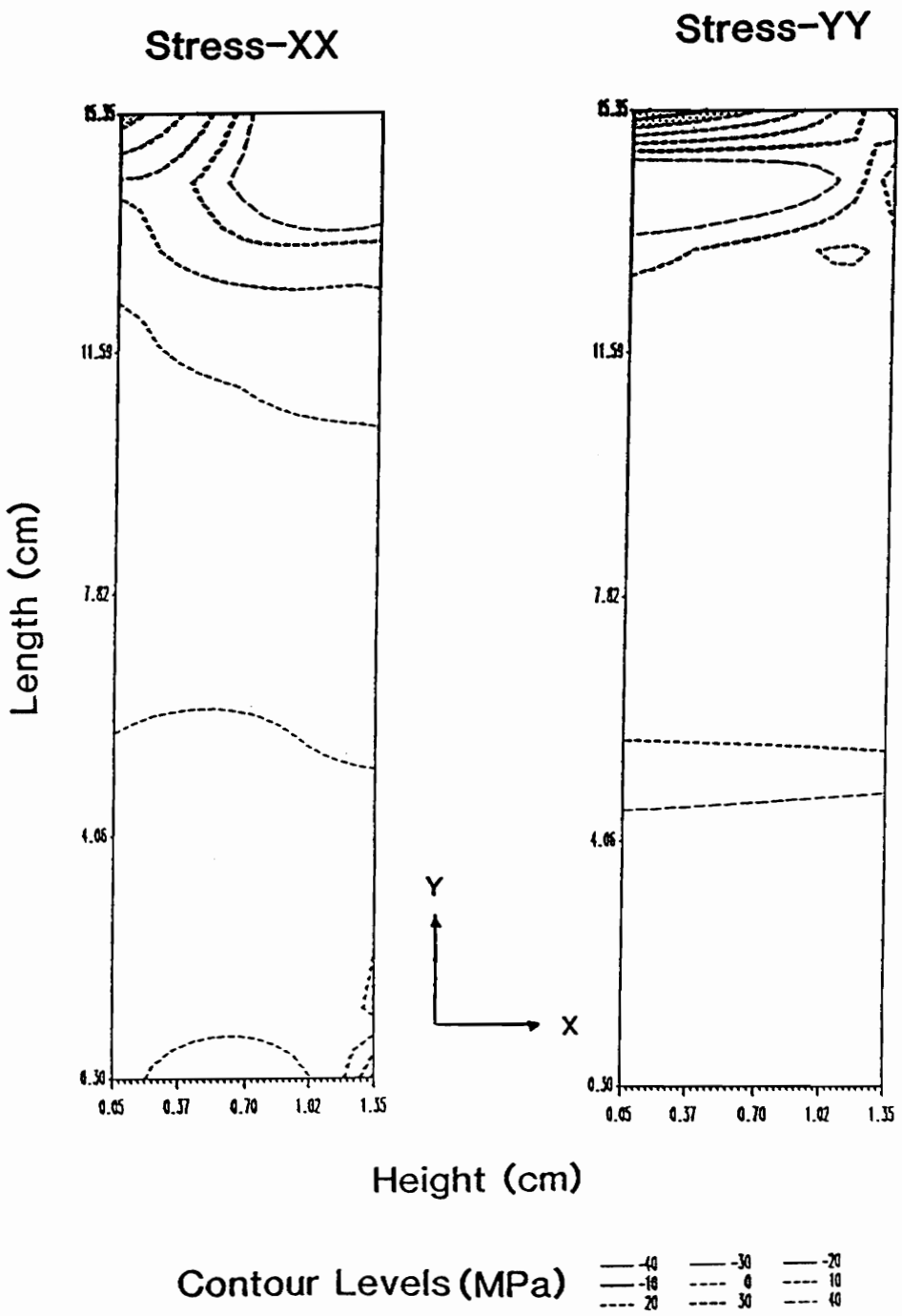

Figure 14. Stress Distribution-Dry Rock Asperity: Stress distributions within a 1.4 cm by 16 cm dry rock asperity at a depth of 2.5 km. Stress in the x-direction, σ_{XX} is shown on the left and stress in the y-direction σ_{YY} is shown on the right. Note the small zone of tension in the upper left hand corners. Stipples indicate tensile stresses.

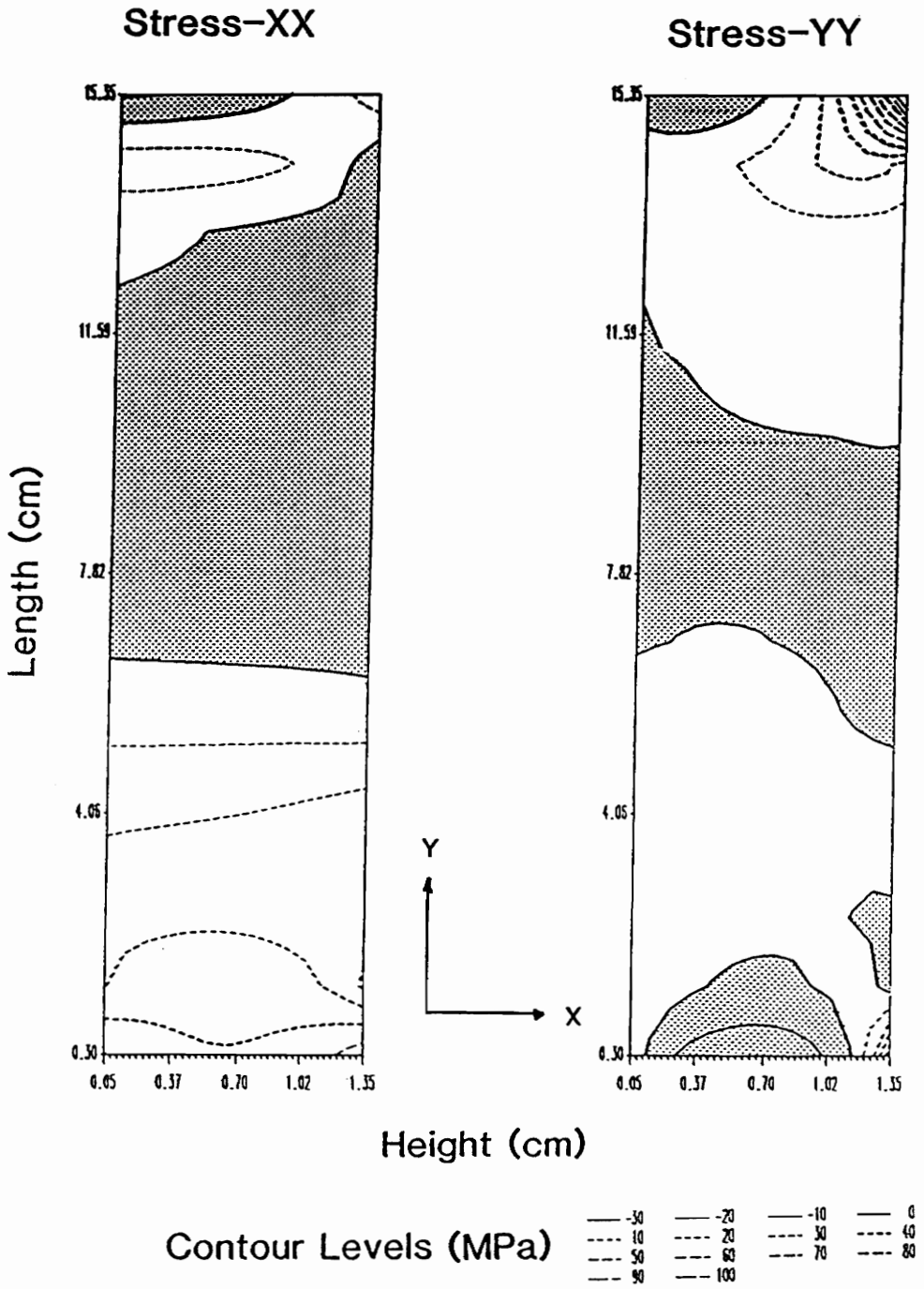

Figure 15. **Stress Distribution-Saturated Asperity:** Stress distributions within a 1.4 cm by 16 cm saturated asperity at a depth of 2.5 km. Fluid pressure is equivalent to hydrostatic at 2.5 km. σ_{XX} is shown on the left and σ_{YY} is shown on the right. Stipples indicate tensile stresses. Note that a larger portion of the asperity is in tension as compared to Figure 14.

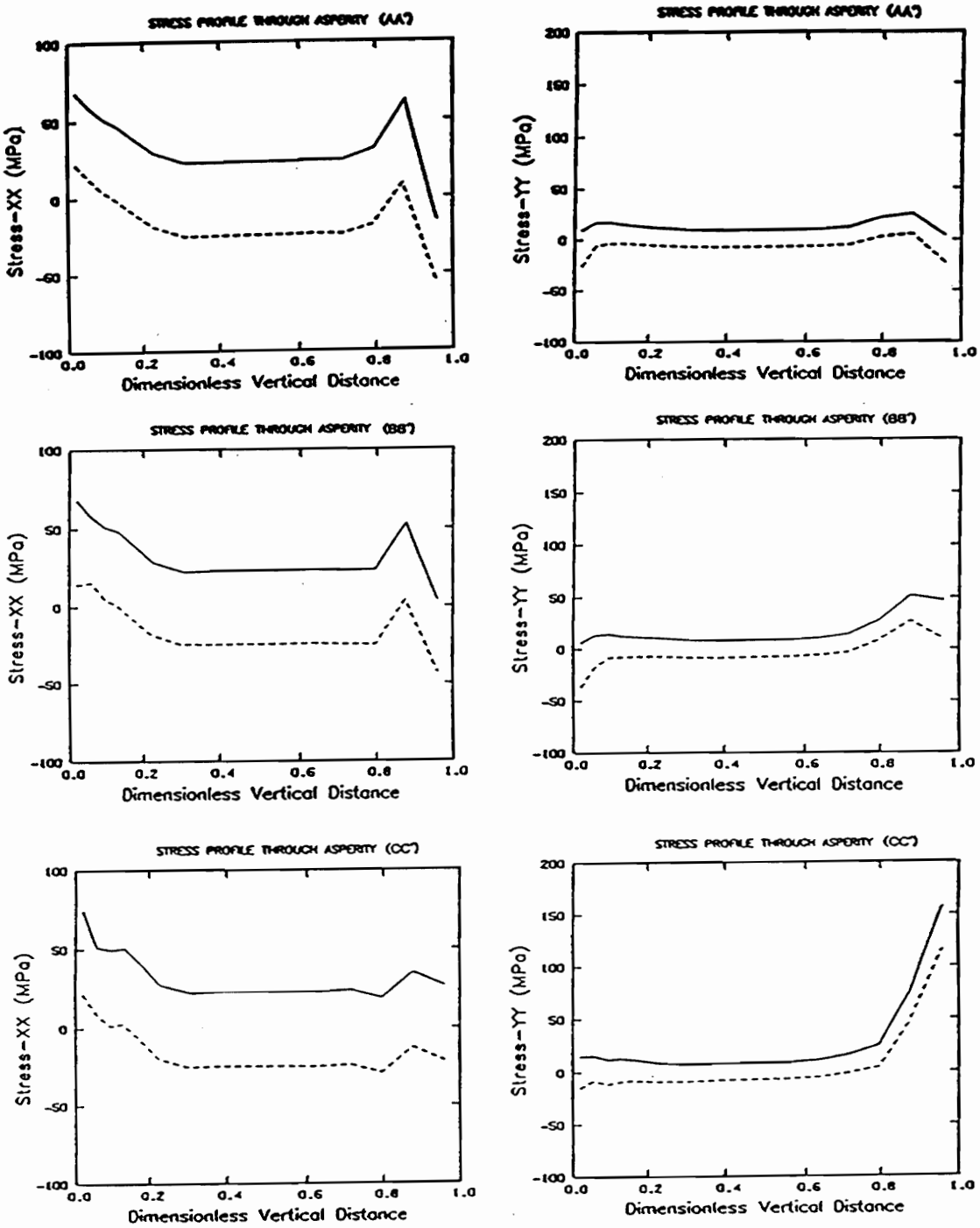

Figure 16. Stress Magnitudes-Dry Rock vs. Saturated: Stress magnitudes along three vertical profiles through the asperity. The solid line represents the magnitude of the stresses in the dry rock asperity, whereas the dashed line represents the stress magnitudes in the saturated asperity. Note that compressive stresses are lower and tensile stresses are higher in the saturated asperity.

the deeper asperities are also associated with higher compressive stresses. This is especially true for the stresses in the y-direction, σ_{yy} near the point of application of the load associated with the weight of the overlying rock.

Finally, the extent to which the stresses within an asperity change as a result of a fluid pressure increase was modeled. Once again, an intermediate asperity size, 1.4 cm by 16 cm, at z = 2.5 km was used for the modeling. The fluid pressure within the asperity was increased by four different magnitudes, dp = 0.025 MPa, dp = 0.050 MPa, dp = 0.075 MPa and dp = 0.1 MPa (= 1 bar). The stress distribution within the asperity is not affected to the extent that a change of stress is visible on the types of contour plots used in the previous analyses; however, the difference between the magnitude of the stresses resulting from hydrostatic fluid pressure, ie., σ_{hyd}, and the magnitude of the stresses resulting from fluid pressures at hydrostatic plus an additional increment of pressure, dp, ie., σ_{hyd+dp}, is appreciable. Accordingly, plots of the stress difference, $\sigma_{hyd} - \sigma_{hyd+dp}$, along a profile are given in Figure 20. As one might expect, the greatest pressure increase results in the greatest change in stress. Moreover, while not obvious from the plots, an increase in pressure increases the tensile stresses and decreases the compressive stresses. In general, an increase in pressure of 0.1 MPa or less results in a stress change on the order of 0.1 MPa or less. Therefore, if the surface pressure source function is cyclic and imparts cyclic pore pressures to asperities then this will in turn impart cyclic tensile stresses to the asperities. Consequently, a possible source of naturally occurring cyclic tensile stresses (fatigue) has been identified.

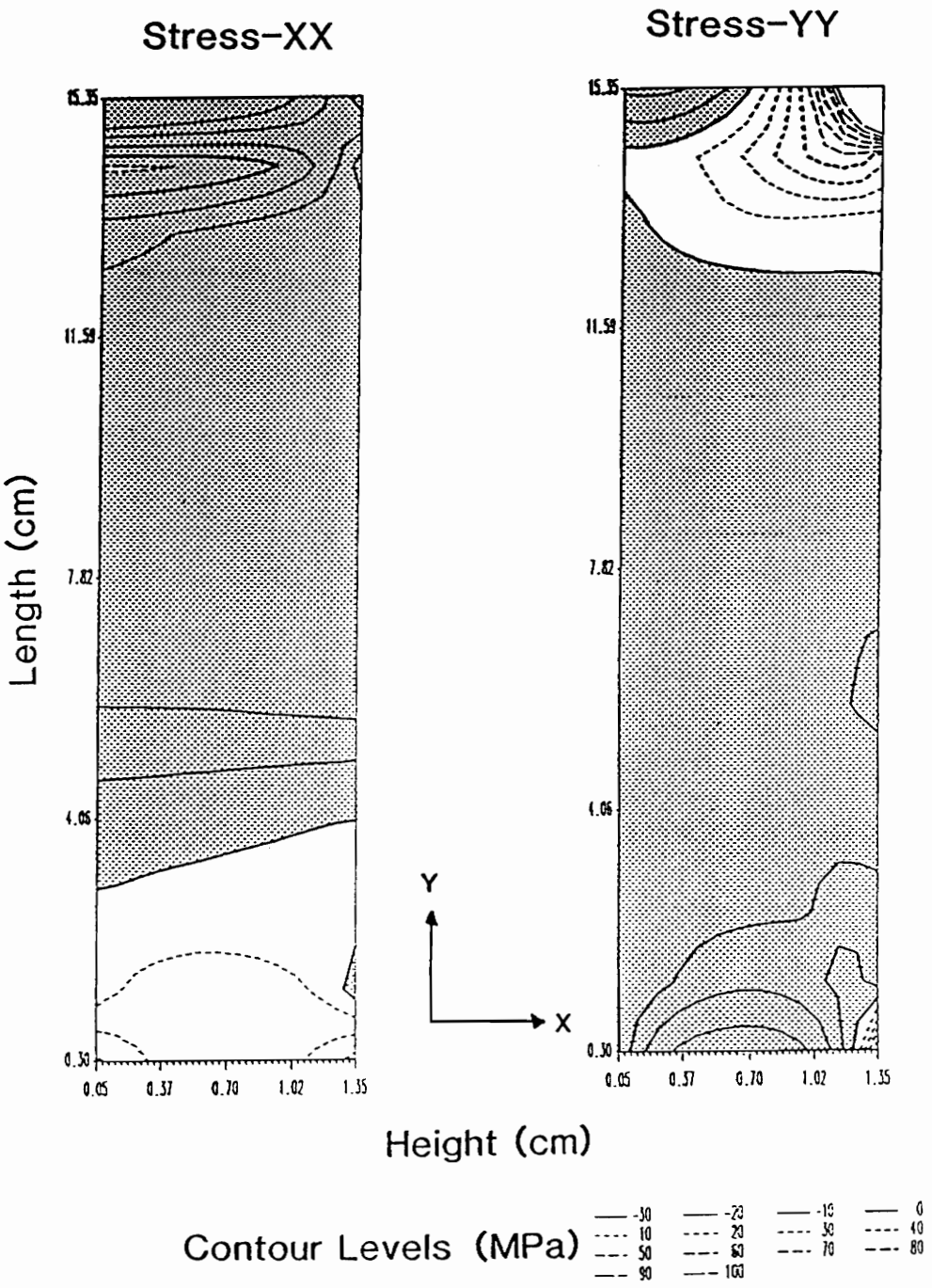

Figure 17. Stress Distribution (z = 5.0 km): Stress distribution within a 1.4 cm by 16 cm saturated asperity at a depth of 5.0 km. σ_{xx} is shown on the left and σ_{yy} is shown on the right. Stipples indicate areas of tension. Compare to Figure 15 and Figure 18 to see the effect of depth on the stress distribution within an asperity.

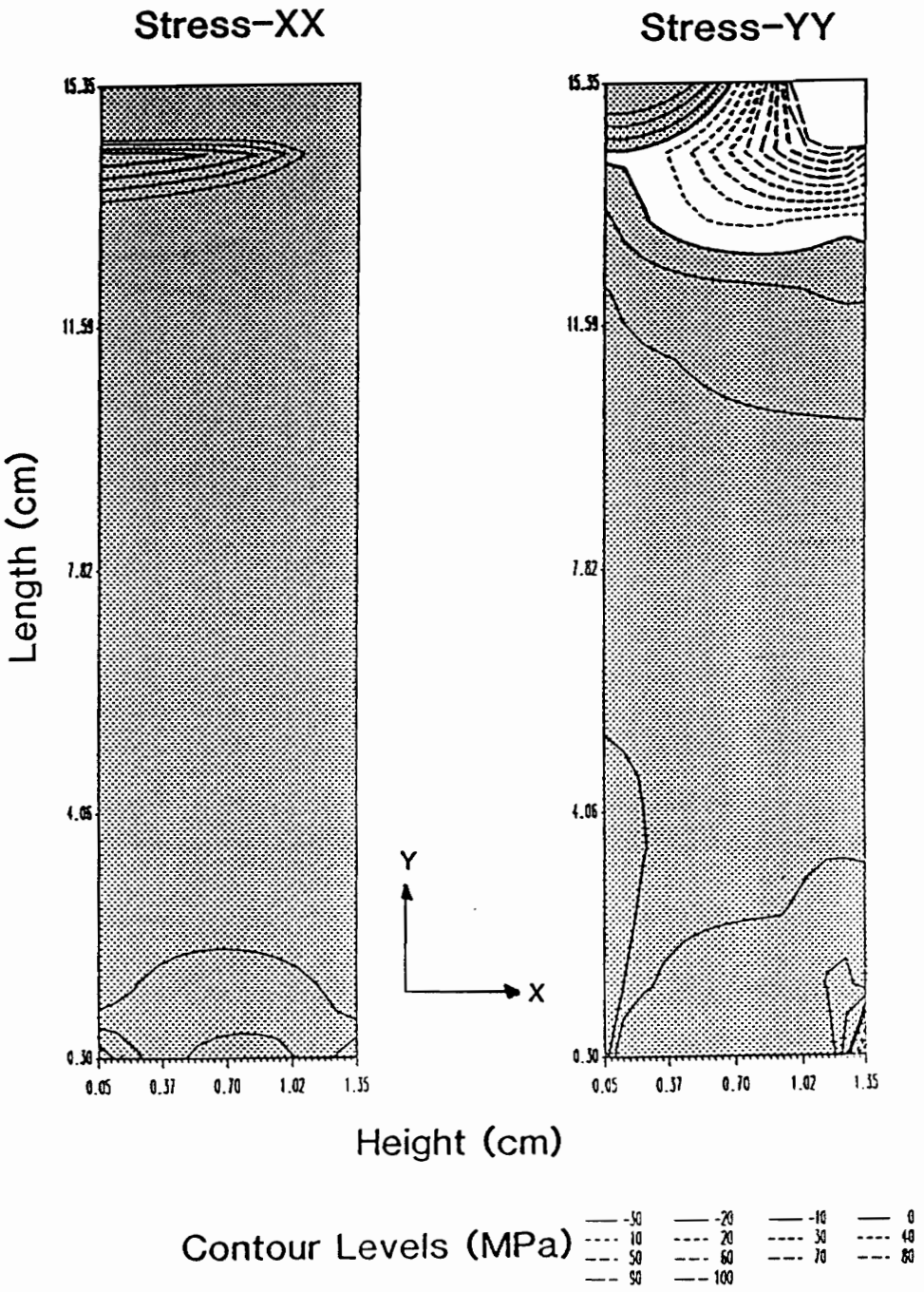

Figure 18. Stress Distribution (z = 10.0 km): Stress distribution within a 1.4 cm by 16 cm saturated asperity at a depth of 10.0 km. σ_{xx} is shown on the left and σ_{yy} is shown on the right. Stipples indicate areas of tension. Compare to Figure 15 and Figure 17 to see the effect of depth on the stress distribution within an asperity.

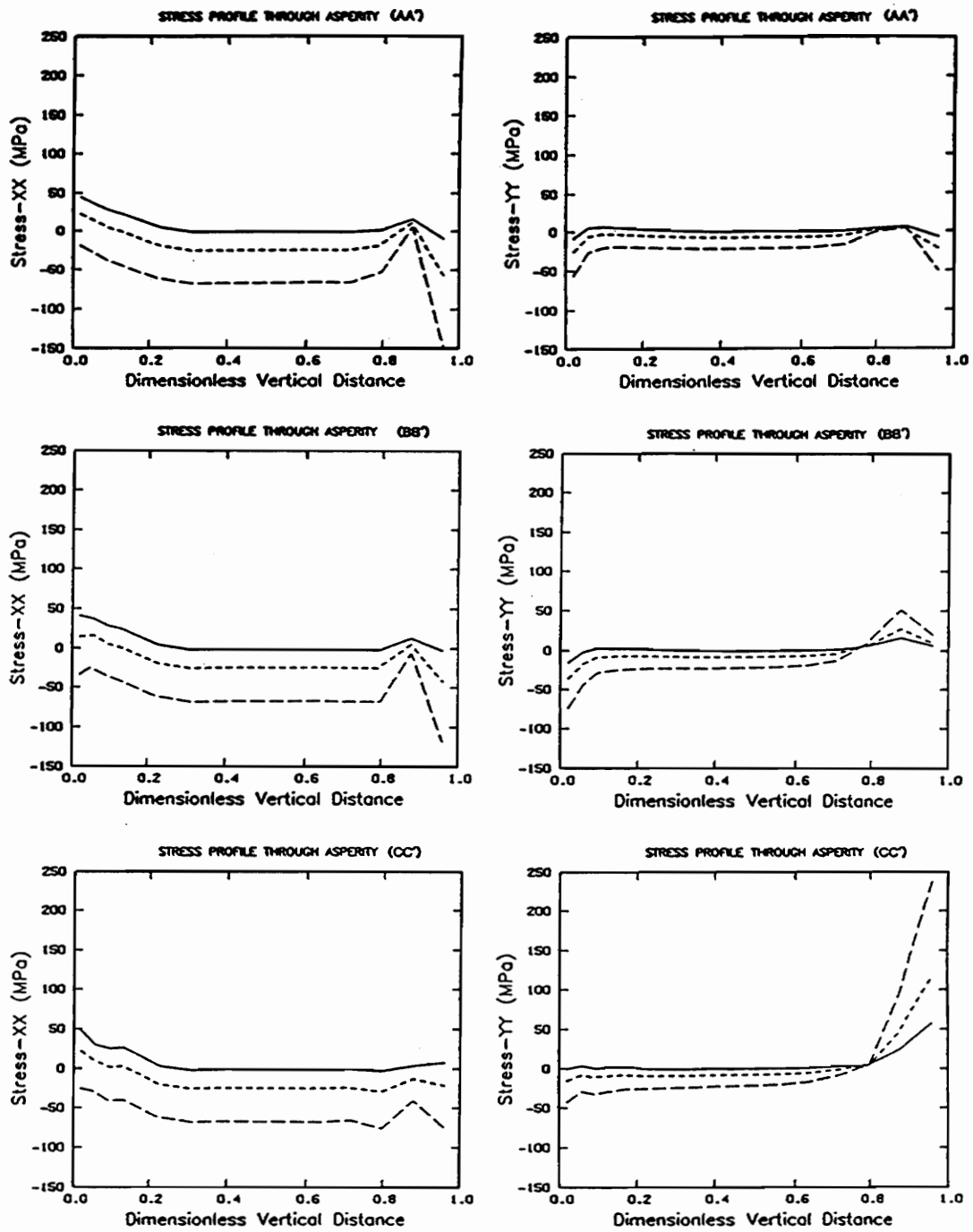

Figure 19. Stress Magnitudes for Asperities at Different Depths: Stress magnitudes along three vertical profiles through asperity. Solid line--z = 2.5 km, short dash--z = 5.0 km, long dash--z = 10.0 km. Note that deeper asperities are associated with both higher tensile stresses and higher compressive stresses.

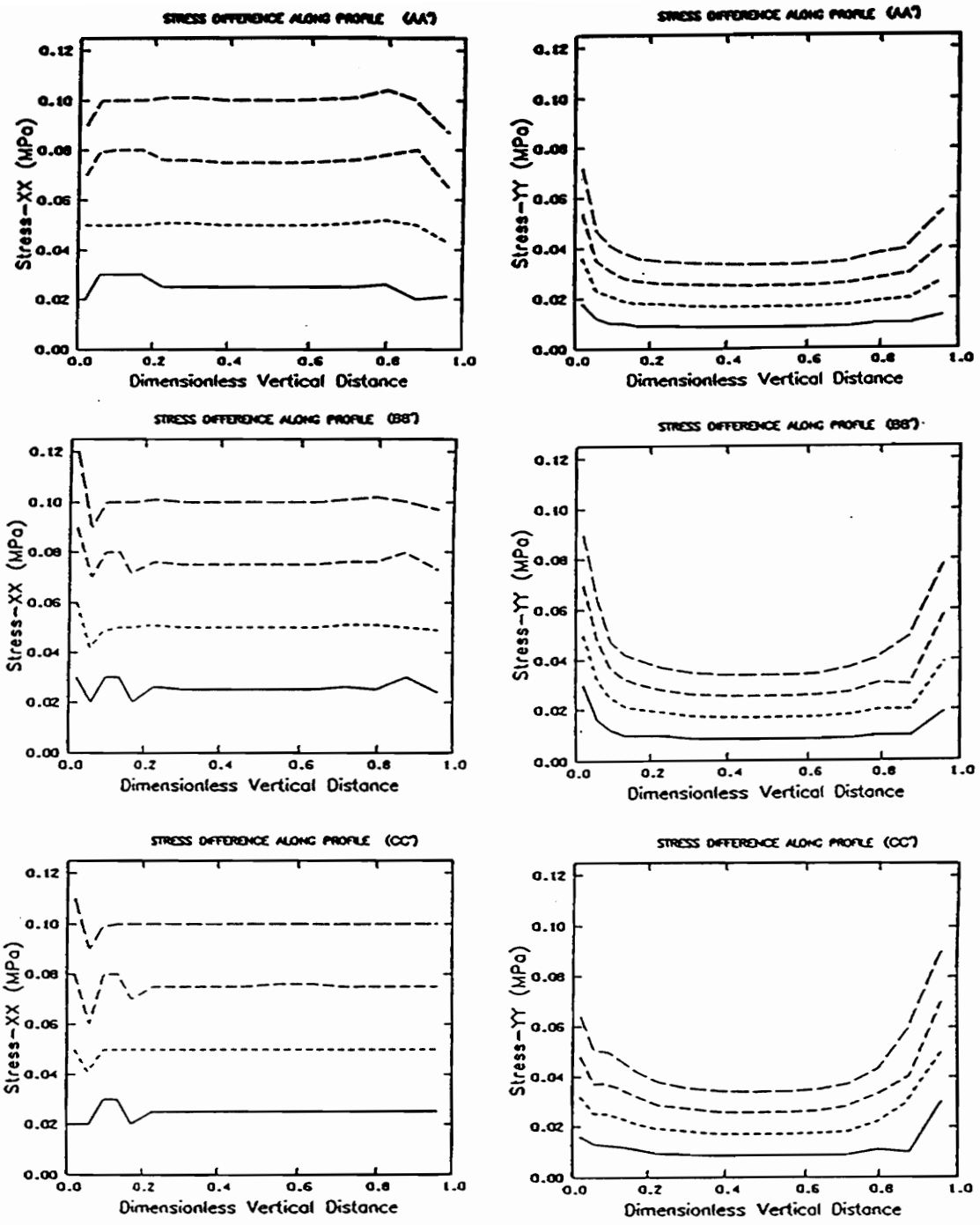

Figure 20. Stress Difference due to Pressure Change: The difference between σ_{hyd}, the stress in the asperity due to hydrostatic fluid pressure and $\sigma_{hyd + dp}$, the stress due to hydrostatic fluid pressure plus an additional increment of pressure, dp. Solid line--dp = 0.025 MPa, short dash--dp = 0.050 MPa, middle dash--dp = 0.075 MPa and long dash--dp = 0.1 MPa. An incremental increase in pore pressure raises the effective tensile stress.

Discussion

As shown in the discussion on linear elastic fracture mechanics (LEFM) applied to crack growth, there are a number of experimental crack growth parameters which must be determined before an LEFM analysis can be performed. Furthermore, there is widespread scatter in these experimental results and, as such, experimental procedures must be tailored to the material, crack growth mechanism and in-situ environment under investigation (Ewalds and Wanhill, 1984). Consequently, a quantitative analysis of failure by fatigue crack growth is not possible without detailed experimental data; however, it is possible to state the important results from this study and to present a qualitative discussion of these results.

As previously stated, Kim (1976) pointed out that rock is a fatigue-prone material. Accordingly, if rock is subjected to cyclic tensile stresses one must consider fatigue as a subcritical crack growth mechanism by which failure may occur. It has been shown in the analysis presented in this paper that it is possible that cyclic variations in the elevation of the water table (or river levels) can impart cyclic pore pressure changes at depth within the Earth's crust. Furthermore, a change in pore pressure was shown to change the stress magnitudes within an asperity. Consequently, cyclic pore pressure changes can cause cyclic stress variations within an asperity. Therefore, it is possible that fatigue crack growth can occur as a result of natural "hydraulic pumping". Also, it is more likely

that grain boundary cracks will be most susceptible to this type of loading. Kim (1976) suggested that fatigue in rocks due to mechanical cyclic tension is characterized by grain boundary loosening and the growth of grain boundary cracks. Because the effective stress is an intergranular stress, this type of crack growth is even more likely to result from an increase in the tensile effective stress. Therefore, it seems that hydraulically induced fatigue should occur more readily than pure mechanically induced fatigue.

A change in pore pressure of 0.1 MPa (1 bar) or less within an asperity was shown to cause a change in the effective stress on the order of a few one hundredths of a megapascal. Tensile stresses within an asperity range from on the order of several megapascals at $z = 2.5$ km to roughly tens of megapascals at $z = 10.0$ km. The fatigue data of Kim (1976) can be expressed in the form

$$S = 100 - 7 \log N \qquad [24]$$

where S is the maximum tensile stress in a cycle expressed as a percentage of the monotonic tensile strength of the material and N is the number of cycles at failure. The tensile strength of Westerly granite is approximately 11 Mpa (Kim, 1976); the in-situ tensile strength of a granite gneiss in the CVSZ as given by Rundle and others (1987) is approximately 17 MPa. There is general agreement that the tensile strength of rock increases with increasing depth, although there is widespread disagreement about the order of magnitude of this change (Atkinson, 1984). Because there are so many unknowns involved, an accurate assessment of the number of cycles necessary to produce failure of an in-situ asperity is impossible; however, to get a feel for the number of cycles to failure a rough calculation can be performed. If we consider a 1.4 cm by 16 cm asperity at $z = 5.0$ km the average tensile stress in the interior of the asperity is on the order of 13 to 15 Mpa. Now, if we consider the tensile strength of rock at 5.0 km to be 17 MPa then solving for N from the equation above, the number of cycles to failure is approximately 2000 and 50 for 13 and 15 MPa, respectively.

There are various in-situ conditions which one can reasonably expect to reduce the number of cycles required for failure. First, fatigue crack growth is enhanced by the presence of a liquid en-

vironment that causes stress corrosion. Therefore, stress corrosion, which has been put forth by Costain and others (1987) as one of the principle subcritical crack growth mechanisms in the Hydroseismicity hypothesis, acting in concert with fatigue could, in principle, significantly reduce the number of cycles to failure. Also, environmental effects e.g., stress corrosion and hydrolytic weakening, are enhanced by low-frequency fatigue cycles. In the fatigue tests of Kim (1976) a frequency of 1 Hz was used whereas the annual water table elevation cycle has a frequency of 3×10^{-8} Hz; consequently, this could also accelerate the crack growth process. Moreover, fatigue in rocks is generally attributed to grain boundary crack growth (Kim, 1976). Therefore, an increase in the intergranular tensile stress (due to a pore pressure increase) should also accelerate the fatigue process.

Even though a detailed analysis of the "time to failure" can ultimately not be performed, several important conclusions from the numerical analysis presented herein with implications for the Hydroseismicity hypothesis have resulted. Probably the most important result is the fact that a significant portion of a saturated asperity is in tension which results primarily from the influence of pore pressure. Stress corrosion and hydrolytic weakening, which have been proposed by Costain and others (1987) to be the principal failure mechanisms, require tensile stresses and a fluid environment in order to operate. Furthermore, it has been shown that small transient increases in pore pressure on the order of a fraction of a MPa can increase the intergranular effective tensile stresses on the order of a fraction of a Mpa. Therefore, this provides additional credence to the idea that a small transient increase in fluid pressure at depth may trigger earthquakes by raising the tensile stresses within a sufficiently weakened population of asperities and cause failure. Also, an asperity/fatigue failure earthquake model might account for the tendency in the CVSZ for earthquake sequences and periodicity. Conceptually, it seems that failure first would occur in a small group of asperities leading to small earthquakes or foreshocks to a main event. As the stresses redistribute small earthquakes will continue to occur until a new state of equilibrium is reached. Thus, asperity failure could produce a sequence of small foreshocks and aftershocks to a main event. Moreover, once a new equilibrium state is reached the weakening process will restart. This

process of weakening, failure, return to equilibrium and restart may explain the tendency towards periodicity in the CVSZ.

This model of asperity failure by subcritical crack growth may also provide answers and/or insight into some previously unexplained phenomena associated with reservoir induced earthquakes. In contrast to naturally occurring intraplate seismicity such as in the CVSZ where it is not known when the first fatigue cycle began, the loading history of a reservoir is precisely known. For example, see Figure 21 and Figure 22. Evident from these figures is the fact that several cycles of seasonal reservoir level fluctuations occurred prior to the bursts of seismic activity. For instance, at Bhatsa reservoir seven cycles occurred before the onset of seismicity and at Lake Oroville eight cycles occurred before the sharp increase in seismic activity began. At Lake Oroville, Rajendran and Gupta (1986) put forth the idea that the large burst of seismic activity in 1975-1976 was related to the, until that time, largest seasonal fluctuation of the reservoir in 1974; however, they could not account for the lack of activity associated with the larger reservoir level variation in 1977. A fatigue/asperity failure model may explain this phenomenon.

The cyclic variation in the reservoir level, in regions prone to RIS, may cause fatigue crack growth in asperities at depth. Fatigue, coupled with stress corrosion, weakens asperities either to the point of failure or to the point at which they are susceptible to large changes in the reservoir level. Once failure occurs, as in the burst of activity in 1976, the stresses at depth redistribute onto new asperity surfaces until a state of dynamic equilibrium is reached. At this point the fatigue process begins again. If a large reservoir level fluctuation occurs early in the fatigue process when the asperities are not sufficiently weakened failure will not result. On the other hand, failure will result from large reservoir level fluctuations later on in the fatigue process when the asperities are weaker and more vulnerable. This would explain why some large changes in reservoir levels are associated with seismicity and others are not. In addition, the three to six year lag time between the filling of a reservoir and the onset of seismicity (see section on RIS) in the majority of RIS cases may be an indication that three to six fatigue cycles are necessary to bring about failure.

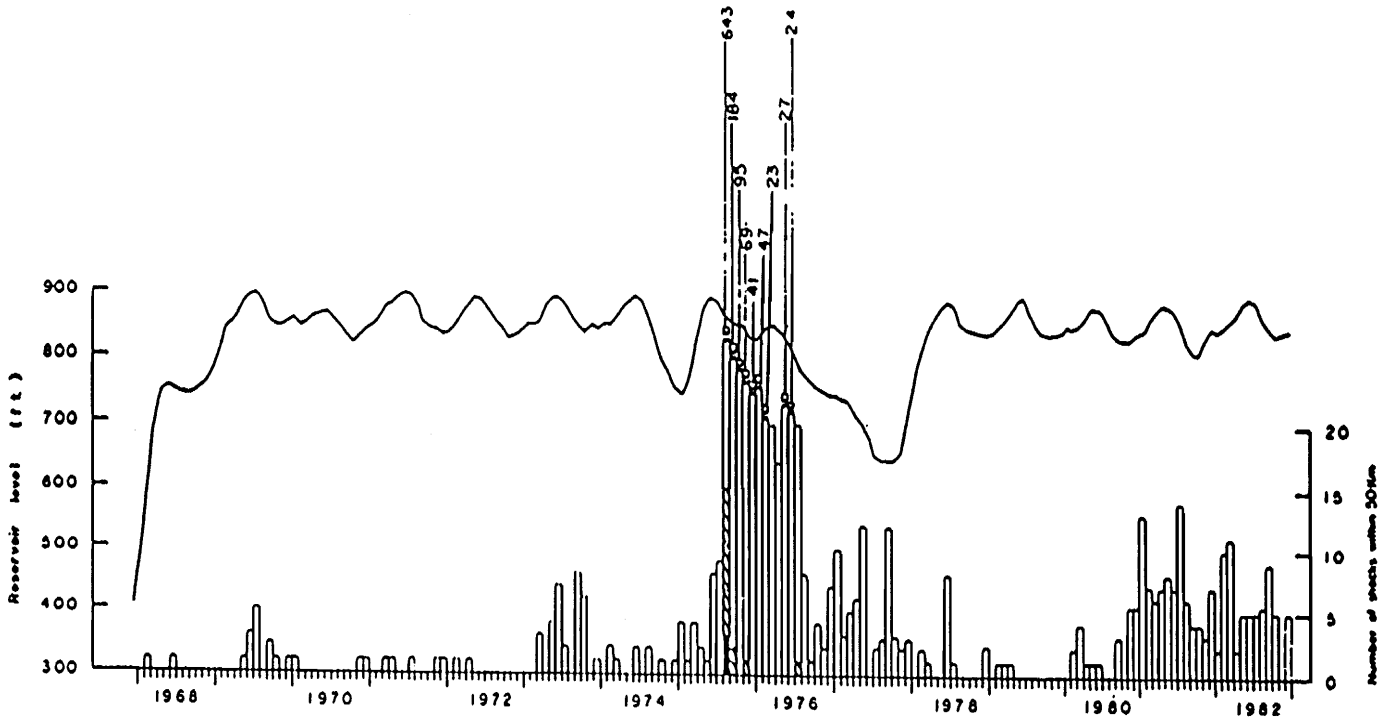

Figure 21. **Seismicity and Reservoir Level–Lake Oroville, California:** Reservoir level (curve, scale on left) and number of earthquakes (columns, scale on right). Note the annual reservoir level periodicity. Eight reservoir level cycles prior to the burst of seismic activity in 1976 may be a rough indication of the number of hydraulically induced fatigue cycles necessary for the generation of seismicity for crustal conditions. From Rajendran and Gupta, 1986.

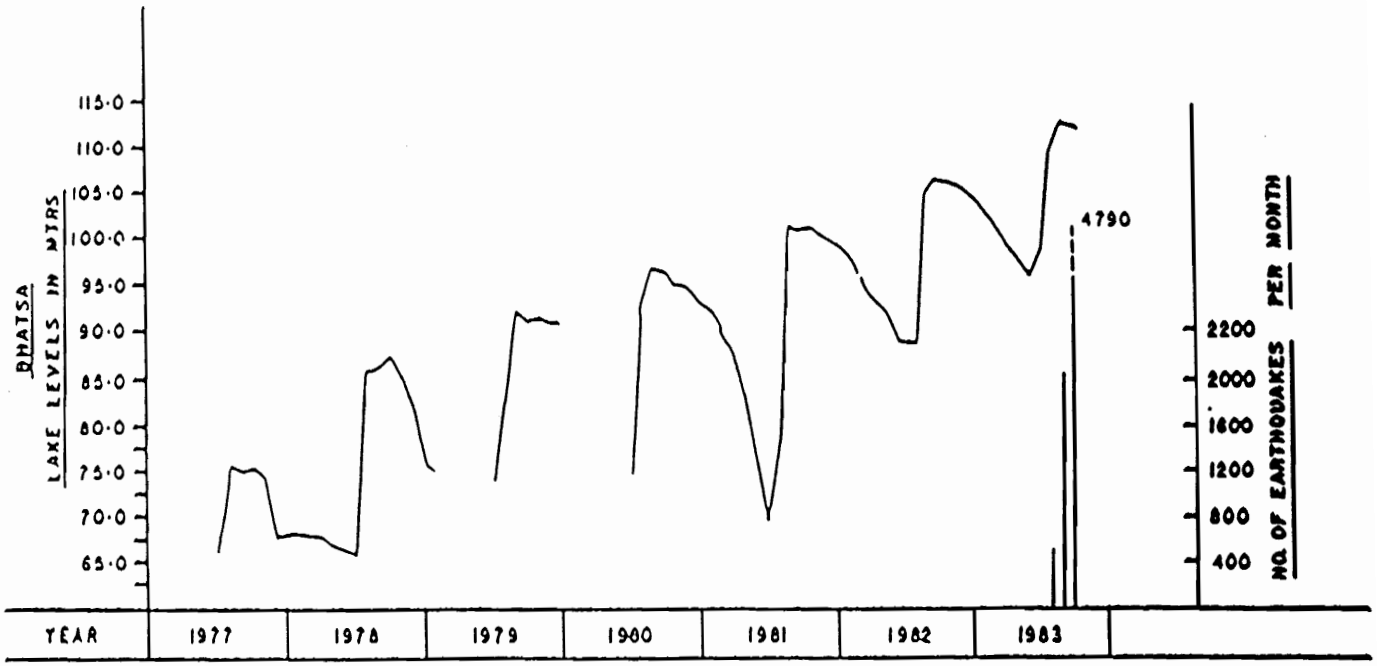

Figure 22. Seismicity and Reservoir Level--Bhatsa reservoir Maharashta, India: Reservoir levels (curve, scale on left) and seismicity (columns, scale on right). Note the annual reservoir level periodicity. Seven reservoir level cycles prior to the burst of seismic activity in 1983 may be a rough indication of the number of hydraulically induced fatigue cycles necessary for the generation of seismicity for crustal conditions. From Rastogi and others, 1986.

No doubt, one may ask are the sizes of the asperities modeled in this analysis reasonable? Certainly, one may never know for sure; however it does seem that there will be different levels of asperity size. For instance, large asperities will contain smaller asperities which will in turn contain even smaller asperities and so on. Therefore, it seems that asperities of the scale used in these analyses will exist in the subsurface. Also, if the asperities bear the entire load across the fracture surface then they must be areas of stress concentration. Consequently, what is the order of magnitude of the stresses acting on the asperity? An attempt has been made in the previous discussion to assess the effect upon the stress within an asperity of different horizontal compressive stresses. Conceptually, it seems that different asperities will be in different states of contact across a fracture. In other words, within a population of asperities some asperities will be in full contact across a fracture while others may only be in partial contact. Accordingly, each asperity may have a different magnitude of horizontal compressive stress depending on the level of contact across the fracture. As a result, it is reasonable to assume that the magnitudes of the horizontal compressive stress used in these analyses could exist in the subsurface. Moreover, it seems that the state of contact across a fracture will be in a process of continual change. For example, as weaker asperities fail or crumble other asperities will take on the load that these weaker asperities had supported. Therefore, the state of stress within an asperity is dynamic, constantly changing as the stresses across a fracture are redistributed.

Conclusions

The frictional properties of a fracture surface are governed by the strength of asperities. Furthermore, although failure across a fault results from shear stresses, it is possible that tensile stresses and subsequent tensile failure within asperities initiates faulting (Byerlee, 1967). These two statements were the motivation behind this investigation. Results from this analysis indicate that tensile stresses do exist within asperities. Moreover, the presence of fluids at pressures at or near hydrostatic significantly increases both the percentage of the asperity in tension and the magnitudes of the tensile stresses. In addition, small transient increases of fluid pressure driven by water table or river level increases can propagate to hypocentral depths and alter the stresses within an asperity. As a result, it does seem reasonable that small transient increases in fluid pressure can trigger asperity failure and lead to earthquake activity as suggested by Costain and others (1987).

In conclusion, a model, consistent with the Hydroseismicity model, is put forth in which hydraulically induced structural weakening and failure of asperities by fatigue is the driving force behind seismicity. Intraplate seismic zones are assumed to be fractured, permeable, saturated volumes hydrologically connected to fluids at the Earth's surface. Accordingly, changes in the elevation of the water table or river levels will result in a change in the pore pressure at depth. This pore pressure change diffuses along a fracture network where it encounters asperities and imparts a pore

pressure change within the asperities. This pore pressure change causes a change in the stresses within the asperity. The elevation of the water table and the river levels exhibits an annual periodicity. Consequently, the pore pressure within an asperity also follows an annual cycle which causes cyclic tensile stresses to develop within the asperity. Accordingly, fatigue, driven by cyclic tensile stresses, causes microcrack growth. Additionally, chemical crack growth mechanisms such as stress corrosion enhance the growth of these microcracks. As the microcracks grow they nucleate until they can just barely support the stresses within the asperity. At this point, the asperity is sufficiently weak so that a small stress change resulting from a small transient pore pressure increase will cause the cracks to grow in an unstable manner and ultimately lead to failure. An earthquake may be initiated when a population of asperities is weakened to the point at which it is vulnerable to small applied stresses, which include transient fluid pressure increases due to extended periods of elevated water table levels.

Bibliography

Atkinson, B. K., Subcritical crack propagation in rocks: Theory, experimental results and applications, J. Struct. Geol., **4**, 41-56,1982.

Atkinson, B. K., Subcritical crack growth in geologic materials, J. Geophys. Res., **89**, 4077-4114, 1984.

Bell, M. L. and A. Nur, Strength changes due to reservoir-induced pore pressure and stresses and application to Lake Oroville, J. Geophys. Res., **83**, 4469-4483, 1978.

Bollinger, G.A., L. Glover, III, J.K. Costain, M.S. Sibol and C. Coruh, The Central Virginia Seismic Zone-Seismicity and Subsurface Geology, Eqke. Notes, **54**, (Abstr.), 83-84, 1983.

Bollinger, G.A., J.A. Snoke, M.S. Sibol and M.C. Chapman, Virginia Regional Seismic Network, **NUREG/CR-4502**, U.S. Nuclear Regulatory Commission, Washington, DC, 57 pp., 1985.

Brace, W. F., Permeability of crystalline rock: New in situ measurements, J. Geophys. Res., **89**, 4327-4330, 1984.

Bradshaw, F. J. and C. Wheeler, Effect of environment and frequency on fatigue cracks in an Al alloy, Int. J. Fract. Mech., **5**, 255-268, 1969.

Broek, D., **Elementary Engineering Fracture Mechanics**, Martinus Nijhoff Publishers, The Haque, 469 pp., 1982.

Byerlee, J. D., Frictional characteristics of granite under high confining pressure, J. Geophys. Res., **72**, 3639-3648, 1967.

Carder, D. S., Seismic investigations in the Boulder Dam area, 1940-1944 and the influence of reservoir loading on earthquake activity, Bull. Seismol. Soc. Am., **35**, 175-192, 1945.

Coruh, C., G. A. Bollinger, and J. K. Costain, Seismogenic structures in the Central Virginia Seismic Zone, in review, 1987.

Costain, J. K., J. A. Speer, L. Glover III, L. Perry, S. Dashevsky, and M. McKinney, Heat flow in the Piedmont and Atlantic Coastal Plain of the Southeastern United States, J. Geophys. Res., **90**, 2123-2135, 1986.

Costain, J. K., G. A. Bollinger, and J. A. Speer, Hydroseismicity: A hypothesis for intraplate seismicity near passive rifted margins, Seismological Research Letters, in press, 1987.

Davison, F. C., Jr., and M. J. Bode, A note on the December 1986 - January 1987 Richmond, Virginia, felt earthquake sequence, Seismological Research Letters, in press, 1987.

Evans, D. M., The Denver area earthquakes and the Rocky Mountain Arsenal disposal well, Mountain Geology, **3**, 23-36, 1966.

Ewalds, H. L., and R. J. H. Wanhill, **Fracture Mechanics**, Edward Arnold Ltd., London, 304 pp., 1984.

Gandhi, C. and M. F. Ashby, Fracture mechanism maps for materials which cleave: F.C.C., B.C.C. and H.C.P. metals and ceramics, Acta Metall., **27**, 1565-1602, 1979.

Glover, L., G.A. Bollinger and J.K. Costain, Geology and Seismicity of the Central Virginia Seismic Zone, GSA Abstr. with Prog., **11**, SE Sec. 28th Ann. Mtg., 180, 1979.

Griffith, A. A., The phenomena of rupture and flow in solids, Phil. Trans. Roy. Soc. of London., **A 221**, 163-197, 1921.

Gupta, H. K., The present status of Reservoir Induced Seismicity investigations with special emphasis on Koyna earthquakes, Tectonophysics, **118**, 257-279, 1985.

Haimson, B. C., Crustal stresses in the Michigan Basin, J. Geophys. Res., **83**, 5857-5863, 1978.

Haar, L., J. S. Gallagher, and G. S. Kell, **NBS/NRC Steam Tables**, Hemisphere Publishing Corporation, Washington D. C., 320 pp., 1984.

Healy, J. H., W. W. Rubey, D. T. Griggs, and C. B. Raleigh, The Denver earthquakes, Science, **161**, 1301-1310, 1968.

Howells, D. A., The time for a significant change of pore pressure, Engineering Geology, **8**, 135-138, 1974.

Hsieh, P. A., and J. D. Bredehoeft, A reservoir analysis of the Denver earthquakes: A case of induced seismicity, J. Geophys. Res., **86**, 903-920, 1981.

Hubbert, M. K., and W. W. Rubey, Role of fluid pressures in mechanics of overthrust faulting: I Mechanics of fluid-filled porous solids and its application to overthrust faulting, Bull. Geol. Soc. Amer., **70**, 115-166, 1959.

Huyakorn, P. S., and B. H. Lester, STAFAN: A two-dimensional code for simulating fluid flow and the interaction of fluid pressure and stress in fractured rock for repository assesment, Battelle Office of Nuclear Waste Isolation, Report No., 427, 1983.

Huyakorn, P. S., and G. F. Pinder, **Computational Methods in Subsurface Flow**, Academic Press, New York, 473 pp., 1983.

Jaeger, J. C. and N. G. W. Cook, **Fundamentals of Rock Mechanics**, 2nd Edition, John Wiley and Sons, New York, 585 pp., 1976.

Kim, K., Deformation and failure of rock under monotonic and cyclic tension, Ph.D. Degree in Mining Engineering, University of Wisconsin-Madison, 105 pp., 1976.

Major, M. W., and R. B. Simon, A seismic study of the Denver (Derby) earthquakes, Q. Colo. Sch. Mines, **63**, 9-55, 1968.

Munsey, J.W. and G.A. Bollinger, Focal Mechanism Analyses for Virginia Earthquakes, Bull. Seism. Soc. Am., **75**, 1613-1637, 1985.

Nava, S. J., The New Madrid Seismic Zone: A test case for naturally induced seismicity, M. S. Degree in Geology, Memphis State University, 128 pp., 1983.

Parker, A. P., **The Mechanics of Fracture and Fatigue: An Introduction**, E. and F. N. Spon, Ltd., London, 167 pp., 1981.

Rajendran, K. and H. K. Gupta, Was the earthquake sequence of August, 1975 in the vicinity of the Lake Oroville, California, reservoir induced?, Phys. Earth and Planet. Interiors, **44**, 179-199, 1986.

Raleigh, C. B., J. H. Healy, and J. D. Bredehoeft, Faulting and crustal stress at Rangely, Colorado, in **Flow and Fracture of Rocks**, Monograph 16, American Geophysical Union, Washington, D. C., 275-284, 1972.

Rastogi, B. K., R. K. Chadha, and I. P. Raju, Seismicity near Bhatsa, reservoir, Maharashtra, India, Phys. Earth Planet. Int., **44**, 179-199, 1986.

Rundle, T. A., M. M. Singh, and C. H. Baker, In-situ measurements in the Earth's crust in the Eastern United States, **NUREG/CR-4623**, U. S. Nuclear Regulatory Commission, Washington D. C., 76 pp., 1987.

Segall, P., Rate dependent extensional deformation resulting from crack growth in rock, J. Geophys. Res., **89**, 4185-4195, 1984.

Simmons, G. and D. Richter, Microcracks in rocks, in **The Physics and Chemistry of Minerals and Rocks**, R. G. J. Sterns, Editor, John Wiley and Sons, Ltd., London, 697 pp., 1976.

Simpson, D. W., Seismicity changes associated with reservoir loading, Engineering Geology, **10**, 123-150, 1976.

Swanson, P. L., Subcritical crack growth and other time- and environment-dependent behavior in crustal rocks, J. Geophys. Res., **89**, 4137-4152, 1984.

Talwani, P. and S. Acree, Pore pressure diffusion and the mechanism of Reservoir Induced Seismicity, Pageoph, **122**, 959-963, 1985.

Uhrhammer, R. A., Observations of the Coyote Lake, California Earthquake Sequence of August 6, 1979, Bull. Seism. Soc. Am., **70**,559-570, 1980.

Zoback, M. D. and S. Hickman, In situ study of the physical mechanisms controlling induced seismicity at Monticello Reservoir, South Carolina, J. Geophys. Res., **87**, 6959-6974, 1982.

Zoback, M. L., and M. D. Zoback, State of stress in the conterminous United States, J. Geophys. Res., **85**, 6113-6156, 1980.

Appendix A. Pressure and Temperature Dependence of Density and Viscosity

The density as a function of temperature and the pressure as a function of density and temperature for pure water were calculated using the computer routines given by Haar and others (1984). Given a geothermal gradient, the density of water is calculated at 20 m intervals over the range of depths of interest. This information is then used as input to calculate the pressure of a column of water over each 20 m interval. The pressure of each 20 m column of water is summed over the range of interest to obtain the hydrostatic fluid pressure at a particular depth. This information is then used as input to calculate the viscosity of pure water (x 10^{-6} kg/s-m) as a function of temperature and pressure using the following equation from Haar and others (1984),

$$\mu(\rho, T) = \mu_o \exp\left[\frac{\rho}{\rho^*} \sum_{i=0}^{5} \sum_{j=0}^{4} b_{ij}\left[\frac{T^*}{T} - 1\right]^j \left[\frac{\rho}{\rho^*} - 1\right]^j\right] \qquad [A1.1]$$

where

$$\mu_o(T) = \left[\frac{T}{T^*}\right]^{\frac{1}{2}} \left[\sum_{k=0}^{3} a_k \left[\frac{T^*}{T}\right]^k\right]^{-1} \times 10^{-6} \text{ kg/s-m} \qquad [A2.1]$$

$$\rho^* = 317.763\ \text{kg/m}^3$$

$$T^* = 647.27\ \text{K}$$

The values of the constants a_k and b_{ij} are given on p. 314 and p. 315, respectively in Haar and others (1984). It is important to note that there is an error in the published value for a_3; it should be -0.0036744 (Lester Haar, personal communication, 1987). This equation has been approved by the International Association for the Properties of Steam (IAPS) and yields reliable results for values of pressure up to 3500 bar for $T \leq 560°$ C.

Appendix B. Derivation of Governing Equations of Deformation and Flow

The soil consolidation equations as given by Biot (1941, p. 160) are of the following form,

$$G\frac{\partial^2 u_i}{\partial x_j \partial x_j} + \frac{G}{1-2\nu}\frac{\partial \varepsilon}{\partial x_i} - \alpha\frac{\partial p}{\partial x_i} = 0 \qquad \text{(B1.1)}$$

These equations give three equations in four unknowns (u_i and p). The complete solution, therefore, requires Darcy's Law in the form,

$$V_i = -k\frac{\partial p}{\partial x_i} \qquad \text{(B1.2)}$$

where G is the shear modulus, ν is Poisson's ratio, ε represents the volume increase of the soil per unit initial volume, α is a measure of the ratio of the water volume squeezed out to the volume change of the soil if the soil is compressed while allowing water to escape ($\alpha = 1$ for saturated media), u_i are the displacements of the solid skeleton in the direction of the i^{th} unit vector, p is pore pressure, V_i are the components of the Darcy velocities and k is the coefficient of permeability. The above equations can be rewritten in a more complete form (Huyakorn and Pinder, 1983), The equation governing consolidation,

$$G\frac{\partial^2 u_i}{\partial x_j \partial x_j} + (\lambda + G)\frac{\partial^2 u_j}{\partial x_i \partial x_j} - \frac{\partial p}{\partial x_i} = - F_i - \frac{\partial \sigma_{ij}^{\circ}}{\partial x_j} \qquad \text{(B1.3)}$$

where λ is Lame's constant, F_i is the body force and σ_{ij}° is the initial effective stress. The governing equation of fluid flow in a compacting porous matrix can be rewritten as,

$$\frac{\partial}{\partial x_i}\left[\frac{k_{ij}}{\mu}\frac{\partial p}{\partial x_j} + \rho_f g_i\right] = \varphi\beta\frac{\partial p}{\partial t} + \frac{\partial}{\partial t}\left[\frac{\partial u_i}{\partial x_i}\right] \qquad \text{(B1.4)}$$

where k_{ij} is the intrinsic permeability of the porous matrix, μ is the dynamic viscosity of water, ρ_f is the fluid density, φ is the effective porosity and β is the compressibility of water. Equations (B3.1) and (B4.1) are the equations used in the computer code STAFAN to solve the problem of fluid-rock interaction.

The following derivations of equations (B3.1) and (B4.1) are based on Huyakorn and Pinder (1983). Assuming the solid to be linear elastic, consider a representative elementary volume of a porous medium filled with a homogeneous fluid. The total stress, τ_{ij} within the volume must satisfy the force equation of equilibrium,

$$\frac{\partial \tau_{ij}}{\partial x_j} + F_i = 0 \qquad \text{(B1.5)}$$

The total stress, τ_{ij} can be written as the sum of the effective stress, σ_{ij} acting on the solid skeleton and a fluid pressure term,

$$\tau_{ij} = \sigma_{ij} - \alpha p \delta_{ij} \qquad \text{(B1.6)}$$

where δ_{ij} is the identity matrix and α is the physical constant previously defined. In this manner, the effective stress can be expressed as,

$$\sigma_{ij} = \sigma_{ij}^{\circ} + \bar{\sigma}_{ij} \qquad \text{(B1.7)}$$

where σ_{ij}^{o} is the initial effective stress and $\tilde{\sigma}_{ij}$ is the incremental effective stress. If the porous medium is assumed to be isotropic then the linear elastic stress-strain relation can be written as,

$$\tilde{\sigma}_{ij} = 2G\tilde{\varepsilon}_{ij} + \lambda\tilde{\varepsilon}_{kk}\delta_{ij} \tag{B1.8}$$

where $\tilde{\varepsilon}_{ij}$ is the incremental strain of the solid skeleton. If we consider an initial strain, ε_{ij}^{o} then the total strain in the solid skeleton is,

$$\varepsilon_{ij} = \tilde{\varepsilon}_{ij} + \varepsilon_{ij}^{o} \tag{B1.9}$$

On the other hand, assuming that there is no initial strain or that it is negligible then,

$$\varepsilon_{ij} = \tilde{\varepsilon}_{ij} \tag{B1.10}$$

Now, substituting (B1.6) into (B1.5) yields,

$$\frac{\partial}{\partial x_j}\sigma_{ij} - \frac{\partial}{\partial x_i}(\alpha p) + F_i = 0 \tag{B1.11}$$

Substituting (B1.10) into (B1.7) yields,

$$\sigma_{ij} = \sigma_{ij}^{o} + 2G\varepsilon_{ij} + \lambda\varepsilon_{kk}\delta_{ij} \tag{B1.12}$$

Next, substituting (B1.12) into (B1.11) and setting $\alpha = 1$ (for saturated medium),

$$\frac{\partial\sigma_{ij}^{o}}{\partial x_j} + F_i + 2G\frac{\partial\varepsilon_{ij}}{\partial x_j} + \lambda\frac{\partial\varepsilon_{kk}}{\partial x_i} - \frac{\partial p}{\partial x_i} = 0 \tag{B1.13}$$

For the case of small deformations, the Eulerian linear strain tensor can be written as,

$$\varepsilon_{ij} = \frac{1}{2}\left[\frac{\partial u_i}{\partial x_j} + \frac{\partial u_j}{\partial x_i}\right] \tag{B1.14}$$

Finally, substituting (B1.14) into (B1.13) yields,

$$G\frac{\partial^2 u_i}{\partial x_j \partial x_j} + (\lambda + G)\frac{\partial^2 u_j}{\partial x_i \partial x_j} - \frac{\partial p}{\partial x_i} = -F_i - \frac{\partial \sigma_{ij}^{o}}{\partial x_j} \tag{B1.15}$$

which is the desired result.

The governing equation of fluid flow in a compacting porous medium can be mathematically expressed by combining Darcy's law with the equations of conservation of mass of the fluid and solid skeleton. First, define the relative bulk velocity of the fluid as,

$$V_i = \varphi\left[\frac{\partial u_{if}}{\partial t} - \frac{\partial u_{is}}{\partial t}\right] \tag{B2.1}$$

or

$$V_i = \varphi(V_{if} - V_{is}) \tag{B2.2}$$

where φ is the effective porosity, u_{if} and $u_{is}(= u_i)$ are displacements of the fluid and solid, respectively and V_{if} and V_{is} are the corresponding velocities. Equation (B2.2) can be rewritten as,

$$\varphi V_{if} = V_i + \varphi V_{is} \tag{B2.3}$$

Now, using Darcy's Law, V_i can be written in terms of the incremental pressure,

$$V_i = -\frac{k_{ij}}{\mu}\left[\frac{\partial p}{\partial x_j} + \rho_f g_i\right] \tag{B2.4}$$

where ρ_f is the fluid density and g_i is gravitational acceleration.

Next, the continuity equation for the solid mass can be written as,

$$-\frac{\partial}{\partial x_i}[(1-\varphi)\rho_s V_{is}] = \frac{\partial}{\partial t}[(1-\varphi)\rho_s] \tag{B2.5}$$

where ρ_s is the solid density and $1-\varphi$ is the fraction of the representative elementary volume that is composed of solid matrix. Equation (B2.5) can be rewritten by expanding the derivatives and collecting terms,

$$\rho_s\left[\frac{\partial\varphi}{\partial t} + V_{is}\frac{\partial\varphi}{\partial x_i}\right] = (1-\varphi)\left[\frac{\partial\rho_s}{\partial t} + V_{is}\frac{\partial\rho_s}{\partial x_i}\right] + (1-\varphi)\rho_s\frac{\partial V_{is}}{\partial x_i} \tag{B2.6}$$

Next, by introducing the comoving derivative operator for the solid,

$$\frac{D}{Dt} = \frac{\partial}{\partial t} + V_{is}\frac{\partial}{\partial x_i} \tag{B2.7}$$

equation (B2.6) can now be reduced to,

$$\frac{D\varphi}{Dt} = \frac{1}{\rho_s}(1-\varphi)\frac{D\rho_s}{Dt} + (1-\varphi)\frac{\partial V_{is}}{\partial x_i} \tag{B2.8}$$

The continuity equation of the fluid mass can be written as,

$$-\frac{\partial}{\partial x_i}[\varphi\rho_f V_{if}] = \frac{\partial}{\partial t}(\varphi\rho_f) \tag{B2.9}$$

Substituting (B2.3) into (B2.9) yields,

$$-\frac{\partial}{\partial x_i}(\rho_f V_i) - \frac{\partial}{\partial x_i}(\varphi\rho_f V_{is}) = \frac{\partial}{\partial t}(\varphi\rho_f) \tag{B2.10}$$

Now, introducing the comoving derivative operator for the fluid,

$$\frac{D}{Dt} = \frac{\partial}{\partial t} + V_{if}\frac{\partial}{\partial x_i} \tag{B2.11}$$

equation (B2.10) reduces to,

$$\frac{D}{Dt}(\varphi\rho_f) = \varphi\frac{D\rho_f}{Dt} + \rho_f\frac{D\varphi}{Dt} \tag{B2.12}$$

Substituting (B2.8) into (B2.12) yields,

$$-\frac{\partial}{\partial x_i}(\rho_f V_i) = \varphi\frac{D\rho_f}{Dt} + \frac{\rho_f}{\rho_s}(1-\varphi)\frac{D\rho_s}{Dt} + \rho_f\frac{\partial V_{is}}{\partial x_i} \tag{B2.13}$$

Next, introduce the following constitutive relations,

$$\frac{1}{\rho_f}\frac{D\rho_f}{Dt} = \beta\frac{Dp}{Dt} \tag{B2.14}$$

$$\frac{1}{\rho_s}\frac{D\rho_s}{Dt} = C_s\frac{Dp}{Dt} \tag{B2.15}$$

where β and C_s are the compressibilities of the fluid and solid grains, respectively and introduce the following assumptions,

$$\frac{Dp}{Dt} = \frac{\partial p}{\partial t}$$

$$C_s \cong 0$$

Note that the second assumption implies that the solid grains are incompressible. Now, making use of these assumptions equation (B2.13) becomes,

$$\frac{1}{\rho_f}\left[\frac{\partial}{\partial x_i}\left[\rho_f\frac{k_{ij}}{\mu}\left[\frac{\partial p}{\partial x_i} + \rho_f g_i\right]\right]\right] = \varphi\beta\frac{\partial p}{\partial t} + \frac{\partial V_{is}}{\partial x_i} \tag{B2.16}$$

Finally, introducing the assumption that the fluid is slightly compressible, which can be mathematically expressed in the following form,

$$\frac{1}{\rho_f}\left[\frac{\partial}{\partial x_i}\left[\rho_f \frac{k_{ij}}{\mu}\left[\frac{\partial p}{\partial x_i} + \rho_f g_i\right]\right]\right] \cong \frac{\partial}{\partial x_i}\left[\frac{k_{ij}}{\mu}\left[\frac{\partial p}{\partial x_i} + \rho_f g_i\right]\right] \tag{B2.17}$$

Now, by utilizing this assumption and using the definition, $V_{is} = \partial u_i/\partial t$ equation (B2.16) reduces to,

$$\frac{\partial}{\partial x_i}\left[\frac{k_{ij}}{\mu}\frac{\partial p}{\partial x_j} + \rho_f g_i\right] = \varphi\beta\frac{\partial p}{\partial t} + \frac{\partial}{\partial t}\left[\frac{\partial u_i}{\partial x_i}\right] \tag{B2.18}$$

which is the desired result.

Appendix C. Additional Numerical Modeling Results of Stresses Within Asperities

It was determined that a change of one order of magnitude in either Young's Modulus, E or the permeability, k of the asperity did not affect the final equilibrium state of stress within the asperity. On the other hand, the value of Poisson's ratio, v, does affect the stress distributions and magnitudes. Figure 23 shows a comparison of the size of the regions of tension when $v = 0.23$ and $v = 0.27$. For the case where $v = 0.23$ the regions of tension are larger than for the case where $v = 0.27$. Similarly, a smaller value of Poisson's ratio results in greater tensile stress magnitudes and decreased compressive stress magnitudes (see Figure 24). These are the expected results. This can be deduced by comparing the following two equations. The horizontal stress σ_h due to the fluid pressure is given by,

$$\sigma_h = \rho_f g h \qquad [C1.1]$$

where ρ_f is the fluid density ($\cong 1.0$ gm/cc), g is the gravitational acceleration and h is depth below the surface. The horizontal stress σ_h due to the mechanical load is

$$\sigma_h = \left[\frac{v}{1 - v}\right]\rho_f g h + T \qquad [C2.1]$$

where ν is Poisson's ratio, ρ_r is the rock density (2.67 gm/cc) and T is the horizontal applied tectonic stress. Therefore, if $\nu = 0.23$ the horizontal tensile stress magnitude due to fluid pressure is greater than the horizontal compressive stress magnitude due to the mechanical load. The opposite is true for $\nu = 0.27$.

To examine the effect of asperity height upon the stresses within an asperity three different heights were modeled. The asperity height is herein defined as the asperity dimension perpendicular to the fracture wall. The modeled heights were 3.0 cm, 1.4 cm and 0.7 cm. The height is meant only to represent the fracture aperture in the immediate vicinity of the asperity. At some distance from the asperity the fracture aperture may be more or less than the asperity height. Stress distributions as represented by contour plots are given in Figure 25, Figure 26 and Figure 27 for asperity heights of 3.0, 1.4 and 0.7 cm, respectively. In general, the taller the asperity the larger the area of the region of the asperity that is in tension. Overall, the stress magnitudes do not vary significantly with height except along the upper and lower edges which are adjacent to the open fracture (see Figure 28).

In a similar fashion, different asperity lengths and their effect upon the stress distributions and magnitudes were examined. Three different asperity lengths were modeled, $l = 8$ cm, $l = 16$ cm and $l = 32$ cm. For the purpose of comparison, asperity height was held constant at the intermediate of the three asperity heights, $h = 1.4$ cm. Contour plots of the stress distributions are given in Figure 29, Figure 30 and Figure 31 corresponding to $l = 8$ cm, $l = 16$ cm and $l = 32$ cm, respectively. In general, the largest tensile zone is associated with the longest asperity. Also, the 32 cm long asperity tends to have higher tensile and lower compressive stresses than either the 8 or 16 cm long asperity (see Figure 32).

Next, the horizontal (tectonic) stresses were varied and their effect on the stresses within an asperity was modeled. For the purpose of comparison, an intermediate size asperity, 1.4 cm by 16 cm, at $z = 2.5$ km was used for the modeling. Contour plots of the stress distributions

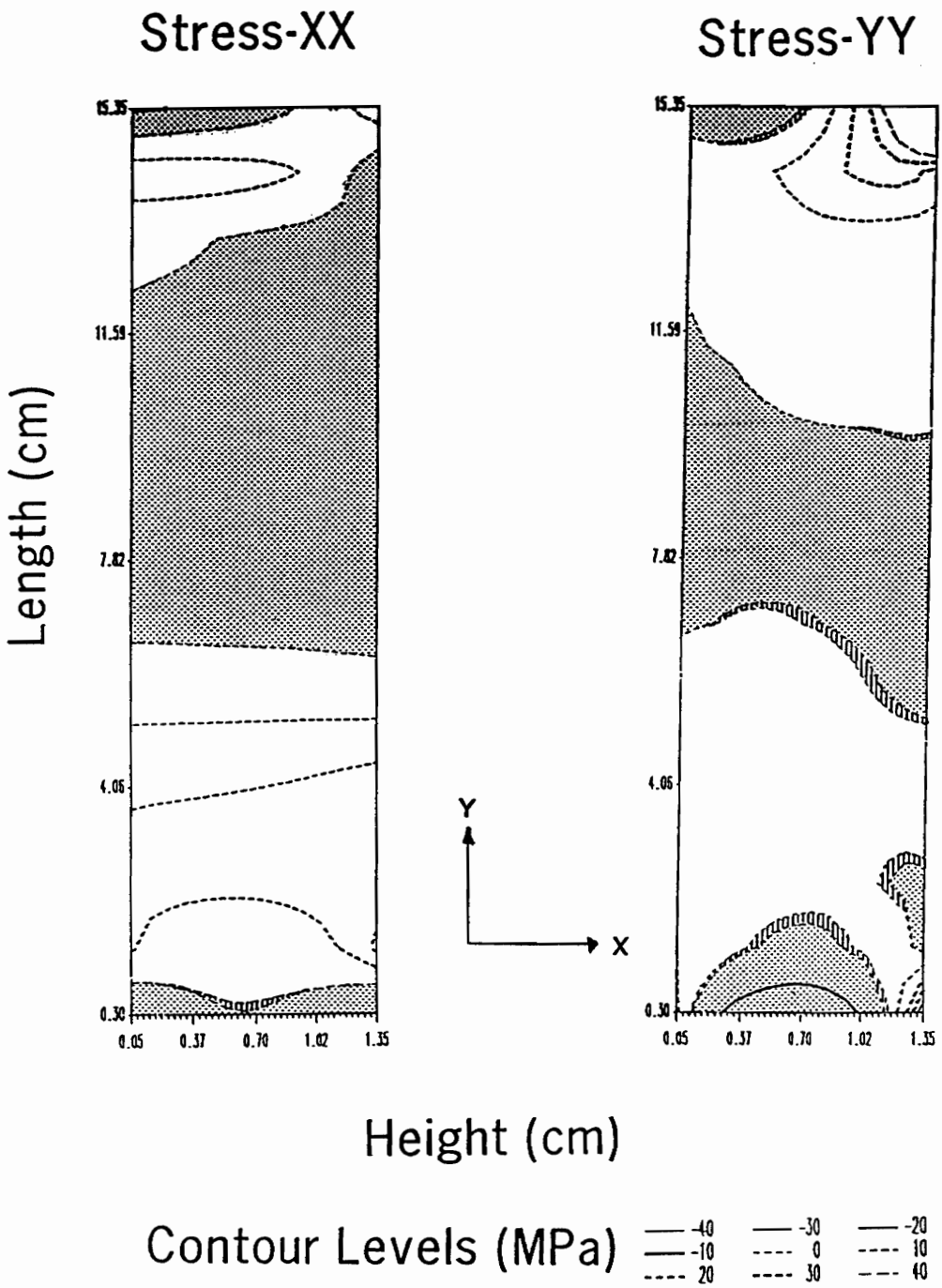

Figure 23. Stress Distribution – Poisson's Ratio Dependence: Stress distribution within a 1.4 cm by 16 cm saturated asperity at a depth of 2.5 km. σ_{xx} is shown on the left and σ_{yy} is shown on the right. Stipples indicate areas of tension for a Poisson's ratio of 0.27. Note the expanded region of tension for Poisson's ratio of 0.23 (indicated by hachures).

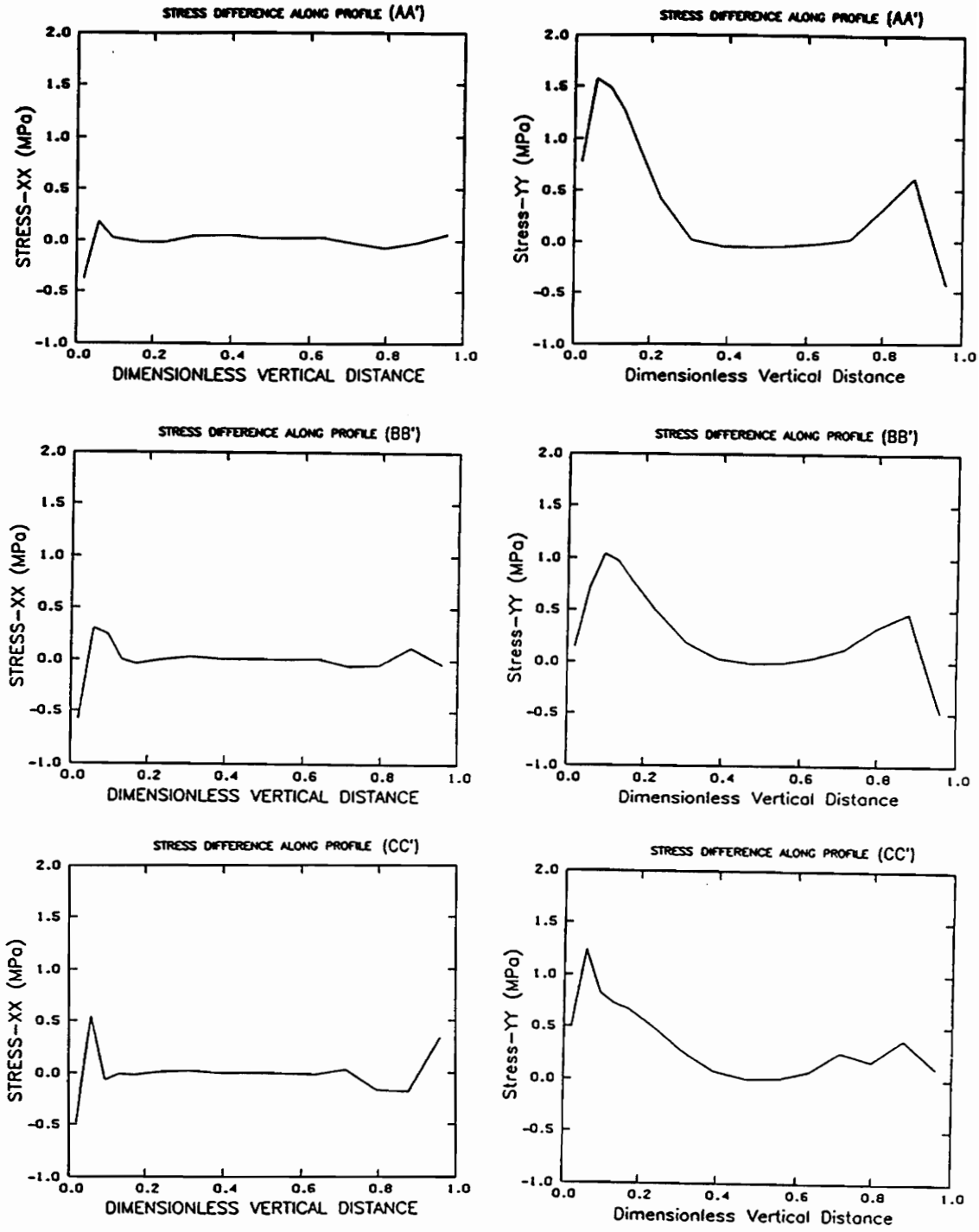

Figure 24. Stress Magnitude Difference for Different Poisson's Ratio: Difference (σ for $\nu = 0.23$ minus σ for $\nu = 0.27$) in stress magnitudes along three vertical profiles through asperity. Negative values indicate regions where the compressive stress magnitude decreased, positive values are indicative of regions where the tensile stress magnitude increased.

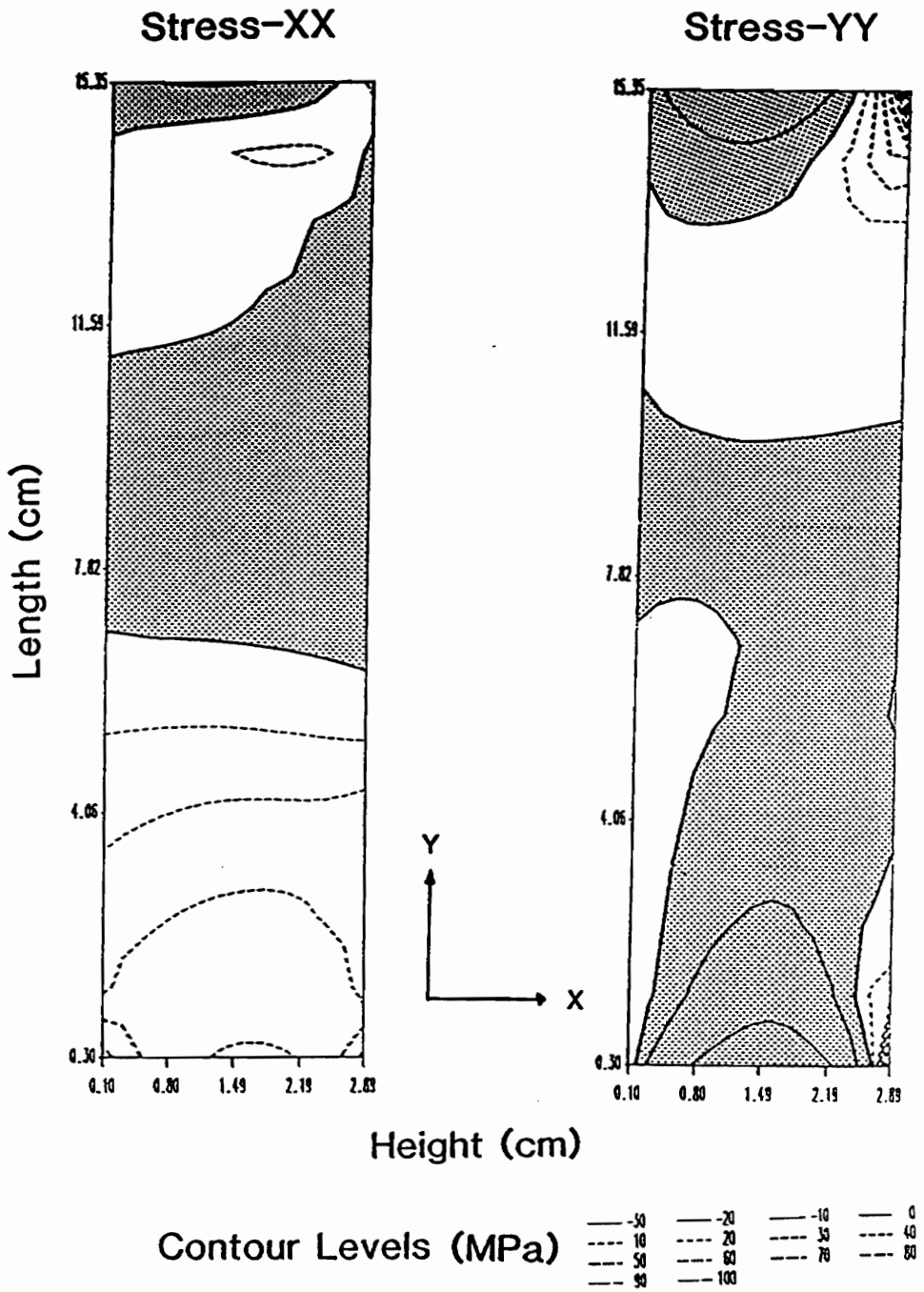

Figure 25. Stress Distribution (h = 3.0 cm): Stress distribution within a 3.0 cm by 16 cm saturated asperity at a depth of 2.5 km. σ_{xx} is shown on the left and σ_{yy} is shown on the right. Stipples indicate areas of tension. Compare to Figure 26 and Figure 27 to see the effect of asperity height on stress distribution.

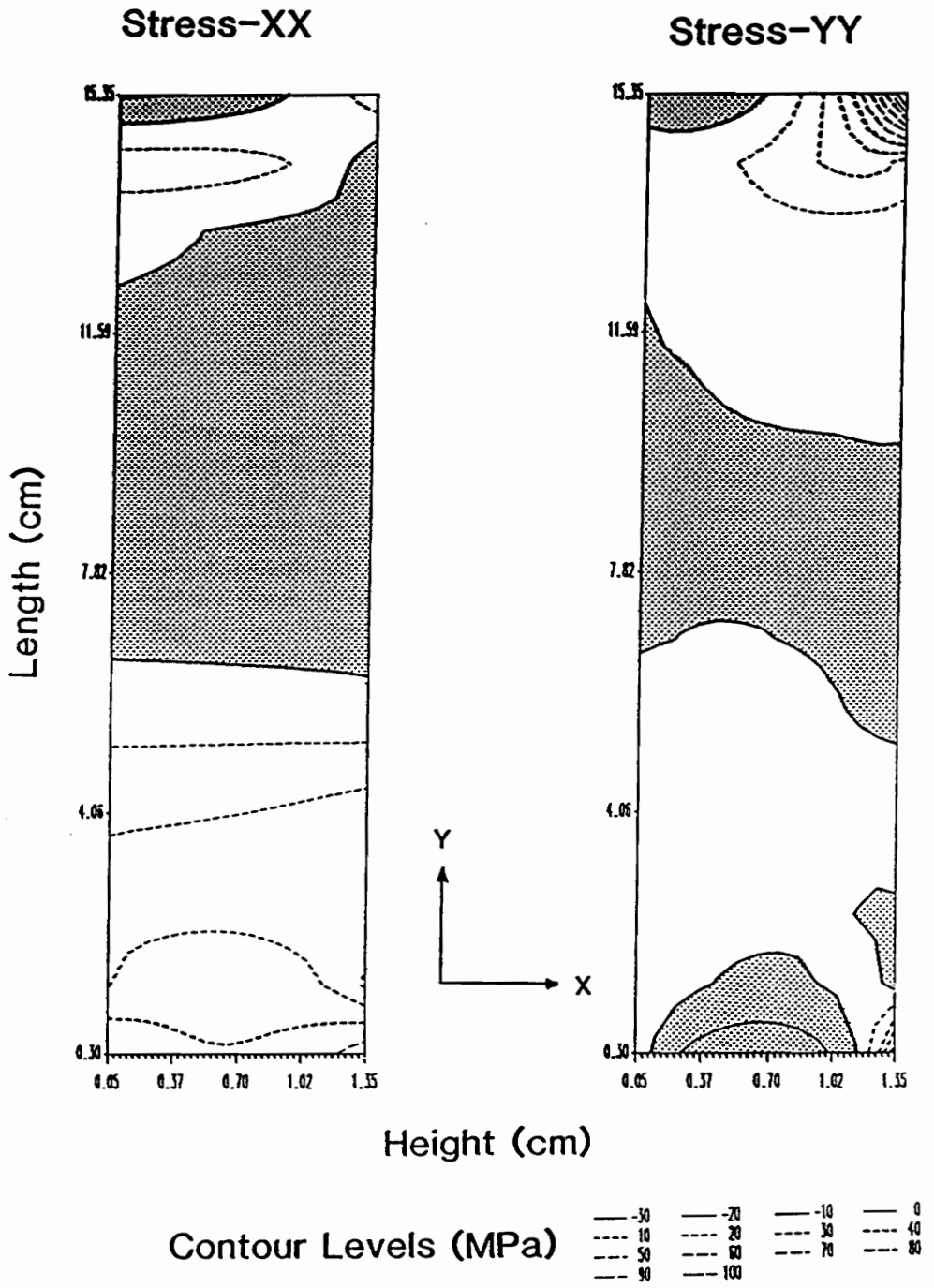

Figure 26. Stress Distribution (h = 1.4 cm): Stress distribution within a 1.4 cm by 16 cm saturated asperity at a depth of 2.5 km. σ_{xx} is shown on the left and σ_{yy} is shown on the right. Stipples indicate areas of tension. Compare to Figure 25 and Figure 27 to see the effect of asperity height on stress distribution.

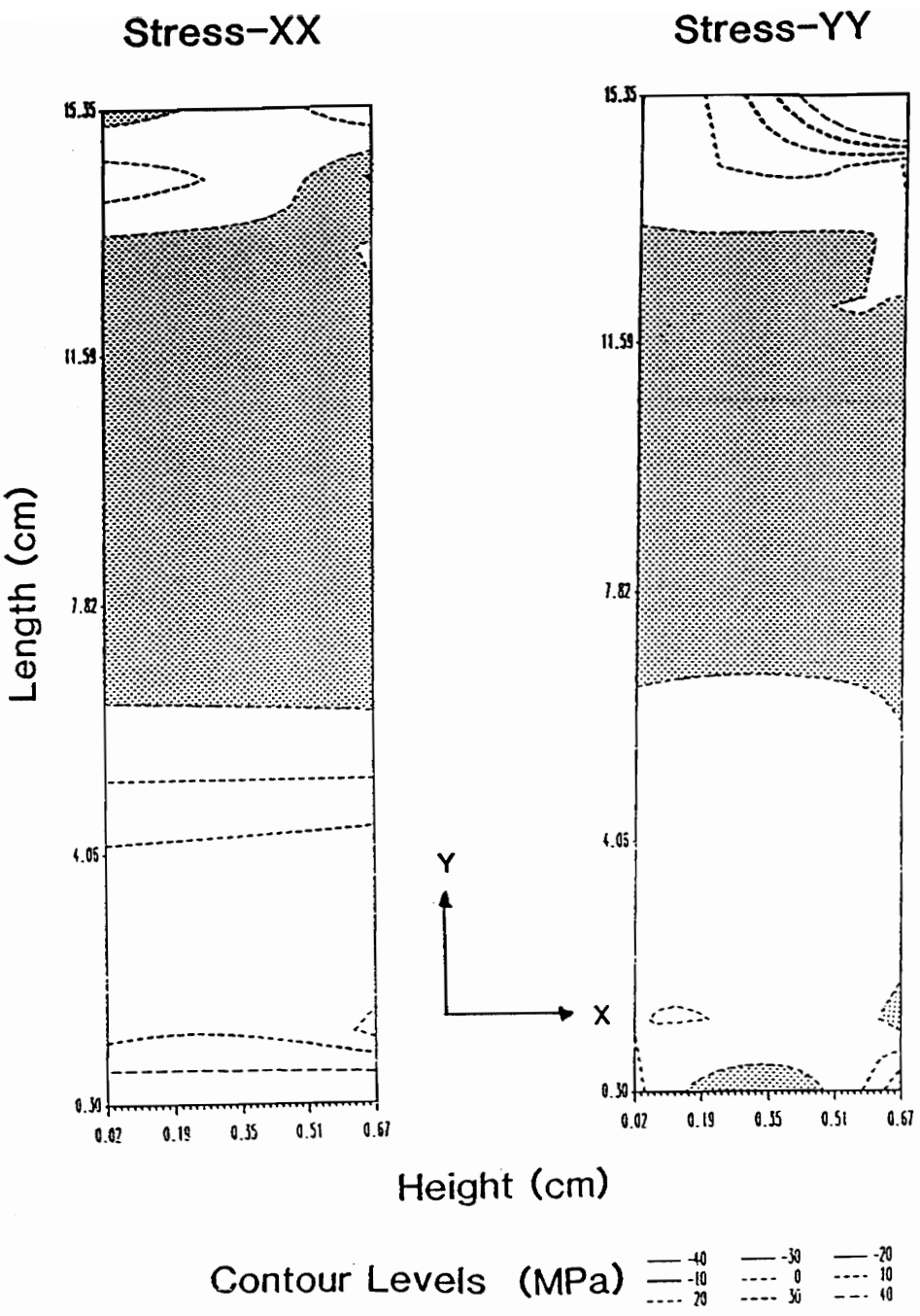

Figure 27. Stress Distribution (h = 0.7 cm): Stress distribution within a 0.7 cm by 16 cm saturated asperity at a depth of 2.5 km. σ_{xx} is shown on the left and σ_{yy} is shown on the right. Stipples indicate areas of tension. Compare to Figure 25 and Figure 26 to see the effect of asperity height on stress distribution.

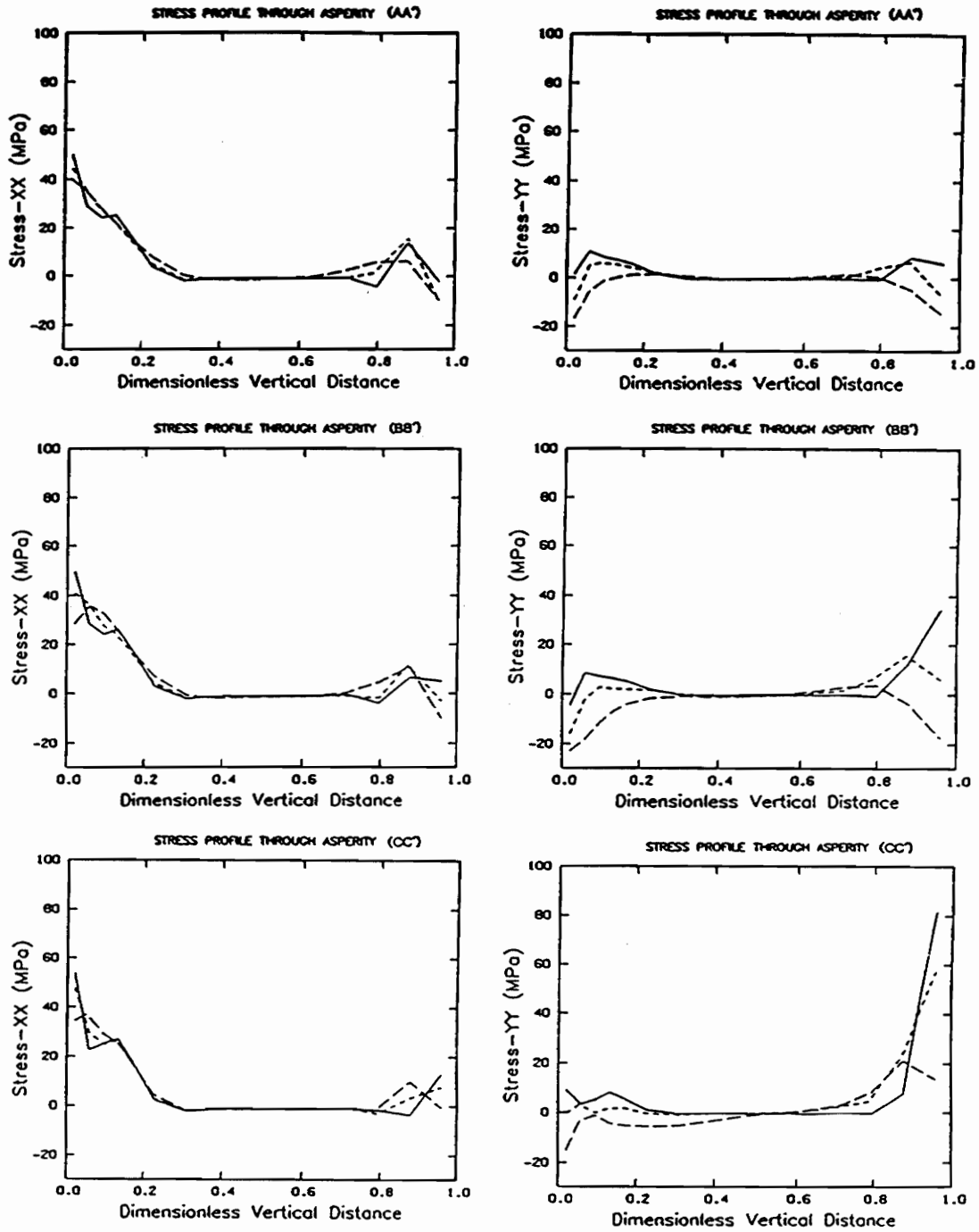

Figure 28. Stress Magnitudes for Different Asperity Heights: Stress magnitudes along three vertical profiles through asperity. Solid line--h = 0.7 cm, short dash--h = 1.4 cm, long dash--h = 3.0 cm.

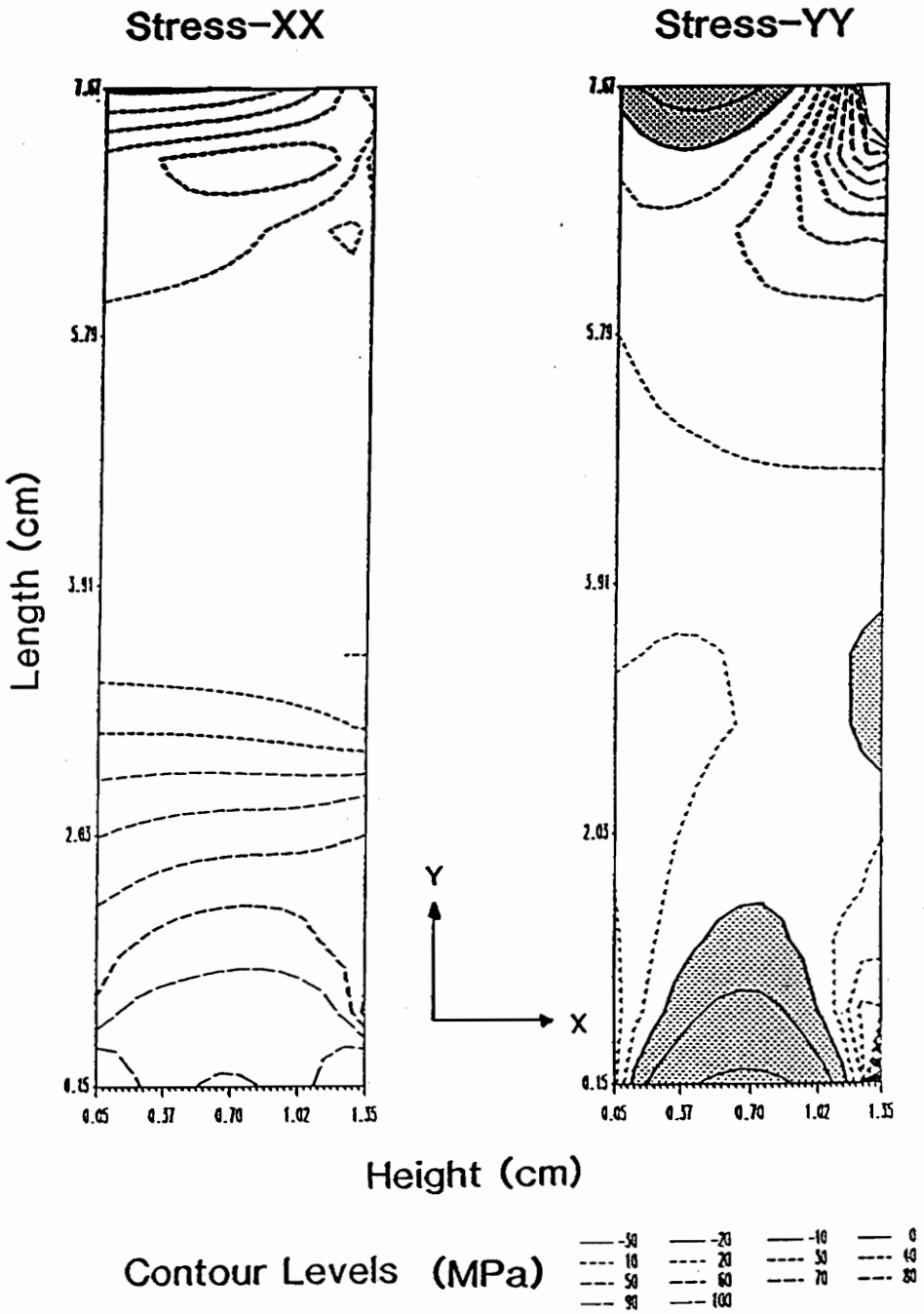

Figure 29. Stress Distribution (l = 8.0 cm): Stress distribution within a 1.4 cm by 8 cm saturated asperity at a depth of 2.5 km. σ_{xx} is shown on the left and σ_{yy} is shown on the right. Stipples indicate areas of tension. Compare to Figure 30 and Figure 31 to see the effect of asperity length on the stress distribution.

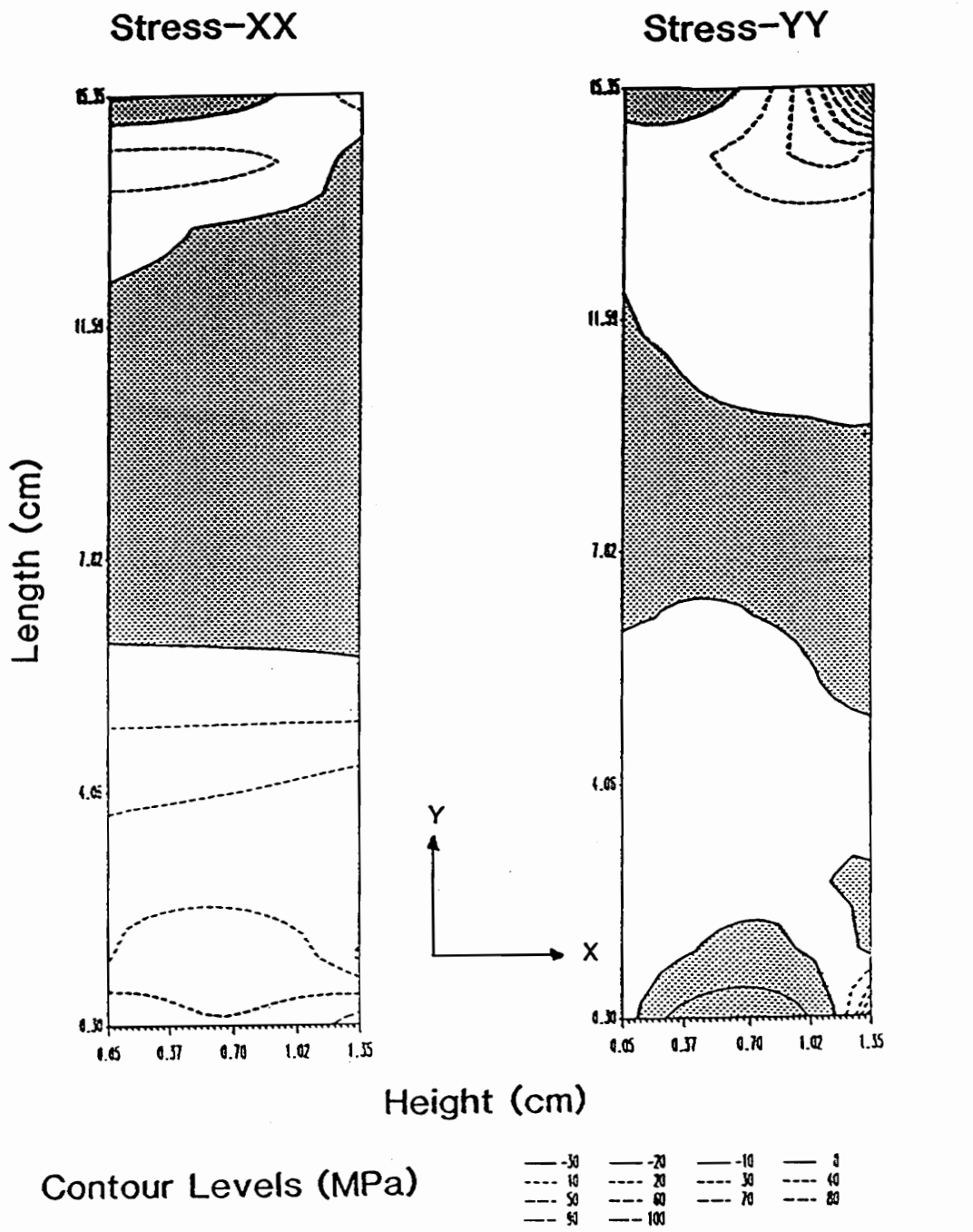

Figure 30. **Stress Distribution (l = 16.0 cm):** Stress distribution within a 1.4 cm by 16 cm saturated asperity at a depth of 2.5 km. σ_{xx} is shown on the left and σ_{yy} is shown on the right. Stipples indicate areas of tension. Compare to Figure 29 and Figure 31 to see the effect of asperity length on stress distribution.

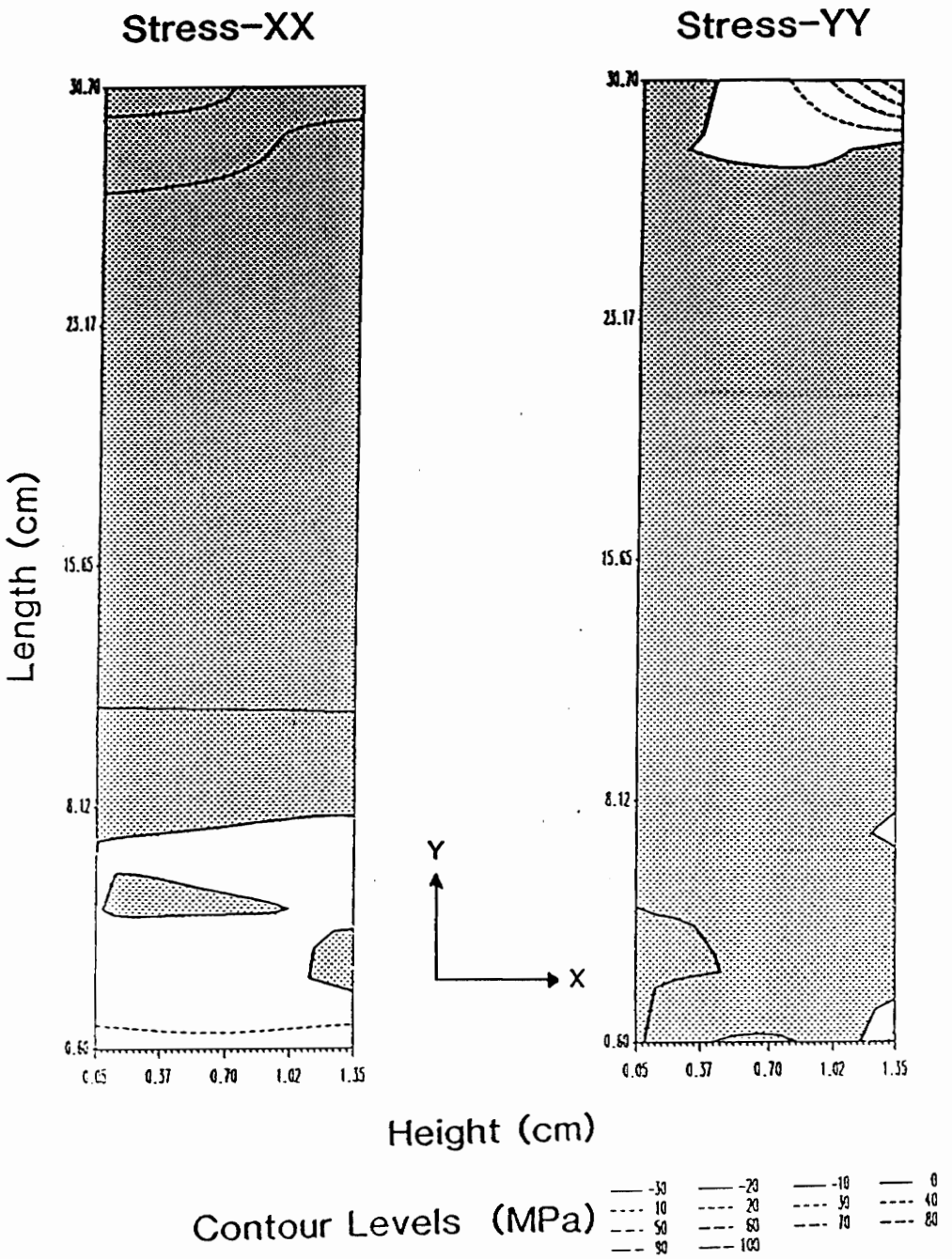

Figure 31. **Stress Distribution (l = 32.0 cm):** Stress distribution within a 1.4 cm by 32 cm saturated asperity at a depth of 2.5 km. σ_{xx} is shown on the left and σ_{yy} is shown on the right. Stipples indicate areas of tension. Compare to Figure 29 and Figure 30 to see the effect of asperity length on stress distribution. Note that the largest area of tension is in the 32 cm long asperity.

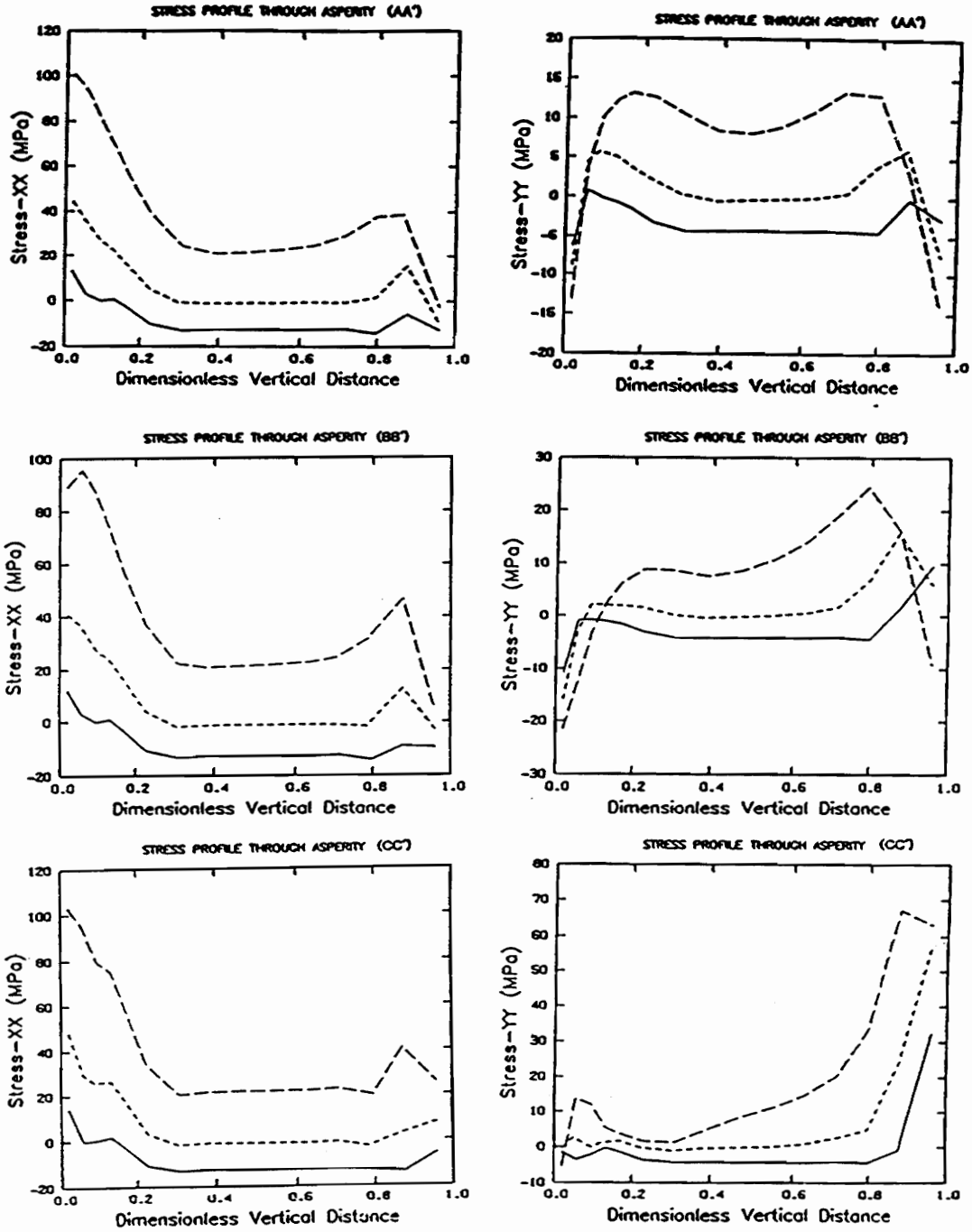

Figure 32. Stress Magnitudes for Different Asperity Lengths: Stress magnitudes along three vertical profiles through asperity. Solid line--l = 32 cm, short dash--l = 16 cm, long dash--l = 8 cm. Note that the 32 cm long asperity has the greatest tensile stress magnitudes.

are given in Figure 33, Figure 34 and Figure 35 for horizontal stresses of 10 Mpa, 50 Mpa and 100 Mpa, respectively. Moreover, stress magnitude curves are given in Figure 36. In general, the higher the applied horizontal stress the smaller the area of tension, the lower the tensile stress and the higher the compressive stress values. These are precisely the results one might expect.

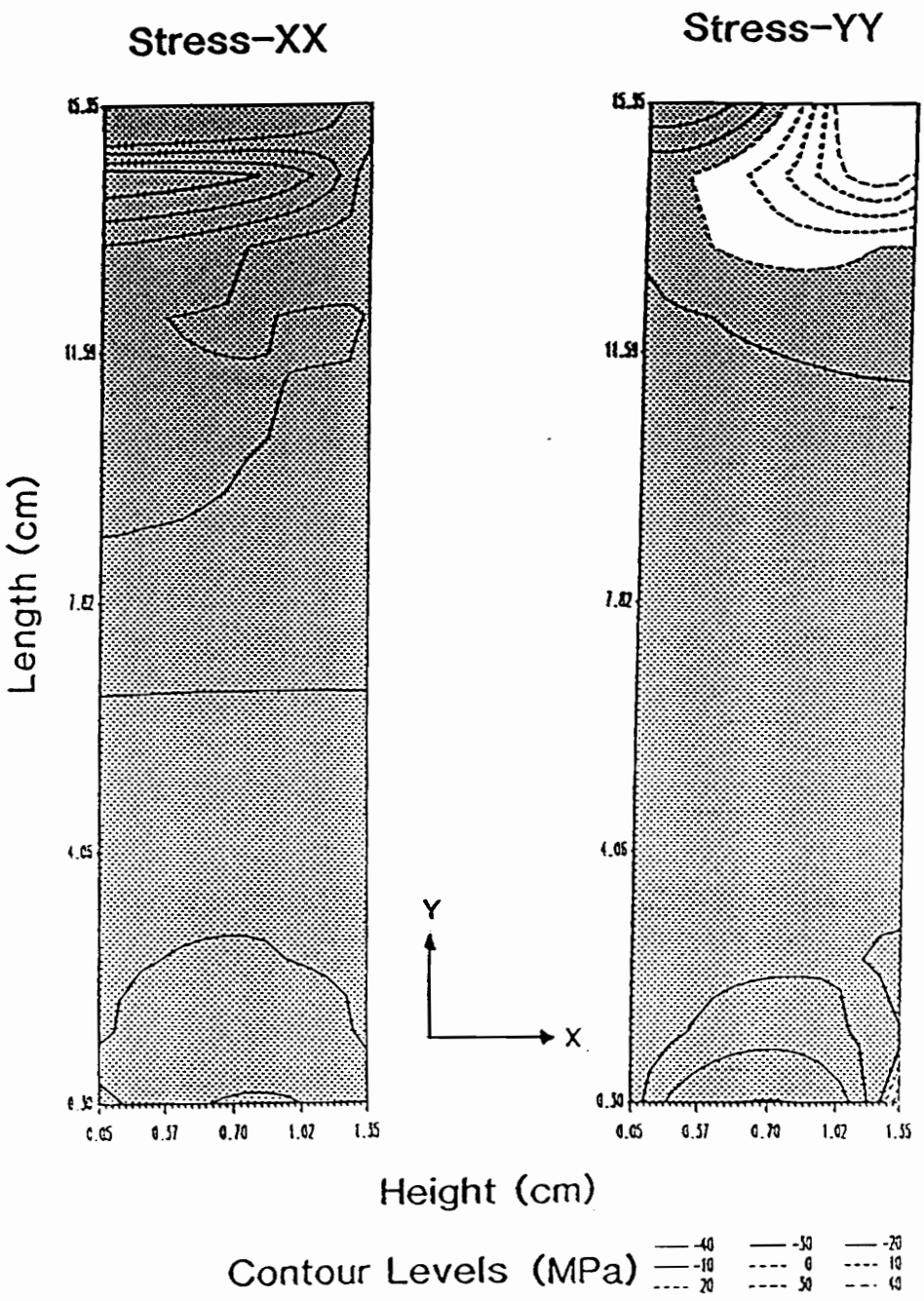

Figure 33. **Stress Distribution–Horizontal Stress = 10 Mpa:** Stress distribution within a 1.4 cm by 16 cm saturated asperity at a depth of 2.5 km. σ_{xx} is shown on the left and σ_{yy} is shown on the right. Stipples indicate areas of tension. Compare to Figure 34 and Figure 35 to see the effect of different horizontal compressive stress magnitudes on the stress distribution within an asperity.

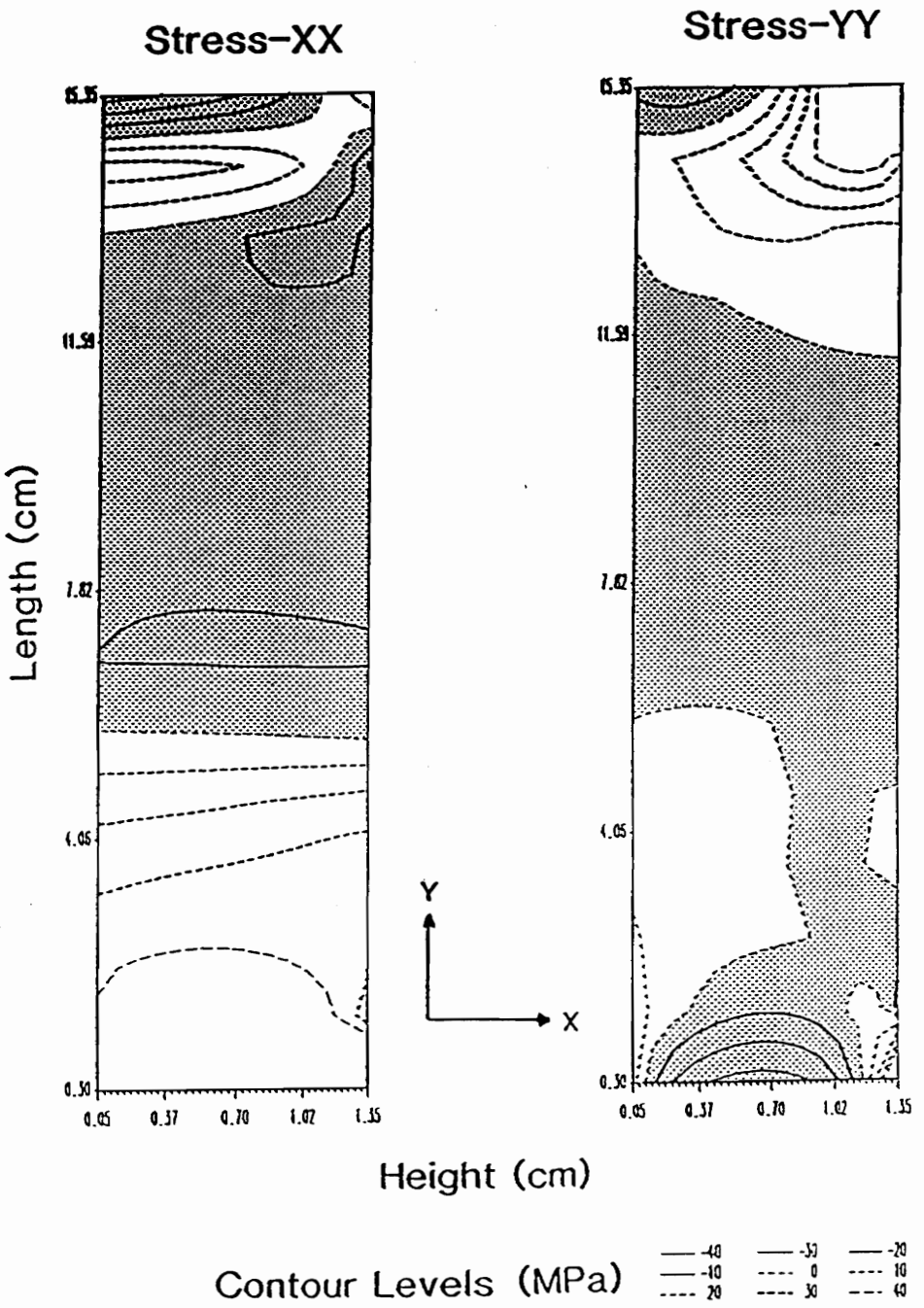

Figure 34. **Stress Distribution–Horizontal Stress = 50 Mpa:** Stress distribution within a 1.4 cm by 16 cm saturated asperity at a depth of 2.5 km. σ_{xx} is shown on the left and σ_{yy} is shown on the right. Stipples indicate areas of tension. Compare to Figure 33 and Figure 35 to see the effect of different horizontal compressive stress magnitudes on the stress distribution within an asperity.

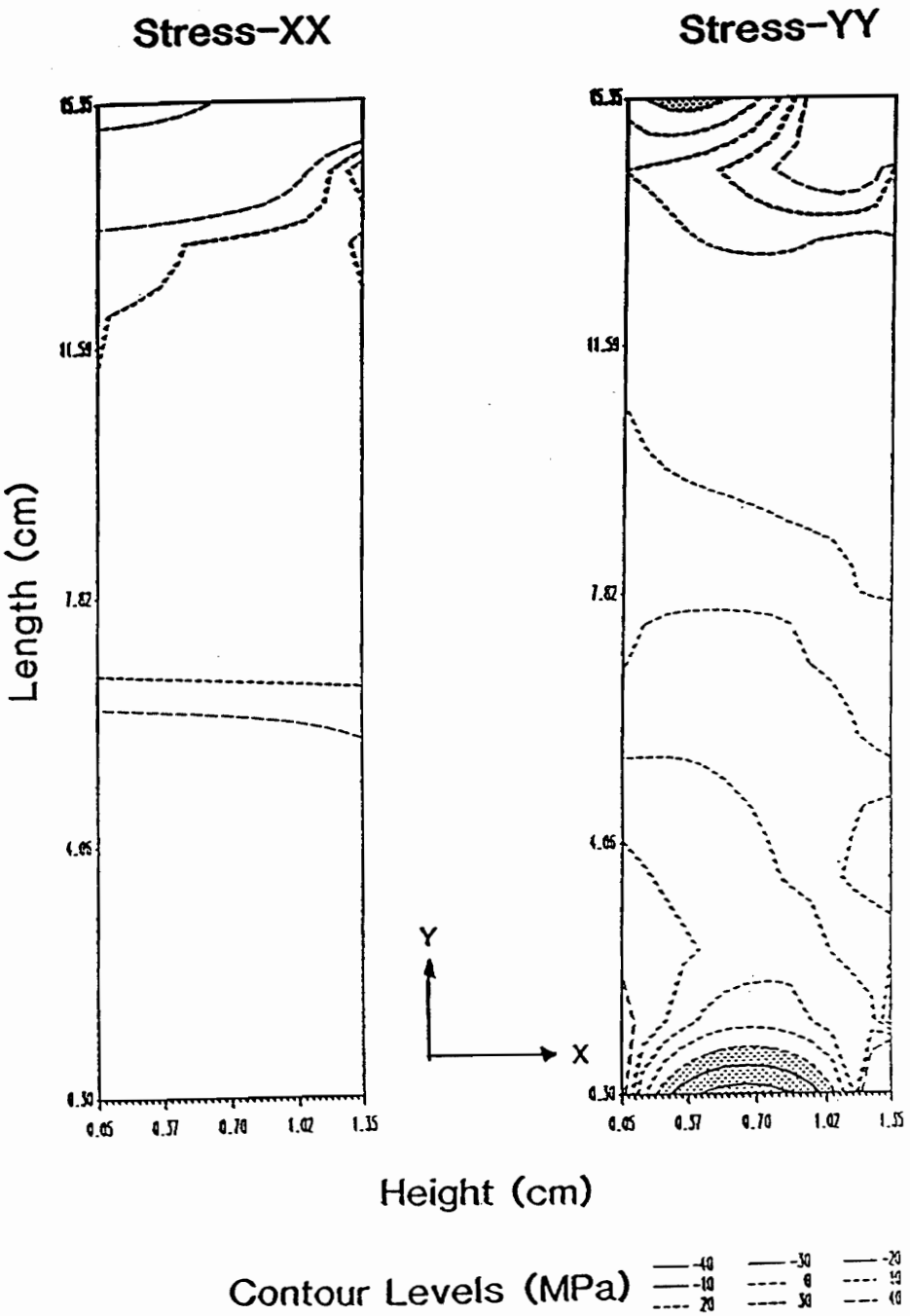

Figure 35. **Stress Distribution–Horizontal Stress = 100 Mpa:** Stress distribution within a 1.4 cm by 16 cm saturated asperity at a depth of 2.5 km. σ_{xx} is shown on the left and σ_{yy} is shown on the right. Stipples indicate areas of tension. Compare to Figure 33 and Figure 34 to see the effect of different horizontal compressive stress magnitudes on the stress distribution within an asperity.

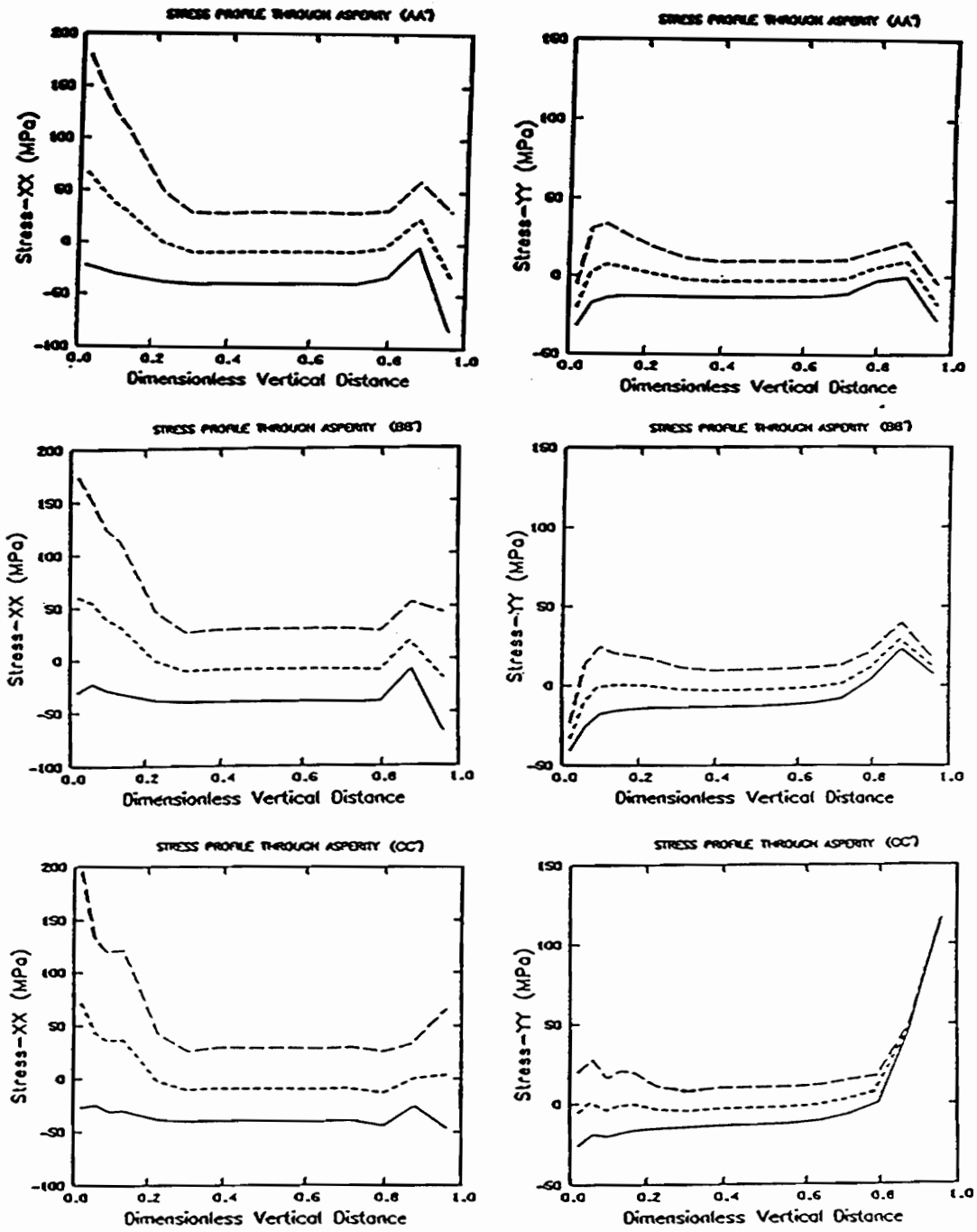

Figure 36. Stress Magnitudes for Different Horizontal Stress: Stress magnitudes along three vertical profiles through asperity. Solid line--10 Mpa, short dash--50 Mpa, long dash--100 Mpa. Note that the higher the applied horizontal compressive stress magnitude the lower the tensile stress magnitude within the asperity.

Appendix D. Asperity Modeling Parameters

The following physical properties used in the numerical modeling of the interaction of pore pressure and stresses are assumed to be temperature and pressure independent. The permeability is taken as the upper end of the range of permeabilities for unfractured crystalline rocks and is

$$k = 1 \times 10^{-12}\,cm^2$$

from Freeze and Cherry (1979). The compressibility of water is also taken from Freeze and Cherry and is

$$\beta = 4.4 \times 10^{-11}\,cm - s^2/gm$$

The porosity, $\varphi = 0.05$ is taken as the upper end of the range for unfractured crystalline rocks (Freeze and Cherry, 1979). Young's modulus,

$$E = 1 \times 10^{12}\,gm / cm - s^2$$

was taken from "Handbook of Physical Constants", 2nd Ed., S. P. Clark, Jr., Ed., **GSA Memoir 97**, New York, 1966, p. 164, and is a representative value for Westerly granite. A value of $v = 0.25$ is used for Poisson's ratio. The remaining parameters were calculated by the author.

The vertical load due to the weight of the rock, F_z was calculated using a rock density of 2.67 gm/cc. The density, pressure and dynamic viscosity of pure water are temperature dependent and were calculated assuming a geothermal gradient of 15° C/km. These values are listed in Table 1.

Table 1. Asperity Modeling Parameters

DEPTH (km)	TEMPERATURE (°C)	DENSITY (gm/cc)	PRESSURE (MPa)	VISCOSITY (gm/cm-s)	F_z (gm/cm-s^2)
2.5	52	0.997	24.3	4.7×10^{-3}	6.5×10^{8}
5.0	90	0.986	47.8	3.0×10^{-3}	1.3×10^{9}
10.0	165	0.949	90.8	1.8×10^{-3}	2.6×10^{9}

Vita

Daniel Lee Needham was born March 3, 1962 in Washington, D. C. He grew up in Vienna, Va. where he graduated from James Madison High School in 1980. Daniel received his B. S. degree in Geophysics with minors in Mathematics and Geology from Virginia Tech in December 1984. In September 1985 he married the former Barbara Ann Swagerty and moved to Blacksburg, Va. to begin work towards the M. S. degree in Geophysics at Virginia Tech. In August 1987 he will complete the requirements for the M. S. in Geophysics and begin work as a Geophysicist/Geologist for Versar, Inc. an environmental engineering consulting firm in Springfield, Va.